Electromigration in solder joints: Towards better understanding using real-time visuals

by

Mostafa Abdelaziz

A thesis
presented to the University of Waterloo
in fulfillment of the
thesis requirement for the degree of
Master of Applied Science
in
Mechanical and Mechatronics Engineering

Waterloo, Ontario, Canada, 2021

© Mostafa Abdelaziz 2021

Author's Declaration

This thesis consists of material all of which I authored or co-authored: see Statement of Contributions included in the thesis. This is a true copy of the thesis, including any required final revisions, as accepted by my examiners.

I understand that my thesis may be made electronically available to the public.

Statement of Contributions

Mostafa AbdelAziz was the sole author of Chapters 3 and 5 which were written under the supervision of Prof. Michael Mayer and were not written for publication.

This thesis consists in part of two manuscripts written for publication. Exceptions to sole authorship of material are as follows:

Research presented in Chapters 1, 2 and 4:

Mostafa AbdelAziz contributed to the literature review, conceptualization, methodology, software, investigation, analysis, and writing of all draft manuscripts.

Dr. Di Xu contributed to providing resources and developing the software.

Dr. Guotao Wang contributed to supervision and project administration.

Mavelyn Breiva and Vivian Mai contributed to the development of the bumping and reflow processes, as shown in Figures 2.8, 2.11, 2.12 and 2.15.

Prof. Michael Mayer contributed to supervision, project administration, funding acquisition, conceptualization, writing, reviewing, and editing of all draft manuscripts.

Permission was granted from Marketplace – Copyright Clearance Center (Order Number: 1109483 obtained on April 5, 2021) to use Figures 1.2 - 1.4.

Citations:

Chapters 1 and 2: Mostafa AbdelAziz, Di Erick Xu, Guotao Wang, Michael Mayer, Electromigration in solder joints: A cross-sectioned model system for real-time observation, Microelectronics Reliability, Volume 119, 2021, 114068, ISSN 0026-2714, https://doi.org/10.1016/j.microrel.2021.114068.

Chapter 4: Mostafa AbdelAziz, Michael Mayer, In-situ Determination of Specimen Temperature during Electromigration Testing of Solder Joint, 2021 IEEE 71st Electronic Components and Technology Conference (ECTC). Manuscript submitted for publication.

Abstract

With the increasing demands and consequent miniaturization of electronic devices, electromigration is posing a challenge to the reliability not only of integrated circuits but also of the electronic packages. A methodology is reported that allows for quasi-continuous in-situ optical microscopic imaging of a cross-sectioned solder joint (sample) during testing for electromigration. This methodology is complemented with another approach that estimates the local temperature increase from Joule heating of the sample which allows for an appropriate temperature selection for the EM test to understand the contribution of failures from Joule heating.

A SAC305 solder joint in a flip configuration was encapsulated in epoxy and cross-sectioned. Current stressing was applied to producing electromigration, with a theoretical current density in the range of $(1.02 - 2.29) \times 10^4\ \mathrm{A/cm^2}$. In-situ optical microscopic imaging and resistance measurements were performed simultaneously until an open circuit was observed. A crack and void started to form in an example experiment, and their evolution was recorded using the real-time imaging. The void and the crack continued growing until the end of current stressing. The void area at the cross-section grew to 1500 μm^2 while the crack grew to a length of 110 μm. After 330 h, the experiment was stopped as an open circuit occurred, which was preceded by a 10% rise of the resistance, indicating failure due to electromigration. During the end of the test, the test vehicle temperature increased by 20 °C as a result of increased Joule heating due to the loss in cross-sectional area of the solder joint. The location of the void did not agree with the expected current crowding location at the solder joint corner. It was inferred that the formation of cracks due to internal stresses prompted the formation of the void at that location that resulted in the open circuit, demonstrating the interconnection between the various failure mechanisms caused by EM. Microstructural changes were also monitored after the open circuit and were possibly due to the thermal stress occurring once the sample cooled down. Hillock formation and additional cracks were observed 30 min after the open circuit.

The results highlight the unique capacity of real-time imaging to support more detailed electromigration research in solder joints by tracing the source of specific failure events. Additionally, cross-sectioning of samples for real-time visuals decreases the cross-sectional area and increases the current density, allowing for accelerated EM testing. Thus, the use of real-time

visuals allows for accelerated tests which is helpful for studying EM under varying test conditions and comparing the reliability of different solder materials through a detailed analysis of the failure times.

Keywords: Electromigration (EM), Current crowding, Solder joint, SAC305, In-situ testing, Reliability

Acknowledgements

First and foremost, all praise to Allah for his blessings and the completion of my thesis. The trials and tribulations throughout my master's degree have only made me a stronger person.

"Allah does not burden a soul beyond that it can bear" (Qur'an, 2:286)

I am deeply indebted to my parents, who have showered me with love and unconditional support – their help cannot be overstated. Their life advice and experiences, which they have bestowed upon me, were key to my personal growth and development; I would not have done it without them. I thank my dad for his integrity, heart-warming empathy, and patience – my mom for her critical thinking, openness, and flexibility – my sister for her support and valuable advice. Although I have yet to catch a cold from going outside with wet hair, or lose an ear to frostbite at -5 °C, their advice has been valuable throughout every stage of my life. I thank my mom for her ability to plan everything a few decades ahead, for she has even planned my kids' future before I was born.

I would like to express my deepest appreciation and gratitude to my academic supervisor, Professor Michael Mayer for giving me the opportunity to do this research and providing invaluable guidance and advice to my research and personal life. His mentorship, patience, professionalism and attention to detail are unparalleled. He has taught me the importance of following a scientific approach and guided me towards that path.

My research would not have been possible without the support of Shehryar Khan, who has acted like a big brother, mentor, and most importantly, a role model. His unwavering guidance and insightful suggestions cannot be overemphasized. Shehryar has helped me through the most difficult challenges. Our disagreements on virtually every topic, from the etiquette of sneezing in public to political ideas, have surprisingly only brought us together.

I would like to thank my thesis committee members, Prof. Elliot Biro and Prof. Jan Kycia, for all their guidance and feedback during this process. Particularly, Professor Elliot has provided valuable advice and insightful suggestions to sample preparation for metallography. His teachings and extensive knowledge in metallography are profound; one would be surprised by his incredible attention to detail and intricacies of his techniques.

I would like to extend my sincere thanks to Dr. Xu Di, Sudharsan Venkatesan, Nick Kam, Mavelyn Breiva, Vivian Mai, Anna Zhang, James Lin, Jane Su, Dr. Pablo Enrique, Cameron Dean, Derek Eppinghoven, Azar Fattahi, Dr. Monica Snowden, Dr. Rob Liang, Alia Rahman, Shasvat Rathod, and all CAMJ members. The support, daily discussions and memories will always be cherished.

Thanks again to Sudharsan, Pablo, Cameron, and Derek whose relentless support has been immense, especially at the end of my journey. Sudharsan, who has taught me more about Mechatronics than I have learned during my undergraduate degree. Pablo, whose bright ideas paved the way for improved methodologies. Cameron, who has offered to help me in *every possible* capacity. Derek, who has taught me more idioms and saying in two months than I have heard in my *entire existence*. His favorite saying is one that mimics his lifestyle: “Life is like a sandwich no matter which way you flip it; the bread always comes first”.

As soon as my thesis gets published, and I cannot make further changes, will I think of the wittiest remarks that I should have included here… For now, I am stuck in quarantine, *dreading* having to format this document. Well, at least you cannot say I was not thinking far ahead… I have got my mom to thank for that!

Table of Contents

Author's Declaration ii

Statement of Contributions iii

Abstract iv

Acknowledgements vi

List of Figures x

List of Tables xvi

Chapter 1. Introduction 1

1.1 Theory of electromigration 5

1.2 Literature review 8

1.3 Scope and objectives 12

Chapter 2. Sample preparation and simulation 14

2.1 PCB design requirements 14

2.2 Test vehicle 1: eight solder joints 16

2.2.1 Solder joint simulation 19

2.2.2 Bumping and reflow processes 24

2.2.3 Details of assembly 30

2.2.4 Resistance characterization 31

2.2.5 Test vehicle preparation for cross-sectional viewing 31

2.3 Test vehicle 2: two solder joints 33

Chapter 3. Equipment used in EM test 35

3.1 List of equipment and specifications 35

3.1.1 Commercial oven 36

3.1.2 Custom-made oven and PID controller 38

Chapter 4. Electromigration test results 41
4.1 Pre-characterization tests 41
4.1.1 Temperature characterization 41
4.1.2 Power characterization 43
4.2 EM test at room temperature 46
4.3 Real-time visuals (RTV) 48
4.3.1 RTV example 1: textbook scenario 48
4.3.2 RTV example 2: current redistribution 53
4.4 Comparison of test vehicles 61
Chapter 5. Conclusions 62
References 64
Appendix A: List of components 69
Appendix B: Custom-made components 70
Appendix C: Setup automation 72

List of Figures

Figure 1.1: (a) Through-hole technology showing leads on bottom side of PCB, (b) surface mount technology showing connection of device directly on PCB, (c) flip chip configuration showing series of solder joints. 1

Figure 1.2: Example of Sn whisker causing a short circuit between two legs (used with permission) [4]. 2

Figure 1.3: Example of thermo-mechanical stresses generated in a flip chip due to CTE mismatch, showing (a) flip chip before solder joining, (b) start of reflow process resulting in misalignment between upper and lower substrates, (c) stress generation causing boards to bend concave downward once assembly is cooled down to room temperature (used with permission) [4]. 3

Figure 1.4: (a) Example of crack propagation in a SAC solder joint, (b) zoomed-in portion of upper interface (used with permission) [4]. 4

Figure 1.5: Forces acting on metal ion during current flow. Electron flow direction shown in green, electric field in red, and current in blue. Electromigration is responsible for electron wind force which displaces metal ion. Current density formula based on JEDEC standard [11]. 6

Figure 1.6: Current crowding in solder joints, showing (a) electron flow direction, (b) void nucleation, (c) void growing along the solder joint-metallization line interface. The final diameter is reduced, increasing the current density. 9

Figure 2.1: Design requirements for selection of solder joint and pad size. Typical geometry of test vehicle for solder joint diameter of 250 μm after reflow. 15

Figure 2.2: (a) Bottom side of motherboard showing voltage probe pads. Flip configuration consists of two daughterboards soldered onto motherboard using SAC305 solder. Figure shows top side of components (b) before and (c) after bumping and reflow processes, and (d) cross-sectional illustration of flip configuration [49]. 17

Figure 2.3: 3D visualization of flip chip channel configuration. Flip configuration consists of 16 channels evenly split between even and odd channels. (a) Channel configurations, showing example of CH 1 (solder) and CH 2 (solder-line) (b) Current flow direction starting from motherboard to daughterboard and back. (c) Even channel configurations measure resistance of copper traces as well as that of solder sample. (d) Odd configurations measure resistance of solder sample alone [49]. 18

Figure 2.4: Simulated dimensions of half solder joint showing the mesh, simulating cross-sectioning. 19

Figure 2.5: Current density simulation. Magnitude of the applied current was 5 A. The maximum solder diameter and height are 275 μm and 200 μm, respectively. Simulation shows (a) reference solder joint with 1 oz Cu and 200 μm wide lines (b) cross-sectioned solder joint (c) thick solder joint with 5 oz copper (d) 400 μm wide solder joint. Location of maximum current density always at interface corner adjacent to current source. Current flows from top-left corner (A) to bottom-right one (B)....21

Figure 2.6: Effect of mesh density on maximum current density, showing an increase in current density with finer mesh densities. 22

Figure 2.7: Current density simulation showing (a) contour plot on middle plane, showing the largest current density in this plane (b) contour plot on top interface (c) simulation of the cross-sectioned plane (d) temperature gradient across different sections of solder joint, revealing high gradients at the current crowding location. Current flows from top-left to bottom-right corner. .23

Figure 2.8: Solder ball bumping process, showing steps (a) to (f). The terminal pitch is 2.54 mm. 25

Figure 2.9: Micrograph of solder pad on daughterboard. The measured diameter of the pad opening is 208 μm. 25

Figure 2.10: Comparison of different flux types, showing (a) RA Rosin Flux Paste – 8342 and (b) MG Chemicals Rosin Flux pen #835-P....26

Figure 2.11: Solder paste process, showing steps (a) to (g). 27

Figure 2.12: Illustration of daughterboard stencil. Stencil was manufactured using stainless steel. Dimensions are 2.162 inches by 1.712 inches, with a thickness of 4 mils. Stencil holes have a diameter of 12 mils. 27

Figure 2.13: Bumping process of solder joints, showing daughterboard (a) before stencil printing (b) after printing and (c) after reflow. 28

Figure 2.14: Tresky T-3000-FC3 die bonder machine, showing (a) machine platform (b) superimposed images of daughter- and mother- boards (c) motherboard placement on heating plate (d) pick and place tool (e) reflow process. 29

Figure 2.15: Cross-sectional morphology of solder joint on test vehicle showing parts of daughterboard, SAC305 solder, and motherboard.....30

Figure 2.16: Sample preparation for cross-sectional viewing procedure. (a) Pads were covered with aluminum foil to prevent epoxy formation on pads (b) epoxy after curing (c) removal of foil, and (d) Pt1000 temperature sensor attached to sample along with voltage and current connections. .32

Figure 2.17: Test vehicle after epoxy curing, showing (a) location of solder joints on left daughterboard and (b) schematic of test vehicle showing location of temperature sensor when current stressing is applied. 32

Figure 2.18: Second variation of test vehicle consisting of motherboard and daughterboard, showing (a) photographs of bonding sides with 42 solder pads each board, (b) assembly with daughterboard flipped onto motherboard and a close-up of an example solder pad, and (c) layout indicating current direction and voltage probe pads. Current direction is shown in red and voltage drop for left and right solder joints is shown in blue and purple, respectively. Location of current-stressed joints (DUTs) is inside orange squares. Only one of the joints DUT was cross-sectioned before EM testing.....33

Figure 2.19: (a) Schematic of motherboard, with dimensions, showing one of current-stressed solder joints inside red rectangle (b) schematic of daughterboard and corresponding solder joint. 34

Figure 3.1: Overview of equipment for the electromigration test showing the main components: oven, mechanical support, multiplexer, voltmeter, power supply and a computer. 35

Figure 3.2: Location of 8 temperature sensors and their respective color-coding shown in Figure 3.3. The graphs on top are shown as solid lines, whereas the ones on bottom are shown as dotted lines with same color corresponding to their top counterpart. 37

Figure 3.3: Temperature distribution curves inside the Binder Oven at 100 °C measured by eight sensors placed as indicated in Figure 3.2. The temperature range is approximately 2 °C at 100 °C, once the temperature stabilizes. Note: Accuracy of Pt1000: ± (0.15+0.002∗T) 37

Figure 3.4: Schematic of experimental setup used in characterization and current stressing tests, showing (a) main method, and (b) alternative method using inverted microscope that allows for automated temperature control. 39

Figure 3.5: Physical experimental setup, showing (a) main method, (b) alternative method, (c) enclosure used for alternative method, and (d) heating method and temperature sensor used for alternative method. 40

Figure 4.1: Temperature characterization test (a) heating curve of test. Three heating stages were utilized at three temperatures: 50, 100 and 140 °C. Sufficient time was elapsed between heating stages to ensure temperature stabilization of oven and ensure sample and temperature sensor reach same temperature. 42

Figure 4.2: Results of temperature characterization test. Line of best fit is drawn to obtain TCR value and error estimate. 43

Figure 4.3: Power characterization test. Red part of curve shows when resistance measurements are recorded, and blue part shows portion when current is switched on and off. Figure shows, (a) entire test starting at 0.5 A until 5 A, with 0.5 A intervals (b) zoom in on the portion at which current was switched on. The resistance increased with higher current as a result of Joule heating. 44

Figure 4.4: Results of power characterization test. Line of best fit is drawn for solder joint. 45

Figure 4.5: (a) Resistance of solder joints during room temperature current stressing test (b) temperature of individual solder joints calculated using thermal resistance (c) test vehicle temperature measured by Pt1000 temperature sensor.....46

Figure 4.6: Thermal resistance values are shown on left in blue and final resistance increase at end of test is shown on right in yellow. 47

Figure 4.7: Evolution of electromigration failure in a single solder joint under I = 10 A and $T_{ambient} \approx 60$ °C, showing void nucleation at cathode and nucleation of smaller voids on anode. Current direction was from top metallization line (anode) to bottom (cathode). The current was switched off in (g) and the temperature was back at room temperature, down from a peak temperature of 107 °C, resulting in a complete separation crack along the anode interface. 50

Figure 4.8: Results from electromigration test with stressing current I = 10 A and nominal ambient temperature $T_{ambient}$ = 60 °C up to 40 % resistance increase. Variations are due to room temperature variations. $R = V/I$ and $P = V \cdot I$, where V is voltage evolution measured across solder joint. 51

Figure 4.9: (a) Resistance measurements showing resistance changes during test. Micrographs are shown in Figure 4.10 at the times indicated by dashed lines. (b) Growth of cracks & voids (c) Resistance measurements at the end of test immediately prior to failure. (d) Temperature fluctuations during test. 54

Figure 4.10: Screenshots of real-time video at (a) 0 h, (b) 102 h, (c) 139 h, (d) 171 h and (e) 276 h, respectively. Images were taken every hour. The electrons flowed from bottom-left to top-right corner.....58

Figure 4.11: Microstructural changes after the test was stopped. (a) Image taken prior to test stoppage. (b) Image after 30 min of switching off power supply and hot plate, showing formation of two cracks. (c) Image after a few hours of test stoppage. The location of void formation was covered by a hillock. (d) Close-up image of hillock formation. 59

Figure 4.12: Another example of a current stressing test showing void and crack formation in two separate solder joints. 60

Figure 4.13: Control setup of solder joint under 80°C and no current stressing. Figure shows test vehicle (a) before test start and (b) after test stoppage. No visible change was observed. 60

List of Tables

Table 1.1: Examples of EM testing conditions seen in literature. 11

Table 2.1: Material parameters used for simulation using built-in material library in Comsol 20

Table 2.2: Results of simulation for different geometries. Applied current was 5 A, corresponding to a nominal current density of 1.59 x 10^4 A/cm^2 according to the JEP154 standard [11]. 21

Table 2.3: Surface Finish Parameters.....30

Table 2.4: Different measurements of the 6 samples. The room temperature was 22 °C. The level of the probing current was 100 mA. Thermoelectric electromotive force (EMF) characterization measurements were not performed which could impact the resistance data. 31

Table 4.1: Real-time viewing test factors and responses (RT=Room Temperature).....49

Chapter 1. Introduction

Soldering is an important process in electronics which is used to form electrical and mechanical connections between electronic devices. Through-hole technology (THT), surface mount technology (SMT), and area array packages are three common methods used to assemble electronic devices onto a substrate, such as a printed circuit board (PCB). THT is the process in which component leads are inserted into drilled holes on a PCB and then the leads are soldered onto the bottom side of the PCB. Alternatively, surface mount technology (SMT) is a method in which electronic devices, termed surface mount devices (SMD), are mounted directly on the printed circuit board (PCB) using solder. Flip chip technology, a sub-component of area array packages, is similar to SMT, but the method is used to mount a semiconductor device, such as an integrated circuit (IC) which consists of an assembly of electrical components, onto a substrate using a series of spherical solder bumps. Due to the layout of the flip chip configuration, flip chip allows for smaller spacing between conductors which produces overall smaller packages. Additionally, flip chip allows for higher speeds and better performance than both THT and SMD [1]. A schematic of the three methods is shown in Figure 1.1. However, due to the small size of the solder joints in flip chip configurations, many reliability concerns have been observed.

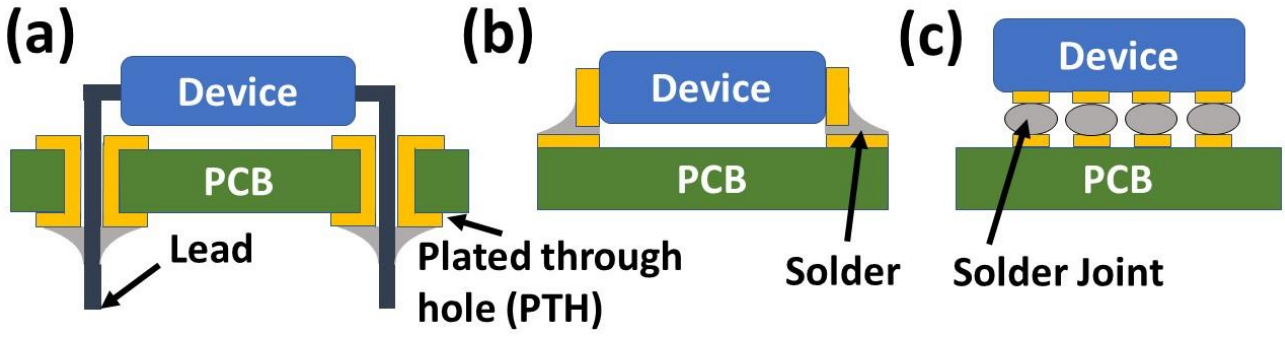

Figure 1.1: (a) Through-hole technology showing leads on bottom side of PCB, (b) surface mount technology showing connection of device directly on PCB, (c) flip chip configuration showing series of solder joints.

Solder joints used in flip chip technology were primarily made of tin (Sn) and lead (Pb) alloys due to their excellent electrical and mechanical properties. However, due to environmental concerns, the electronic packaging industry shifted to Pb-free solder joints [2]. SnPb solder joints possessed some reliability concerns, such as low cycle fatigue due to the thermal stress and coefficient of thermal expansion (CTE) mismatch between the chip and substrate. However, these issues have been exacerbated with Pb-free solder joints since they possess a higher concentration of Sn, which is the primarily material responsible for the reliability concerns [2]. For instance, SAC305 is one of the most common lead-free alloys which is composed of 96.5% tin, 3% silver, and 0.5% copper, compared to Sn63Pb37, composed of only 63% tin.

Reliability concerns are common in Sn-rich alloys since the formation of Sn whiskers can cause short circuits in electronic devices, as shown in Figure 1.2. Copper, which is commonly used as an alternative to Pb in Pb-free joints, reacts with the tin to form Cu_6Sn_5 compound, which is responsible for the whisker growth [3]. However, in flip chip technology, whisker growth is less of a concern since 1) the compressive stress on the solder joints from the metallization lines opposes whisker growth, and 2) the solder joints are further apart, so it is unlikely for a short circuit to occur [2].

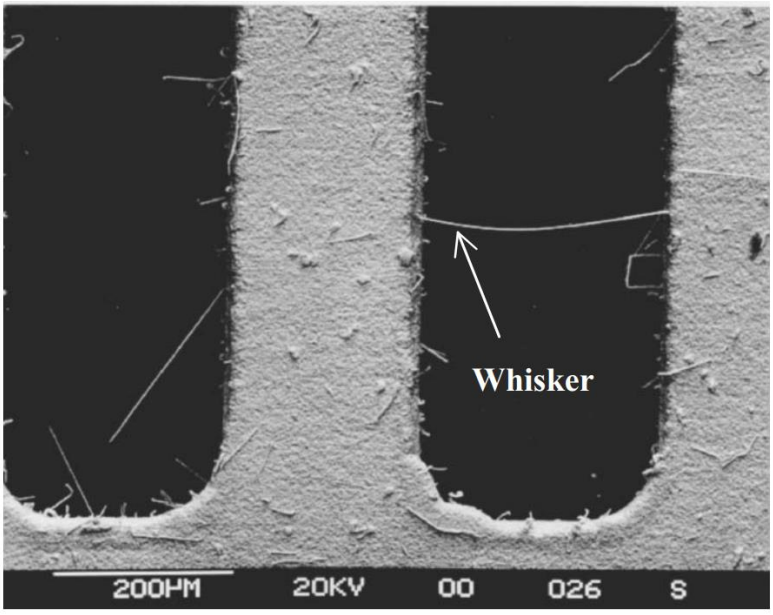

Figure 1.2: Example of Sn whisker causing a short circuit between two legs (used with permission) [4].

On the other hand, thermal-mechanical stresses are a more common reliability concern in flip chip configuration. Thermal-mechanical stress are caused by the CTE mismatch between the Si chip (α = 2.6 ppm/ °C) and PCB, which is made of flame retardant 4 (FR4), a glass-reinforced epoxy resin laminate (α = 18 ppm/ °C) [3]. During the reflow of solder joints at high temperatures, slight misalignment occurs between the solder joints and the pad on the PCB, but it does not cause failure. However, upon cooldown to room temperature, the PCB bends concave downwards, introducing large amounts of shear strain in the solder joints, which might lead to a complete fracture at the interface. The entire process is shown in Figures 1.3 (a) – (c). Epoxy underfill is used to significantly reduce this reliability concern. However, even with the underfill, fractures tend to happen with repeated temperature fluctuations. Temperature cycling and fatigue testing is performed to further study these effects, as established in JEDEC standard JESD22-A104D [2].

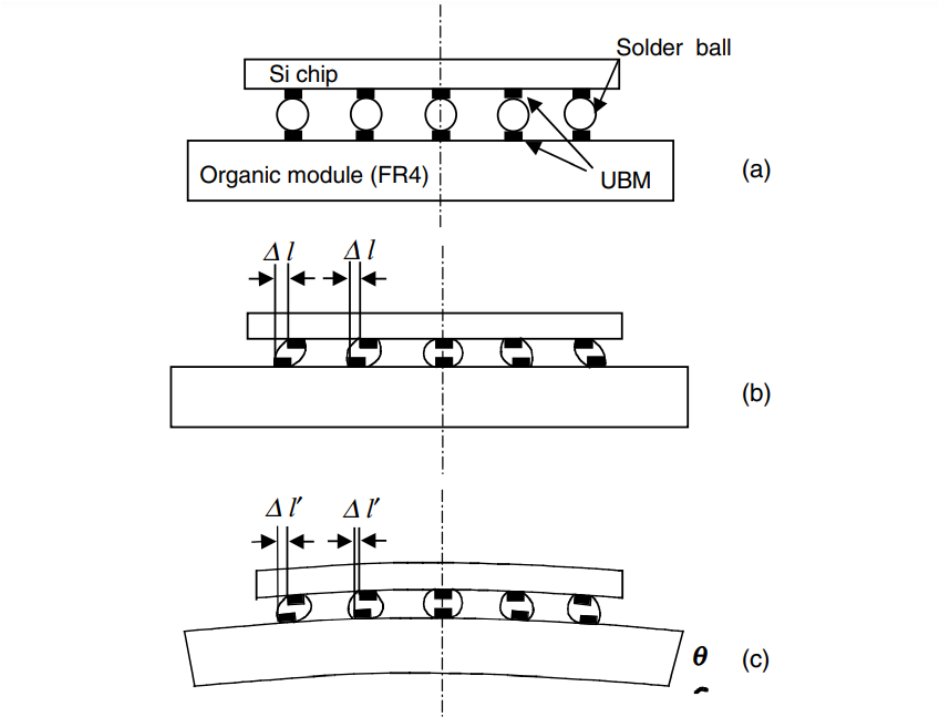

Figure 1.3: Example of thermo-mechanical stresses generated in a flip chip due to CTE mismatch, showing (a) flip chip before solder joining, (b) start of reflow process resulting in misalignment between upper and lower substrates, (c) stress generation causing boards to bend concave downward once assembly is cooled down to room temperature (used with permission) [4].

Impact fracture is another reliability concern in which fracture of the solder joints occurs during shock or impact, such as when dropping an electronic device. This reliability concern becomes more severe when a solder joint ages. Kirkendall voids form at the interface between the solder joint and metallization line, due to the difference in diffusion rates of the metal atoms. The voids make the solder joint more brittle and ultimately more susceptible to fracture. Mini Charpy impact test machines can be used to measure the impact toughness of the studied solder joints [5]. Drop tests can also be used to capture dynamic responses causing solder joint failure while capturing all phases including the crack initiation, propagation and opening [6]. An example of crack formation is shown in Figures 1.4 (a) and (b). Similar to impact fracture testing, fatigue failure can also be studied using vibration loading to obtain cyclic stress versus number-of-cycles-to failure (or S-N) curves [7,8]. Reference [9] has demonstrated a relationship between thermal cycling and drop testing, showing a transition of failure modes when combining both factors.

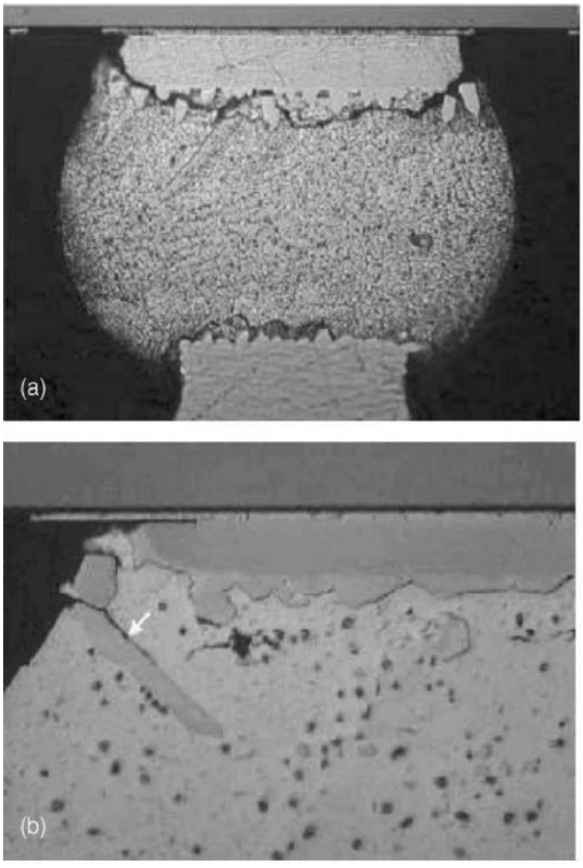

Figure 1.4: (a) Example of crack propagation in a SAC solder joint, (b) zoomed-in portion of upper interface (used with permission) [4].

In addition to the previous concerns, one of the most serious reliability issues in flip chip configuration is electromigration (EM) which occurs under large current densities. Due to the low melting point of solder joints and their geometry, a phenomenon known as current crowding occurs in which non-uniform current density and temperature gradients are generated across the solder joints. These gradients cause intermetallic compound (IMC) growth and void nucleation, decreasing the mechanical strength and electrical properties of the solder joints. Unlike the previously mentioned reliability concerns, EM is not well-understood since it is linked to various factors and other migration phenomena which accelerate failure and make isolating the effects of EM challenging.

1.1 Theory of electromigration

Electromigration is the material transport of metal ions caused by the momentum transfer of moving electrons. When an electric current passes through a conductor, two main forces act on the metal ions of the conductor, namely the "electron wind" force (F_{wind}) and the electrostatic force (F_{field}), as shown in Figure 1.5. F_{field} is the force generated by the interaction of the electric field with the metal ions. This force is miniscule as the metal ions are shielded by the surrounding electrons and therefore can be ignored. On the other hand, F_{wind} is generated by the momentum transfer of the electrons to the metal ions and is responsible for the electromigration phenomenon. For a conductor with small current density, typically smaller than 10^4 A/cm^2 for solder and 10^6 A/cm^2 for either aluminum or copper, the electron wind force is negligible; therefore, electromigration does not occur [10].

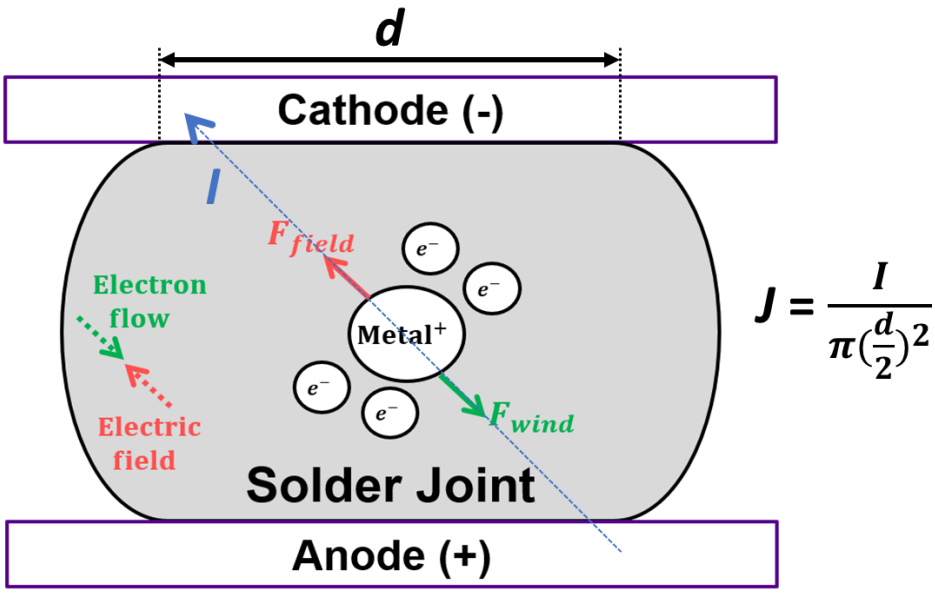

Figure 1.5: Forces acting on metal ion during current flow. Electron flow direction shown in green, electric field in red, and current in blue. Electromigration is responsible for electron wind force which displaces metal ion. Current density formula based on JEDEC standard [11].

However, when a threshold current density is reached, greater than 10^4 A/cm^2 for solder and 10^6 A/cm^2 for aluminum and copper, known as the activation energy, the electron wind force exceeds the electrostatic force and induces a momentum exchange that is transferred to the nearby metal ions. This momentum transfer causes the metal ions to displace from their original position, away from the cathode. This results in loss of metal ions, and consequently material, at the cathode end. Alternatively, metal ions are deposited at the anode. Over time, this results in the formation of voids at the cathode and hillocks at the anode, which translates to an open and short circuit, respectively [12].

J.R. Black developed the first equation, called the Black's equation, to quantify electromigration in a metal film conductor [12]:

$$\frac{1}{MTF} = A\,J^2 e^{\frac{\varphi}{kT}} \tag{1}$$

where:

MTF = median time to failure [h]

A = a constant which contains a factor involving the cross-sectional area of the film

J = current density [$\frac{\mathrm{A}}{\mathrm{cm}^2}$]

Φ = activation energy [eV]

k = Boltzmann's constant

T = absolute temperature [K]

Black's equation is used to obtain the median time to failure (MTF) of a metal conductor which can be used to predict failure times depending on various parameters and experimental conditions. For example, reference [13] performed testing on a SnPb solder joint and reported Φ = 0.8 eV/atom, J = 2.75 x 10^4 A/cm^2, T = 413.15 K, giving a MTF of 1 h. The failure criterion of electromigration is a permanent resistance increase in a conductor. This increase is a result of void nucleation which decreases the effective cross-sectional area that electrons can pass through [10]. A decrease in cross-sectional area, for the same applied current, increases the current density, which decreases the MTF. Current density is a major factor in the determination of MTF, since the relationship between the variables is quadratic.

Electromigration is influenced by many factors as highlighted in Black's equation: current density, activation energy, Boltzmann's constant and temperature. The activation energy is a material constant which entails the type of crystal structure, grain size, type of transport mechanism (grain boundary, bulk and surface diffusion) as well as other factors [12,14]. These factors make studying EM failure challenging; however, the activation energy factor is considered to have the largest potential for slowing down electromigration failure, as evidenced by the amount of research being done in that field [15–18].

Gradients, whether it be temperature, current or ion diffusion coefficient also affect electromigration as the diffusion of atoms is a direct result of the potential gradient across a conductor. Similarly, other migration mechanisms are also closely related and greatly impact electromigration. Electromigration (EM), thermomigration (TM), stress migration (SM) as well as chemical diffusion have all been shown to affect the reliability of electrical circuits [10].

References [2] and [19] have demonstrated that failures due to EM are closely intertwined with TM, particularly in flip chip technology. Similarly, I. A. Blech was one of the first researchers to suggest a relationship between SM and EM [14]. Thus, as previously noted, many factors play a role on EM, and studying the contribution of each migration phenomenon on the failure mechanism is challenging.

Thermomigration is the migration phenomena that is most closely linked to EM [20]. TM occurs when a large temperature gradient occurs in a conductor. In flip chip technology, non-uniform current densities are observed in the solder joints which consequently result in non-uniform temperature distributions. TM has an adverse effect on the reliability of solder joints, further accelerating damage from EM [19,21].

1.2 Literature review

Solder joints in the microelectronic industry serve to increase packing density and reduce space, ultimately leading to faster electronic devices. The gradual decrease in solder joint sizes has led to increased current densities, giving rise to electromigration concerns, risking the electrical and mechanical properties of solder joints [13,22–24]. The initial direction of research was aimed at IC interconnects (very large-scale integration metallization lines). Research included the relationship between current density and the median time to failure (MTF) for IC interconnects, with Black's equation being widely used to predict the MTF for various electronic devices [3,16,25,26]. However, studying electromigration in solder joints has become more popular, in part due to the lower activation energy, around 0.8 eV for solder joints, for electromigration failure and thus requiring smaller current densities to reach failure [13,27]. A summary of the current densities typically observed in solder joints is shown in Table 1.1.

Compared to IC interconnects, solder joints have unique features that influence their electromigration behavior including lower melting point, current crowding, and atomic flux divergence [28,29]. Current crowding is the non-uniform distribution of current density which is predominant in solder joints due to their geometry, wherein the current flow crowds at the corner of the solder joint to produce hot spots with increased current densities. Atomic flux divergence refers to a region of mass accumulation at the interface between the solder joint and metallization

line (usually Cu or Al), which occurs due to the difference in diffusion rates between the two materials, which increases the likelihood of electromigration induced failure mechanisms at the shared interface [30–32]. Furthermore, solder joints are more prone to electromigration failure due to their lower melting points corresponding to higher diffusivity, requiring lower current densities (by an order of 100) to achieve similar failure times [33].

Due to the differences in cross-sectional areas between the solder bump and the interconnect wire, current crowding can occur at the location of electron flow entrance in the solder bump. In solder joints, void propagation is observed in the cathode to follow a "pancake shape", starting from the location of the highest current density and propagating horizontally in the under bump metallization (UBM) [31], as shown in Figure 1.6. This uneven current distribution across the solder joint has given rise to another driving factor, thermomigration [33]. EM also influences the formation of intermetallic compounds (IMCs); the formation of IMCs has been shown to accelerate failures in solder joints [34].

Thus, the unique features in solder joints such as the interface geometry between the metallization lines and solder joint, solder composition as well as the anisotropic material properties of Sn have made solder joints a weak link in electronic packages. Mass flux divergence occurs at interfaces between dissimilar metals. In solder joints, this corresponds to the interface between the solder joint and metallization line, in which atomic flux divergence occurs. Additionally, due to the geometry of the solder joint, the conducting line is not straight but rather turns at the corner, creating non-uniform current distribution. Ultimately, these factors have also made the study of EM failure mechanisms challenging [24,35].

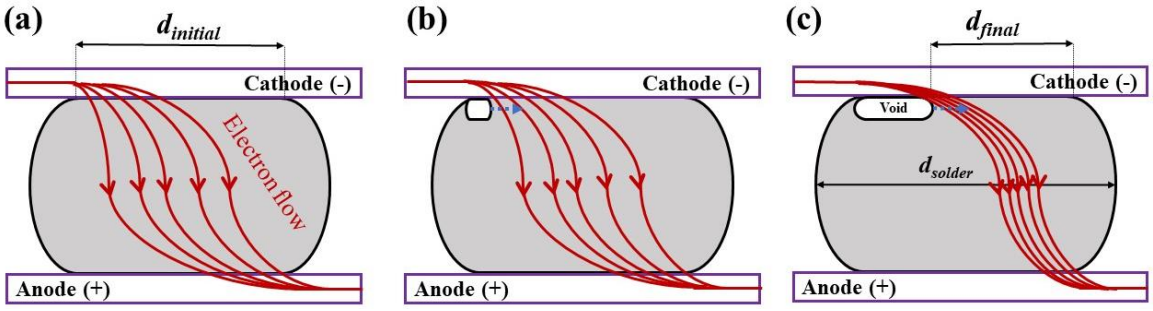

Figure 1.6: Current crowding in solder joints, showing (a) electron flow direction, (b) void nucleation, (c) void growing along the solder joint-metallization line interface. The final diameter is reduced, increasing the current density.

Real-time viewing of flip chip configuration solder joints can assist in understanding the failure mechanisms in solder joints by capturing joint interface evolution involving IMC growth and crack formation [36,37]. In the literature, real-time viewing methods involved SEM monitoring, requiring multiple interruptions to the electromigration test [38]. Other electromigration imaging techniques required destructive cross-sectioning of multiple flip chip samples to capture changes at different time intervals [31]. This process is time consuming and introduces sample-to-sample variation when comparing micrographs from different samples. Interruptions to an EM test might affect the MTF, similar to DC pulsing which is shown to increase the MTF [39]. Therefore, an inaccurate result could be obtained from such an experiment.

Yeh et al. [31] reported the current crowding phenomenon with electromigration for flip chip solder joints. The propagation of the interfacial voids was observed from cross-sectional studies of samples at 38 h, 40 h, and 43 h, respectively. Likewise, Yang et al. performed a similar experiment to document microstructural evolution, with five samples required to capture five time intervals [40]. Huang et al. designed a flip chip sample with 24 solder joints, but the SEM micrographs were only captured at a single time frame [41]. For all these studies, multiple samples were required for imaging, attributed to the destructive nature of cross-sectional imaging preparation. This procedure is tedious and increases the likelihood of sample failure during the imaging preparation process. Moreover, differences between the samples' initial microstructure are expected to impact the final results. A suitable real-time imaging method is required to help eliminate the aforementioned problems.

Lin et al. observed in-situ electromigration failure of a cross-sectioned PbSn flip-chip solder joint under SEM [42]. Current-stressing was interrupted four times to observe the specimen under the microscope. The test time was calculated by summing the current-stressing time, excluding the time elapsed during specimen observation. Thus, sources of error were introduced after each test interruption to allow the sample to reach a set stable temperature. Nevertheless, it was found that failure occurred in only 40 min, under a current density of 4×10^4 A/cm^2, supporting the significance of current crowding on EM failure and the important of in-situ imaging to capture EM failure.

Table 1.1: Examples of EM testing conditions seen in literature.

Article	Test Vehicle			Current Density		Temperature [°C]		MTF [h]	Result	Conclusion
	Description	Surface finish	Material	Solder Diameter, Current	Nominal (i.e. Current /Area) [A/cm2]	Simulation [A/cm2]	Ambient	Test Vehicle		
[12]	Metal Lines	-	Aluminum	11 -> 50 µm wide, 2,000 -> 20,000 Å thick	1×10^6	-	275	-	100 -> 800	Hillocks & Voids	MTTF Design Charts for Aluminum
[46]	Metal Line Contacts/Vias	-	Al, Cu, W	-	DC, Pulsed AC	-	-	-	-		EM depends on testing conditions, materials, pulsing. Fast EM tests as being
[11]	Flip-chip	UBM: Al/Ni(V)/Cu 2 µm thick	SnPb	100 µm, 0.2 A	2×10^3	2.25×10^4	125	-	43	Complete Failure/Open Circuit (OC)	Current Crowding 12x at ē entrance
[31]	Flip-chip with daisy chain	Coated with electroless plated Ni/Au	SAC405 SAC305	140 µm, 1.28 A 1.5 A 1.75 A	2×10^4 2.4×10^4 2.8×10^4	2.95×10^4 3.5×10^4 4.13×10^4	27	72 95 130	887 693 9.37	No Changes, Cracks observed, failure	TM > EM
[45]	Flip-chip with daisy chain	Cu/Ni(V)/Al	SnPb SAC405	100 µm, 1.7 -> 1.8 A	$3.5 \times 10^{3->}$ 3.7×10^3	5.1×10^4	50	-	-	Void Formation	TM + UBM Dissolution as Failure Mechanisms
[44]	Single Bump & Daisy Chain	Ni/Au, OSP, etc.	-	250 mA -> 1.5 A	$3 \times 10^{3->}$ 2×10^4	-	Max 110	-	-	10 -> 20 % resistance change	Many factors play a role. Need to record them
[33]	Flip-chip with daisy chain	Ni	SAC405	320 µm, 10A	2.04×10^4	-	25	81-85	500	No OC	Black's eq not applicable to solder joints, 3 Failure types
[2]	On-die power grid	-	Cu interconnect	-	-	-	-	-	-	-	Physics-based EM tool
[34]	Flip-chip with daisy chain	ENEPIG & OSP	SAC305	300 µm	1×10^4	-	150	-	500	Grain Rotation (GR)	GR as a tool for life prediction
[43]	Flip-chip with microbumps	Cu 5 µm/Ni 3 µm	Sn2.5Ag	18 µm, 0.2 A	9.2×10^4	-	150	155	192.3	IMC Formation, No OC	Failure mechanism: Sn diffusion (not EM)

1.3 Scope and objectives

Research is focused on EM in flip chip solder joints, with flip chips regarded as a field of exceptional growth in packaging technology [13,24]. However, due to the miniaturized solder interconnects in flip-chip configuration, EM is a growing concern, and the electronic packaging industry is starting to face challenges in obtaining consistent reliability in solder joints [2,16,18,47]. Some defects were previously tolerated in larger solder joints, with a diameter greater than 300 μm, as the defects take up a relatively small percentage of the joint. However, for a smaller joint, the defects are still the same size, thereby taking up a larger percentage of the joint. Thus, the defects which, previously tolerated, are currently not tolerated as they take up a relatively larger area of the now smaller device [9]. Thus, with the shrinking microelectronic devices, the maximum tolerable current densities have also been decreasing for these devices. Ultimately, EM is a reliability concern as it causes permanent degradation of conductors often followed by a runaway failure mechanism resulting in fast complete failure of the joint. Certain applications, such as space travel, medical devices and military equipment, require high levels of reliability and small margins of error [10]. Thus, there is an urgent need to tackle EM.

As shown in the previous section, in the present literature, EM testing methodology involves current stressing of a sample which is often complemented with in-situ resistance measurements. The resistance change is the main failure criterion, with cross-sectional micrographs being used as an optional step, involving destructive testing, to observe microstructural changes. This methodology is useful to predict EM failure times but fails to explain the physics behind the phenomenon of EM.

Thus, the main objective of this research is to 1) allow in-situ monitoring of the electromigration process, 2) provide a constant condition under which EM proceeds, 3) obtain repeatable test results at short testing times. This is achieved by designing a test sample that can be cross-sectioned in a non-destructive process, leaving the resistance measuring circuit intact. This proposed methodology would provide a more detailed failure analysis, providing a better understanding of electromigration. Therefore, real-time visuals obtained during electromigration testing could be useful to learn more about the effects of unique features of solder joints, such as geometry, metallurgy, anisotropy of Sn, etc. on joint reliability and help mitigate electromigration.

Real-time viewing of electromigration in solder joints provides the ability to observe cracks and voids and determine the initial location of void formation and direction of propagation, and verify any defects caused solely by EM and not due to manufacturing processes as described in flip-chip test vehicle preparation e.g. [33]. Furthermore, [27] has highlighted the importance of determining "the prevalence of either failure mode – nucleation vs. growth" which potentially can be determined by in-situ monitoring of a solder joint [33]. JEDEC JEP154 [11] guidelines were followed for the experimental method, including the preparation of the daisy chain test structure, choice of stressing conditions and the method for temperature measurement. Additionally, real-time viewing was used to complement the failure analysis stated in JEP154.

Equally important is the use of cross-sectioning during sample preparation prior to the real-time visual tests, which decreases the cross-sectional area and consequently increases the current density across the solder joints. This results in truly accelerated EM testing, the results of which could be used to determine the upper failure criteria limit in the test vehicles. Similarly, the effect of various variables on EM MTF, such as solder geometry, material composition, and surface finish, could be studied at an accelerated pace. Furthermore, different test vehicle designs could be developed and tested using this methodology to optimize certain parameters and increase reliability.

Chapter 2. Sample preparation and simulation

In order to observe electromigration in solder joints, a test vehicle has to be prepared that resembles commercial flip-chip solder joints. Additionally, the test vehicle ought to be designed to induce electromigration, while minimizing the effects of Joule heating. The design requirements as well as the process development are highlighted in this section. The term 'test vehicle' refers to the PCB and solder joints. The term 'specimen' refers to the material producing the signal which is the solder joint. In this chapter, two test vehicles are described, with the second being an improvement over the first.

2.1 PCB design requirements

The PCB design must follow these requirements to ensure a properly functioning test vehicle:

1) A multitude of channels to be designed to measure the resistance across a number of solder joints, which are formed in a daisy chain configuration
2) Withstand high current density ($10^4 - 10^5$ A/cm^2 for SAC305)
3) Withstand high temperatures, occurring from Joule heating and high ambient temperature testing
4) Limit current crowding to reduce sample-to-sample variations
5) Ensure EM occurs only in solder joints and avoid EM in PCB copper traces
6) Allow for current flow even after cross-sectioning
7) Allow for easy reflow with proper surface finish selection

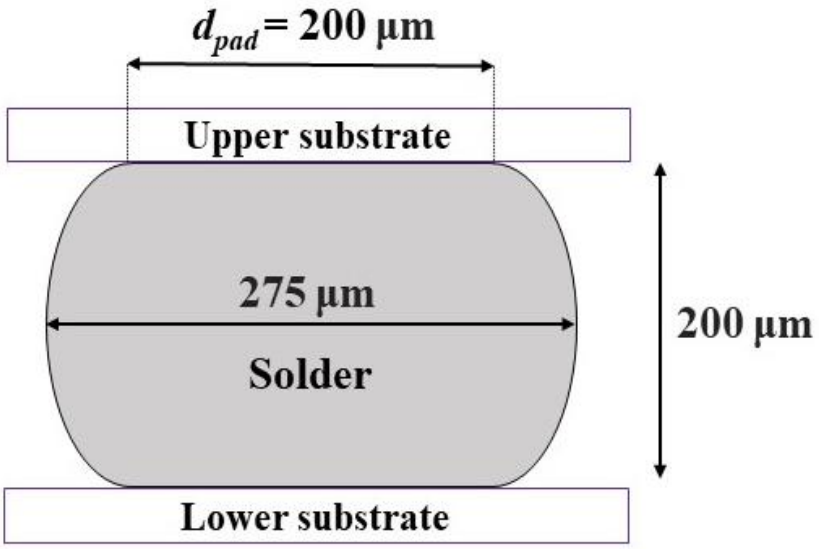

Figure 2.1: Design requirements for selection of solder joint and pad size. Typical geometry of test vehicle for solder joint diameter of 250 µm after reflow.

The most important design requirement is the solder joint diameter, and consequently, the size of the PCB pad both of which are designed small enough. In order for EM to occur, the required current density has to be reached. The current value is limited by the availability of a power supply that can deliver high current, the ability of the test vehicle connectors and traces to withstand high current without fusing, and the solder joint diameter. It is the goal of the design to make the solder joint the weak link, failing first when the current level is increasing.

As mentioned, the solder joint diameter and pad size directly affect the current density. A solder joint diameter of 250 µm was selected as this was the smallest available diameter available in a product on the market (Chipquick SMD2020). According to design requirements, a joint diameter of 250 µm would require a pad diameter of 200 µm, so the pad size was designed accordingly [48]. In flip chip configuration, the upper substrate usually is a silicon chip and lower is a high density PCB or an interposer. However, for this test vehicle, both substrates are PCBs with a typical thickness of 1.2 mm. The assembly, after reflow, is designed to look similar to Figure 2.1.

2.2 Test vehicle 1: eight solder joints

The first test vehicle design was fabricated by Supplier 1 (Markham, Canada). The devices under test (DUTs) are solder joints produced between custom PCBs, forming a test vehicle for convenient handling in the experiments. The custom PCBs are two daughterboards connected to a single motherboard to form a flip configuration, as shown in Figures 2.2 (a) – (c). The daisy chain design has 8 solder joints, as illustrated in Figure 2.2 (d). Two signals (channels) were obtained from each solder joint: one including the resistance of some copper lines, the other without copper line resistance. Thus, there were a total of 16 channels, 8 odd and 8 even, to allow for resistance measurements across different sections of the flip configuration. The even channels were used to measure the resistance of the "solder-line specimens" which are the top and bottom copper traces as well as the solder joints, as shown by the "CH 1" contacts in Figure 2.3 (a). The odd channels were used to measure the resistance of the "solder specimens", directly across the solder joints, as shown by the "CH 2" contacts in Figure 2.3 (a). The flow of current is indicated by the red line in Figure 2.3 (b). Close-ups with more details on an even and an odd channel are given in Figures 2.3 (c) and (d), respectively.

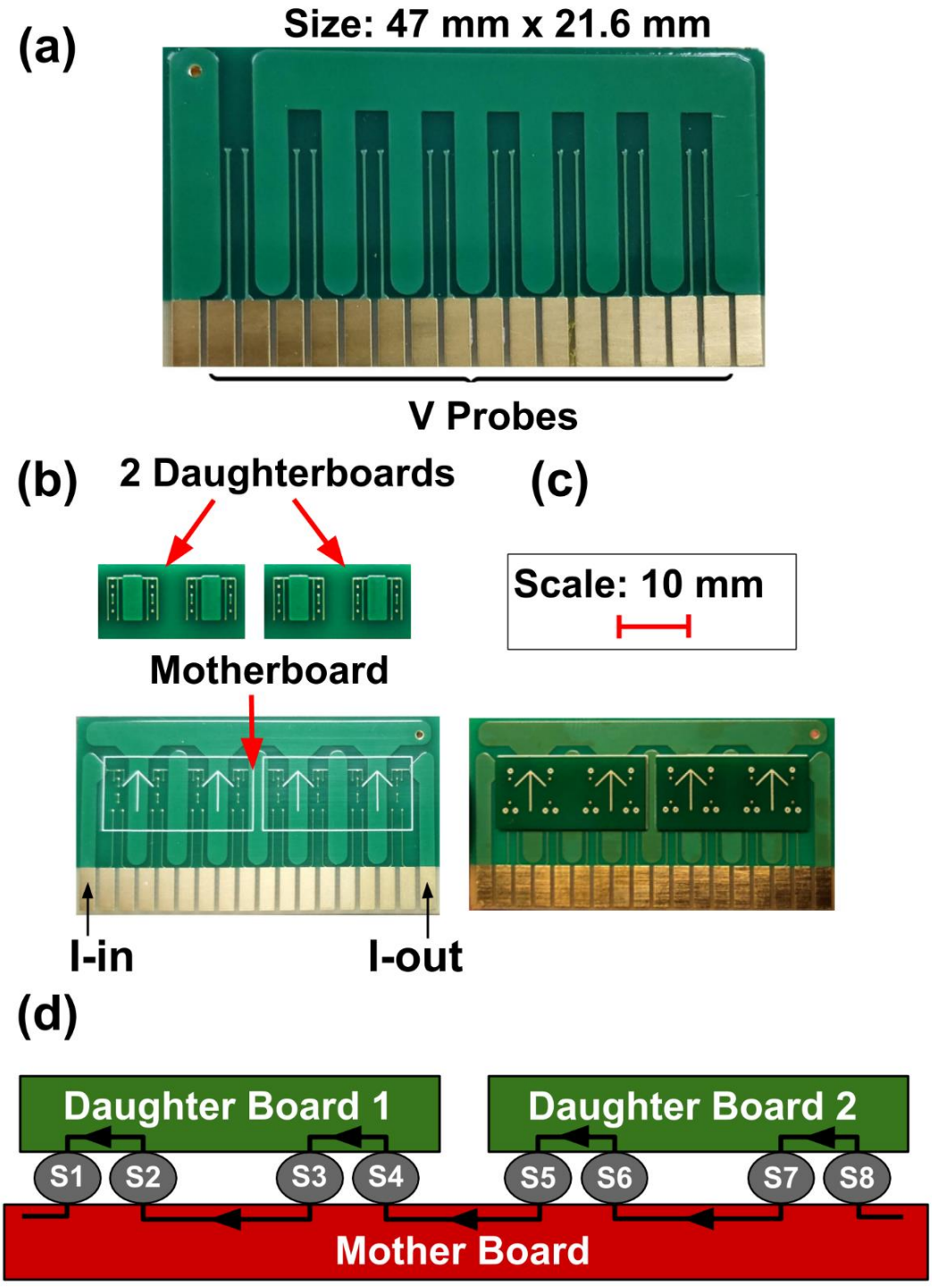

Figure 2.2: (a) Bottom side of motherboard showing voltage probe pads. Flip configuration consists of two daughterboards soldered onto motherboard using SAC305 solder. Figure shows top side of components (b) before and (c) after bumping and reflow processes, and (d) cross-sectional illustration of flip configuration [49].

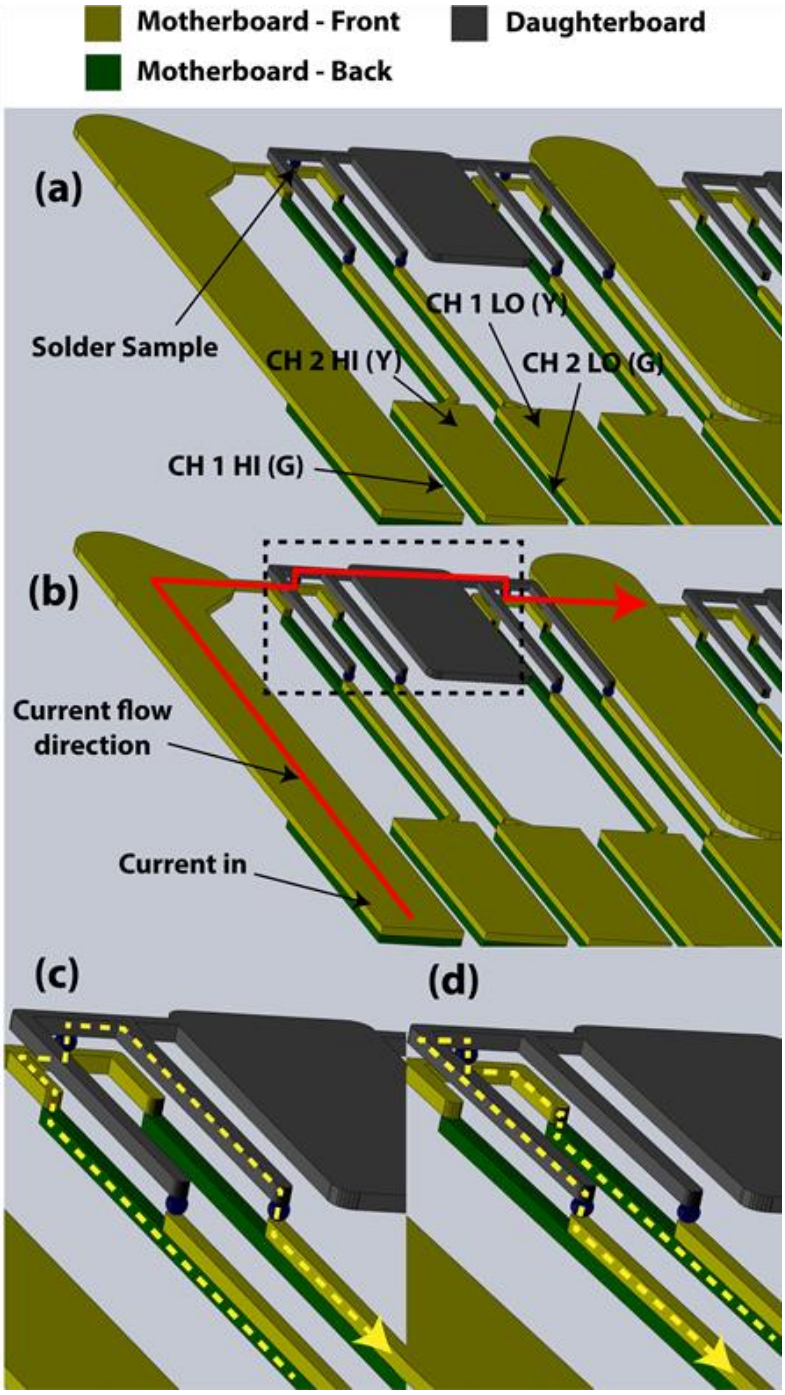

Figure 2.3: 3D visualization of flip chip channel configuration. Flip configuration consists of 16 channels evenly split between even and odd channels. (a) Channel configurations, showing example of CH 1 (solder) and CH 2 (solder-line) (b) Current flow direction starting from motherboard to daughterboard and back. (c) Even channel configurations measure resistance of copper traces as well as that of solder sample. (d) Odd configurations measure resistance of solder sample alone [49].

2.2.1 Solder joint simulation

To ensure that the required current densities are reached, and to gauge the level of Joule heating in the solder joint, current density simulations were developed for a full solder joint and half a solder joint, respectively. Additionally, the metallization line thickness and width were varied to study their effect on current crowding. The joint diameter at the top, middle, and bottom were 200 μm, 275 μm, and 200 μm, respectively. The length of the top and bottom copper lines were kept constant at 500 μm, respectively. Two thicknesses of 34.8 μm and 174.0 μm were used for the copper lines, corresponding to copper weight of 1 oz and 5 oz, respectively. Additionally, two widths of diameter 200 μm and 400 μm were used. Although ENIG surface finish used in the PCB design, the simulation was simplified to include copper only, since the PCB consisted of small amounts of nickel (3.8 μm) and gold (0.1 μm), and the material parameters are similar, as shown in Table 2.1. The boundary conditions were set such that 5 A of current flowed from the terminal to the ground using the DC current model. The software used was Comsol 5.5. Comsol's 'extra fine' element size was used and the simulation was built based on the physics-controlled mesh, similar to Figure 2.4. The simulation files can be found on Google Drive[1].

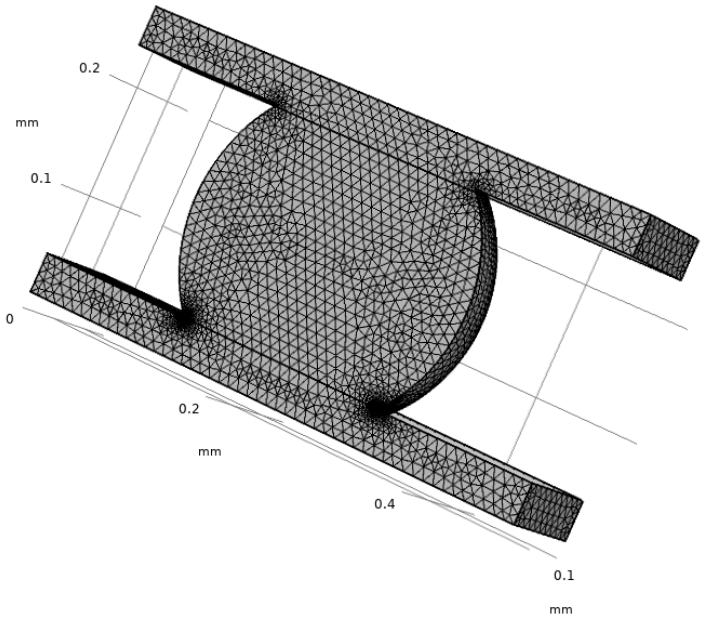

Figure 2.4: Simulated dimensions of half solder joint showing the mesh, simulating cross-sectioning.

[1] https://drive.google.com/drive/folders/1XwL_Iud0WLyswbLjMul1dFciiL1lpSCq?usp=sharing

Table 2.1: Material parameters used for simulation using built-in material library in Comsol

Material	**Cu**	**SAC305** [50,51]	**Au**	**Ni**
Electrical conductivity [S/m]	5.81×10^{7}	9.63×10^{6}	4.56×10^{7}	1.38×10^{7}
Coefficient of thermal expansion [1/K]	1.65×10^{-5}	2.35×10^{-5}	1.42×10^{-5}	1.34×10^{-5}
Heat capacity at constant pressure [J/kg.K]	3.84×10^{2}	2.32×10^{2}	1.29×10^{2}	4.45×10^{2}
Density [kg/m^3]	8.96×10^{3}	7.39×10^{3}	1.93×10^{4}	8.90×10^{3}
Thermal conductivity [W/m.K]	4.01×10^{2}	5.87×10^{1}	3.17×10^{2}	0.907×10^{2}
Young's modulus [Pa]	1.2×10^{11}	4.1×10^{10}	7.0×10^{10}	2.19×10^{11}
Poisson's ratio [1]	3.4×10^{-1}	3.3×10^{-1}	4.4×10^{-1}	3.1×10^{-1}

2.2.1.1 Varying solder dimensions

The current density across a solder joint is generally non-uniform [52]. Therefore, a current density simulation was performed to obtain the value and location of the maximum current density in the solder joint. To understand the phenomenon of current crowding, different geometries of the solder joint and metallization lines were simulated: full joint, half joint, thick line and wide line, as shown in Figures 2.5 (a) – (d). The dimensions of all the geometries are shown in Table 2.2. Figure 2.5 (a) shows the current density distribution of the reference full solder joint, with the maximum value at the corner of the solder joint. Figure 2.5 (b) shows the increase in the current density when the solder joint is cross-sectioned. Compared to the normal metallization line thickness corresponding to 1 oz Cu, the line with a thickness corresponding to 5 oz Cu decreased the maximum current density from 3.51×10^5 A/cm^2 to 1.25×10^5 A/cm^2, as shown in Figure 2.5 (c). Similarly, the current density was decreased with wider lines, as shown in Figure 2.5 (d). The results agree with those shown in [53]. The effect of mesh density on the maximum current density is shown in Figure 2.6.

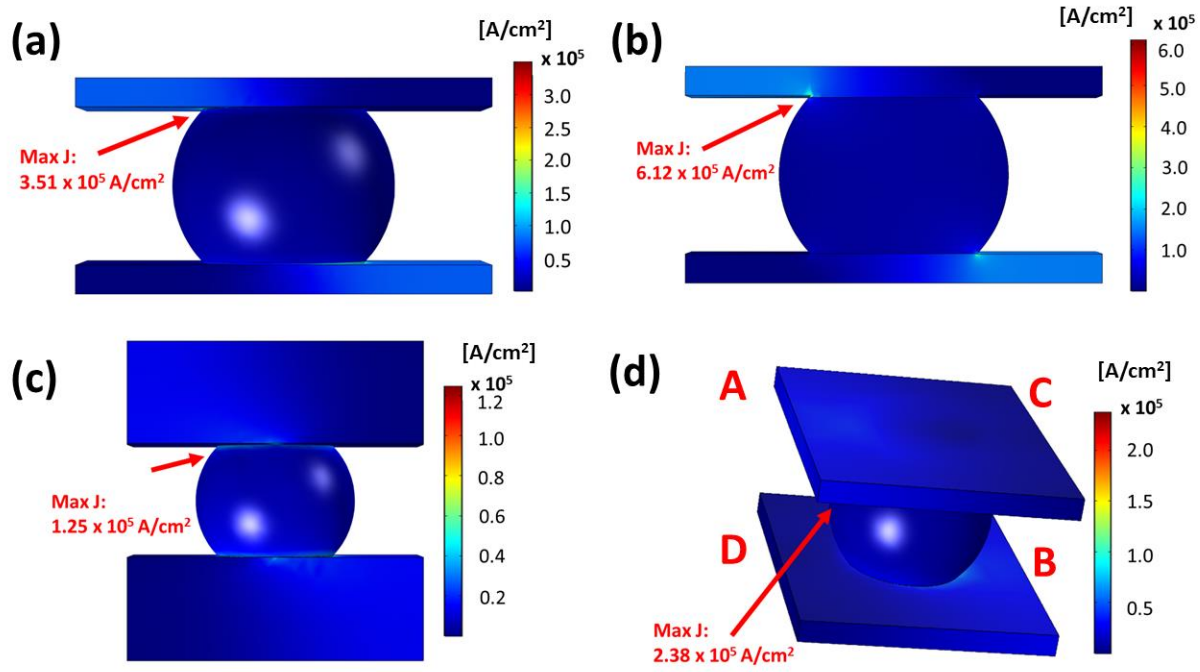

Figure 2.5: Current density simulation. Magnitude of the applied current was 5 A. The maximum solder diameter and height are 275 µm and 200 µm, respectively. Simulation shows (a) reference solder joint with 1 oz Cu and 200 µm wide lines (b) cross-sectioned solder joint (c) thick solder joint with 5 oz copper (d) 400 µm wide solder joint. Location of maximum current density always at interface corner adjacent to current source. Current flows from top-left corner (A) to bottom-right one (B).

Table 2.2: Results of simulation for different geometries. Applied current was 5 A, corresponding to a nominal current density of 1.59 x 10^4 A/cm^2 according to the JEP154 standard [11].

Case	Metallization line		Maximum current density [A/cm^2]	Resistance (voltage drop for 5 A)	
	Thickness [µm]	Width [µm]		Across current flow terminals [mΩ]	Across solder joint [mΩ]
Reference	34.8	200	3.51 x 10^5	1.25	0.648
Cross-sectioned	34.8	200	6.12 x 10^5	2.51	1.29
Thick line	**174.0**	200	1.25 x 10^5	0.662	0.533
Wide line	34.8	**400**	2.38 x 10^5	0.747	0.557

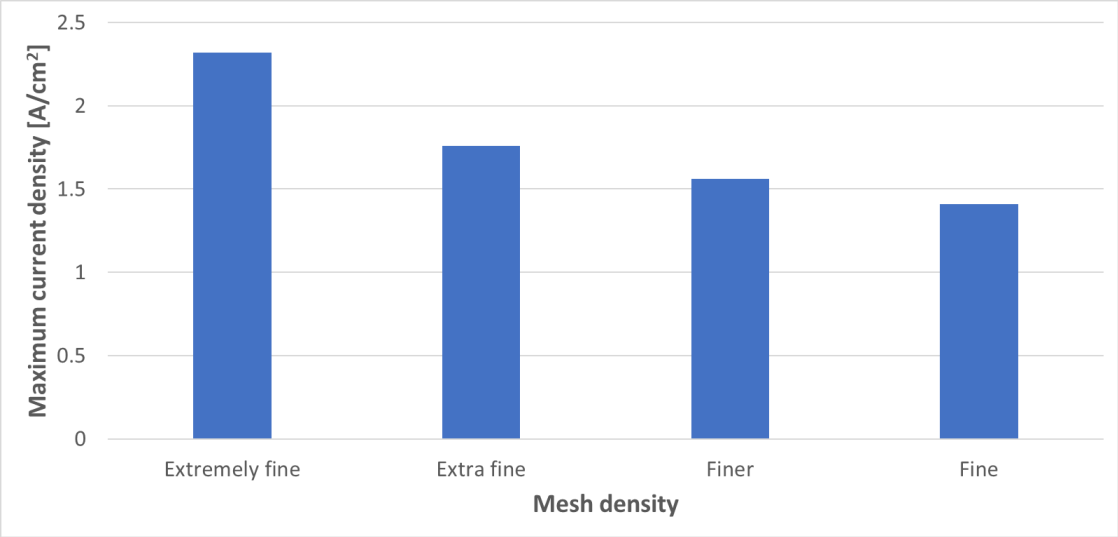

Figure 2.6: Effect of mesh density on maximum current density, showing an increase in current density with finer mesh densities.

2.2.1.2 Cross-sectioning and temperature gradient

To understand the current distribution across the cross-sectioned solder planes, simulations using contour plots on slice planes were performed, as shown in Figures 2.7 (a) and (b). This simulation was performed to locate the plane with the highest current density. The magnitude of the applied current was 5 A. Another simulation was performed on a solder joint bisected in half, revealing the central plane in which the cross-sectional imaging was performed, as shown in Figure 2.7 (c). As expected, current crowding occurred at the location of electron entrance and exit, with a maximum current density of 6.12×10^5 A/cm^2, as shown in Figure 2.7 (c). The maximum current density occurred at the cross-sectioned plane. The current distribution was similar to the skin effect seen in alternating current. The results from this simulation highlight the significance of the presented real-time imaging methodology which is likely to capture microstructural changes in the plane with the largest current density.

Similarly, another simulation was performed to determine if thermomigration would occur for an applied current level of 5 A for the cross-sectioned solder joint (filename "V2_cross-sectioned_temp_gradient"). The Joule heating module was used which was part of the DC current

model. The surfaces are isolating and the non-stressed Cu traces were set at room temperature to study the effect of Joule heating on the current stressed portions of the joint. Looking at the literature, large temperature gradients of ~100 K/mm are required for thermomigration to occur [19]. Comparing the previous value with those in Figure 2.7 (d), there is a possibility that thermomigration would impact the experimental results, since the maximum value was 230 K/mm. Therefore, the test result failure mechanisms would entail both electromigration and thermomigration. However, this value occurred at the current crowding location, and the temperature gradient was more uniform throughout the solder joint. Nevertheless, it is concluded that thicker copper lines are required to decrease current crowding and consequently limit temperature gradients.

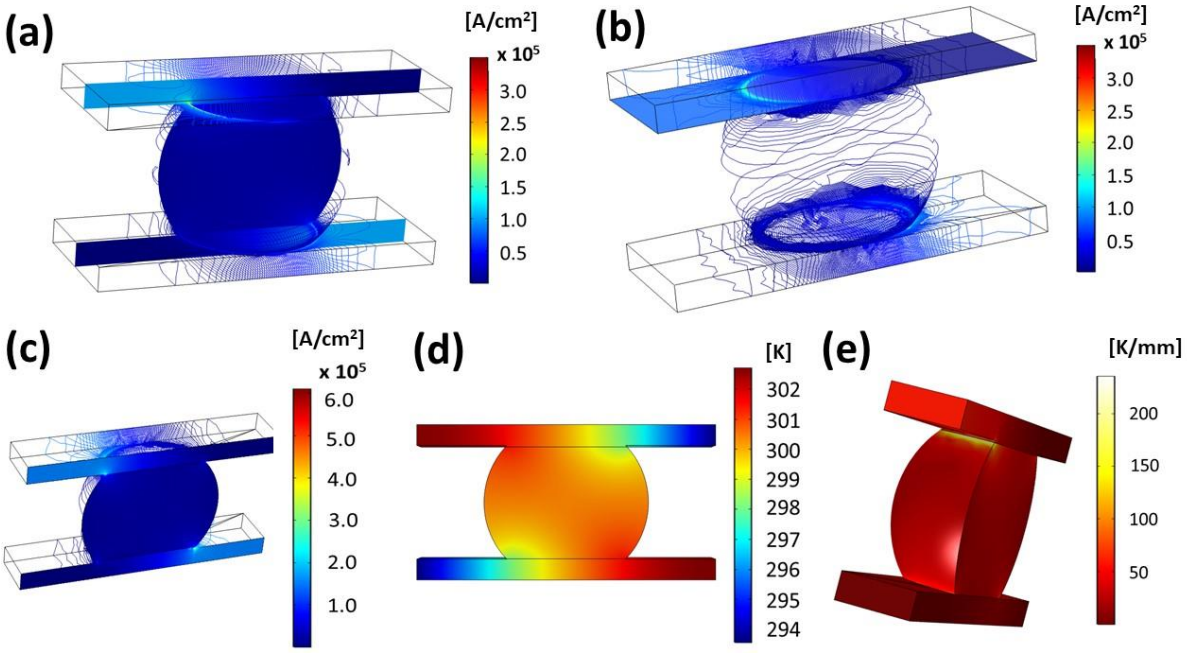

Figure 2.7: Current density simulation showing (a) contour plot on middle plane, showing the largest current density in this plane (b) contour plot on top interface (c) simulation of the cross-sectioned plane (d) temperature gradient across different sections of solder joint, revealing high gradients at the current crowding location. Current flows from top-left to bottom-right corner.

2.2.2 Bumping and reflow processes

The solder formation process consisted of two steps: the bumping process of the daughterboards and the reflow process of the daughterboards onto the motherboard. Two methods were developed for the bumping process of the solder joints onto the daughterboard. The first method involved the use of 250 μm solder balls, and the second method involved the use of stencil printing using solder paste. The bumped boards were then assembled either manually using a hot plate, or automatically using a die bonder. The results of the assemblies obtained from both methods were then characterized by measuring the resistance across all channels.

2.2.2.1 Solder balls

The first method involved the use of Chipquik SMD 2020 - 25000, 0.010" (0.254 mm) diameter Sn96.5/Ag3.0/Cu0.5 solder balls[2], as shown in Figures 2.8 (a) – (f), following a strict procedure:

(a): Apply "Rosin Flux MG Chemicals #835-P" on daughterboard

(b): Manually place solder balls on daughterboard pads, as shown in Figure 2.9

(c): Reflow daughterboards on a hot plate for 5 min at 275 °C

(d): Apply flux on motherboard

(e): Place daughterboards on the motherboard then apply high-temperature (Kapton) tape around the white rectangular borders inside the motherboard. The tape prevents movement of the daughterboards during reflow.

(f): Place assembly on the hot plate for 5 min at 275 °C

Once the procedure is complemented, a conductivity test using a DMM is conducted to determine if the assembly was successful.

[2] Available from Chipquik (Ancaster, Canada): https://www.chipquik.com/store/product_info.php?products_id=1100034

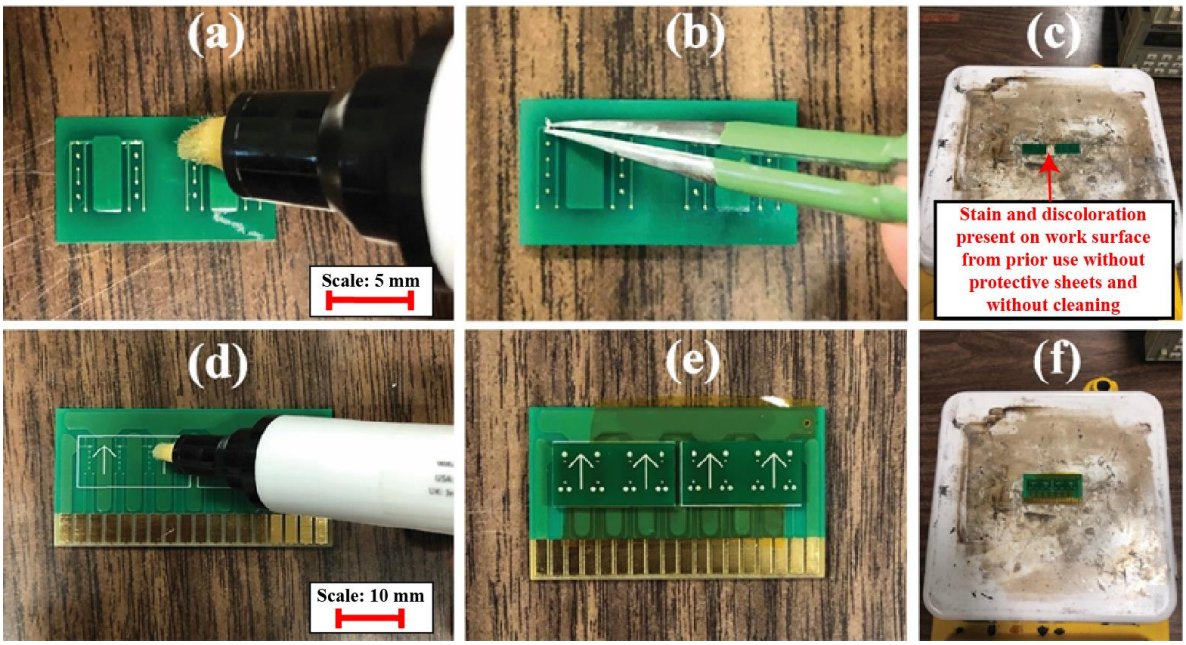

Figure 2.8: Solder ball bumping process, showing steps (a) to (f). The terminal pitch is 2.54 mm.

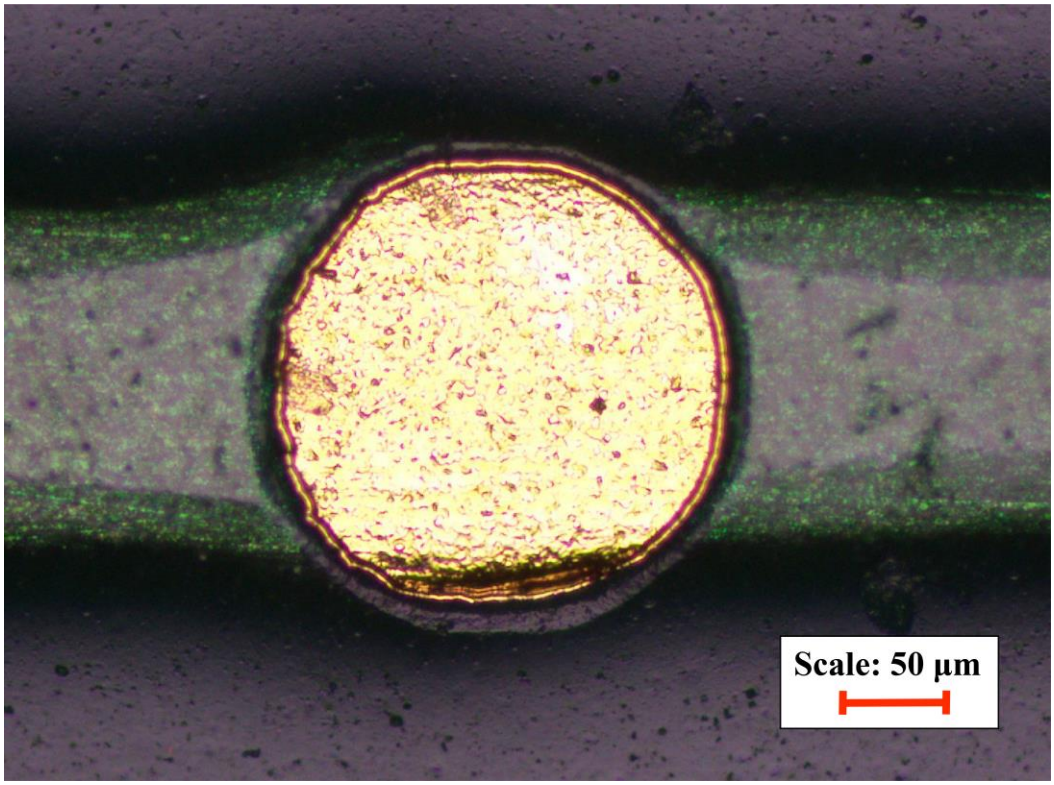

Figure 2.9: Micrograph of solder pad on daughterboard. The measured diameter of the pad opening is 208 µm.

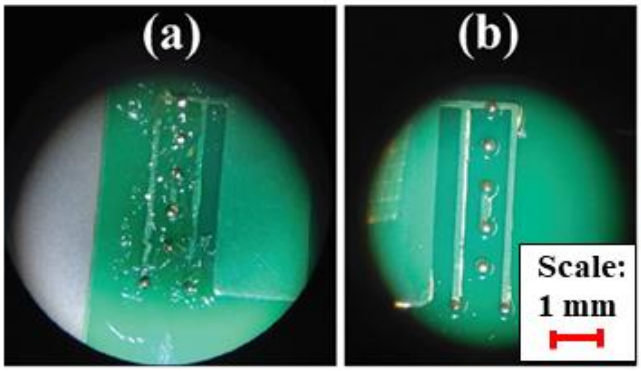

Figure 2.10: Comparison of different flux types, showing (a) RA Rosin Flux Paste – 8342 and (b) MG Chemicals Rosin Flux pen #835-P.

A series of steps were shown to optimize the manual bumping and reflow processes:

- The use of a flux pen instead of flux paste; the flux paste applied an uneven layer, shown in Figure 2.1 (a), compared to the flux paste which applied an even layer, improving the reliability, as shown in Figure 2.1 (b).
- Heating the assembly from the bottom upwards, as opposed to heating the entire assembly at once inside an oven. The former allows for the solder balls to melt, starting from the bottom, which ensured a connection was formed between the solder joint and PCB pad.
- The use of Kapton tape for the accurate placement of the daughterboards onto the motherboard.

2.2.2.2 Solder paste

A stencil, which had holes of diameter 12 mils, was developed for the stencil printing process shown here and in Figures 2.11 (a) – (g). The daughterboard stencil is shown in Figure 2.12.

(a) Scoop solder paste from original container into a petri dish.
(b) Place daughterboard into fixture.
(c) Locate solder pads with stencil and use alligator clips to fix stencil in place.
(d) Lay solder paste onto stencil.
(e) Spread solder paste across the stencil using the solder paste spreader and scrape off excess.

(f) Remove daughterboard, use tweezers if necessary.

(g) Reflow assembly using the motherboard fixture

After the procedure was completed, the PCB stencil was cleaned using lint-free wipes (Kimwipes) and isopropyl alcohol (IPA).

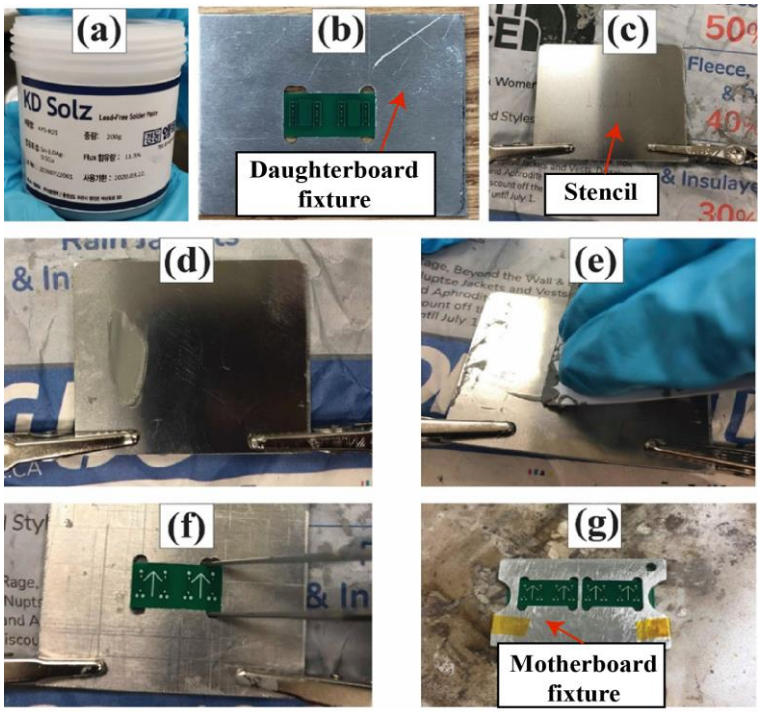

Figure 2.11: Solder paste process, showing steps (a) to (g).

Figure 2.12: Illustration of daughterboard stencil. Stencil was manufactured using stainless steel. Dimensions are 2.162 inches by 1.712 inches, with a thickness of 4 mils. Stencil holes have a diameter of 12 mils.

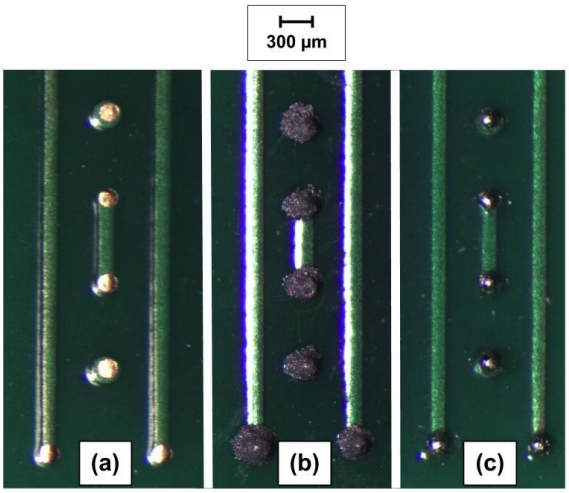

Figure 2.13: Bumping process of solder joints, showing daughterboard (a) before stencil printing (b) after printing and (c) after reflow.

For the solder, KD Solz solder paste (KD MTEC, South Korea) was used which is SAC305 (Sn 96.5%, Ag 3.0%, Cu 0.5%), with 11.5% flux by weight, as shown in Figure 2.13.

It was concluded that the solder ball bumping process was the faster of the two processes, roughly by a factor of 3. Furthermore, many issues were encountered with stencil printing:

- One or more solder pads often observed to be missing solder. In this case, the daughterboard had to be completely cleaned and the process was repeated.
- In some cases, the daughterboard did not fit inside the fixture. The daughterboard was sanded on either end. Careful attention was taken to ensure accurate alignment with motherboard.
- Solder paste moved when removing stencil. Alligator clips were used to clamp down the stencil onto the fixture.
- Leftover solder paste blocked some of the holes in the stencil once the stencil was removed after screening. To solve this problem, the stencil was cleaned with IPA and the holes were examined under a microscope to ensure they were free of any paste.

After multiple iterations of this process, it was observed that one screen pass was more effective than multiple passes as multiple passes applied an excess amount of solder on the pads. Similarly, roughly 2.5 mL of solder paste was enough for each daughterboard.

2.2.2.3 Tresky die bonder

After reflow of the daughterboards, a Tresky T-3000-FC3 die bonder was used for the test vehicle assembly. The two daughterboards were flipped, placed next to a motherboard on the machine, picked by the machine, aligned, and placed on the motherboard using a bonding force of 30 N, which was applied at a temperature of 260 °C and held for 5 min, as shown in Figures 2.14 (a) – (e).

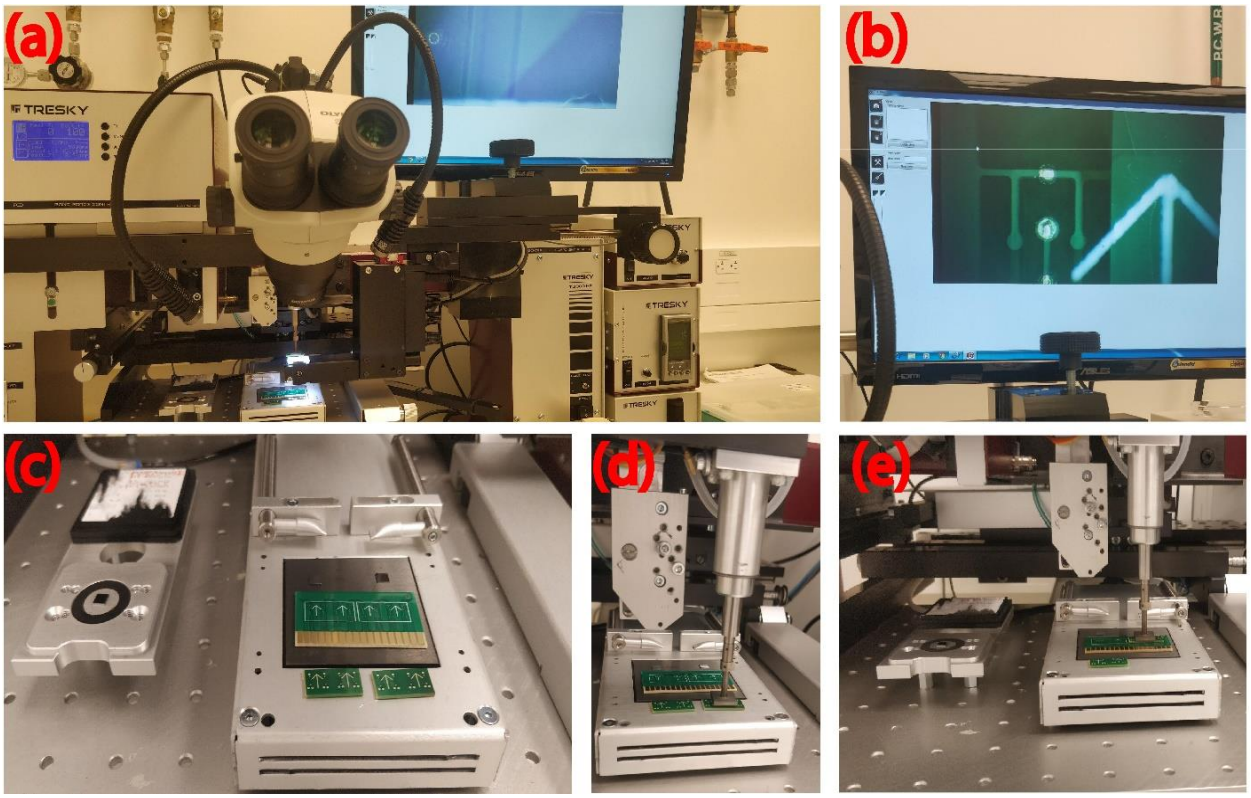

Figure 2.14: Tresky T-3000-FC3 die bonder machine, showing (a) machine platform (b) superimposed images of daughter- and mother- boards (c) motherboard placement on heating plate (d) pick and place tool (e) reflow process.

2.2.3 Details of assembly

Electroless nickel immersion gold (ENIG) was chosen as a surface finish for the solder pads. Details are given in Table 2.3. A cross-sectional view of the test vehicle as viewed under a microscope is shown in Figure 2.15. The thickness of all PCBs was 1.2 mm. Solder resist material thickness was kept at 20 µm over copper tracks and 30 µm on the bare PCB surface. The average diameter and height of the bumped solder joints, using the solder ball bumping process, were 305 µm and 129 µm, respectively. The diameter of the copper pad on the daughterboards was 200 µm.

Table 2.3: Surface Finish Parameters

ENIG Surface Finish	
Material	Nominal Thickness (µm)
Copper	25.4
Nickel	3.81
Gold	0.05-0.10

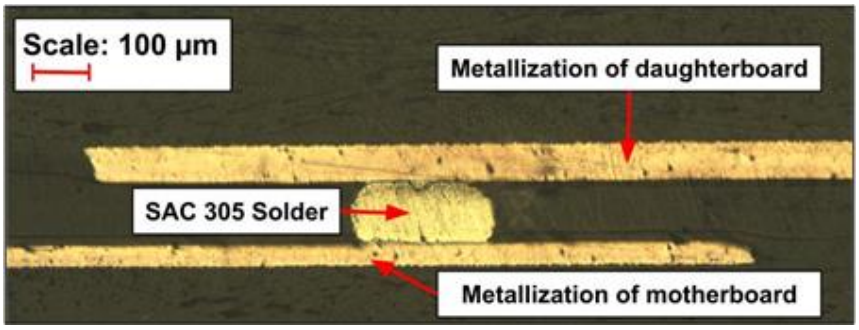

Figure 2.15: Cross-sectional morphology of solder joint on test vehicle showing parts of daughterboard, SAC305 solder, and motherboard.

2.2.4 Resistance characterization

To ensure the reliability of the test vehicle, resistance measurements were taken for all solder joints in the test vehicle, prior to current stressing. All samples had very similar resistance values, as shown in Table 2.4. Each sample consists of 8 "solder line" and 8 "solder only" signals. Since both methods yielded similar results, the solder ball bumping was used since it was faster. The mean of the mean of the odd and even channels were 0.36352 and 2.73868 mΩ, respectively. Thus, percentage errors of up to 15 % can be expected from these results, which are attributed to differences in solder joint geometry, placement precision of solder joints, etc.

Table 2.4: Different measurements of the 6 samples. The room temperature was 22 °C. The level of the probing current was 100 mA. Thermoelectric electromotive force (EMF) characterization measurements were not performed which could impact the resistance data.

Sample	1	2	3	4	5	6
Mean odd (solder only) [mΩ]	0.32994	0.39619	0.34506	0.33759	0.38135	0.39098
Mean even (solder-line) [mΩ]	2.78384	2.77072	2.70799	2.70015	2.73612	2.73326
Std Dev (odd) [mΩ]	0.04644	0.07155	0.02183	0.03093	0.06075	0.03358
Std Dev (even) [mΩ]	0.1632	0.08968	0.06541	0.0746	0.07267	0.0888
Min. resistance [mΩ]	0.27197	0.2931	0.31485	0.27771	0.30836	0.32375
Max. resistance [mΩ]	3.06215	2.95695	2.84178	2.81408	2.84622	2.85969

2.2.5 Test vehicle preparation for cross-sectional viewing

To prevent breakage of the solder joint connections during the grinding process, the test vehicle was encapsulated in epoxy using the "ClaroCit Kit" brand (available from Struers)[3], as shown by the sequence of images in Figures 2.16 and 2.17. The test vehicle was then ground sequentially using silicon carbide paper from 240 to 1200 grit and polished using alumina powder of micron sizes 1.0, 0.3, 0.1 and 0.05, respectively. A Pt1000 temperature sensor was attached with thermally conductive paste (TG-S606B silicone based thermal grease, t-Global Technology) to the surface of a cross-sectioned solder joint near the solder joint that was being imaged, as illustrated in Figure 2.17 (b).

[3] https://eshop.struers.com/US/EN/products/Mounting/Cold_mounting_resin/ClaroCit_Kit_800_g_powder_500_ml_liquid_and_required_consumables(40200072).aspx

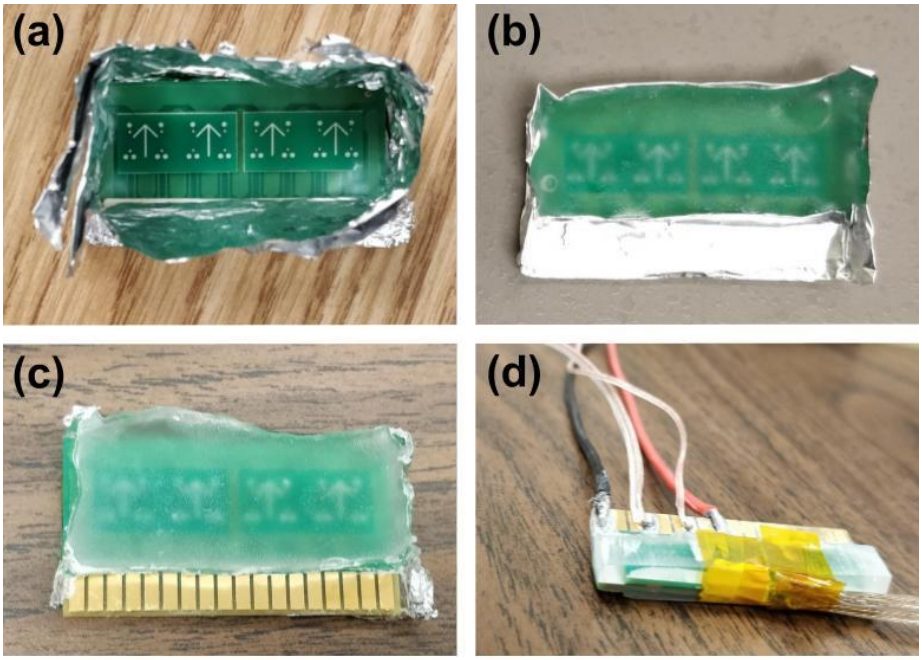

Figure 2.16: Sample preparation for cross-sectional viewing procedure. (a) Pads were covered with aluminum foil to prevent epoxy formation on pads (b) epoxy after curing (c) removal of foil, and (d) Pt1000 temperature sensor attached to sample along with voltage and current connections.

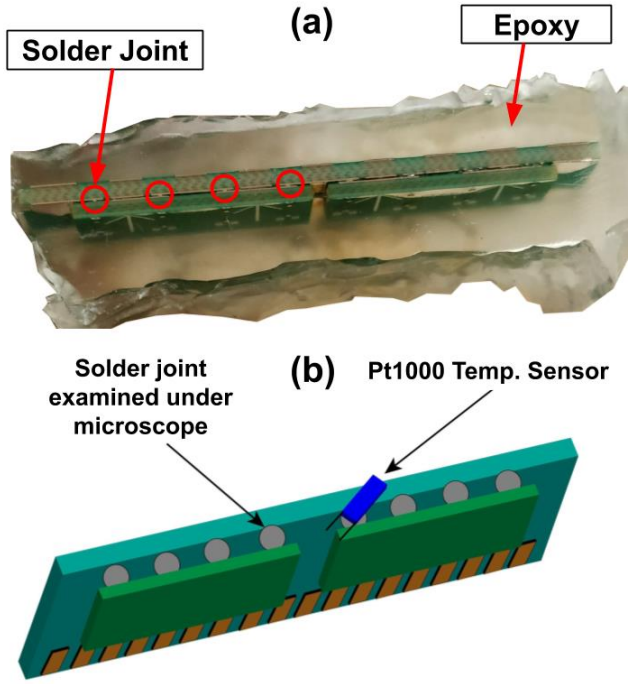

Figure 2.17: Test vehicle after epoxy curing, showing (a) location of solder joints on left daughterboard and (b) schematic of test vehicle showing location of temperature sensor when current stressing is applied.

2.3 Test vehicle 2: two solder joints

The second test vehicle was designed to allow for higher current densities across the solder joints. Photographs of the boards are shown in Figures 2.18 (a) and (b) before and after soldering, respectively. The layout is shown in Figure 2.18 (c). The same pad diameter and solder material as that in test vehicle 1 were used. However, the second test vehicle was designed to have wider current lines and fewer joints, providing a large distance between the solder joints to thermally separate the joints and reduce Joule heating. When inspecting the size of the solder pads, as shown in Figure 2.18 (d), it was found to be substantially larger than in the design (Figure 2.19), indicating a discrepancy between layout and actually produced PCB.

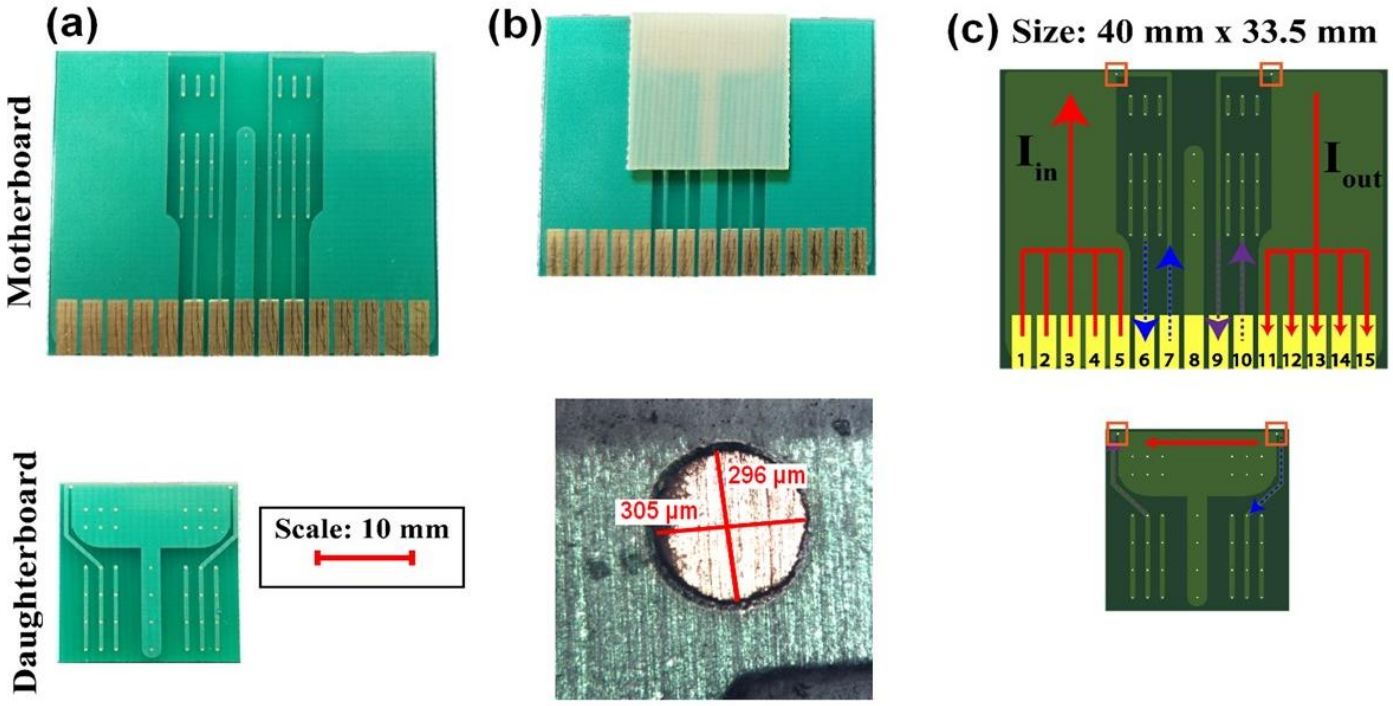

Figure 2.18: Second variation of test vehicle consisting of motherboard and daughterboard, showing (a) photographs of bonding sides with 42 solder pads each board, (b) assembly with daughterboard flipped onto motherboard and a close-up of an example solder pad, and (c) layout indicating current direction and voltage probe pads. Current direction is shown in red and voltage drop for left and right solder joints is shown in blue and purple, respectively. Location of current-stressed joints (DUTs) is inside orange squares. Only one of the joints DUT was cross-sectioned before EM testing.

The electrical layout created using KiCAD version 5.1.9 is shown in Figures 2.19 (a) and (b) for the motherboard and daughterboard, respectively. Only two solder joints were current stressed, which were located at the top of the test vehicle. Furthermore, there were multiple solder joints spread throughout the motherboard to resist the weight of the daughterboard.

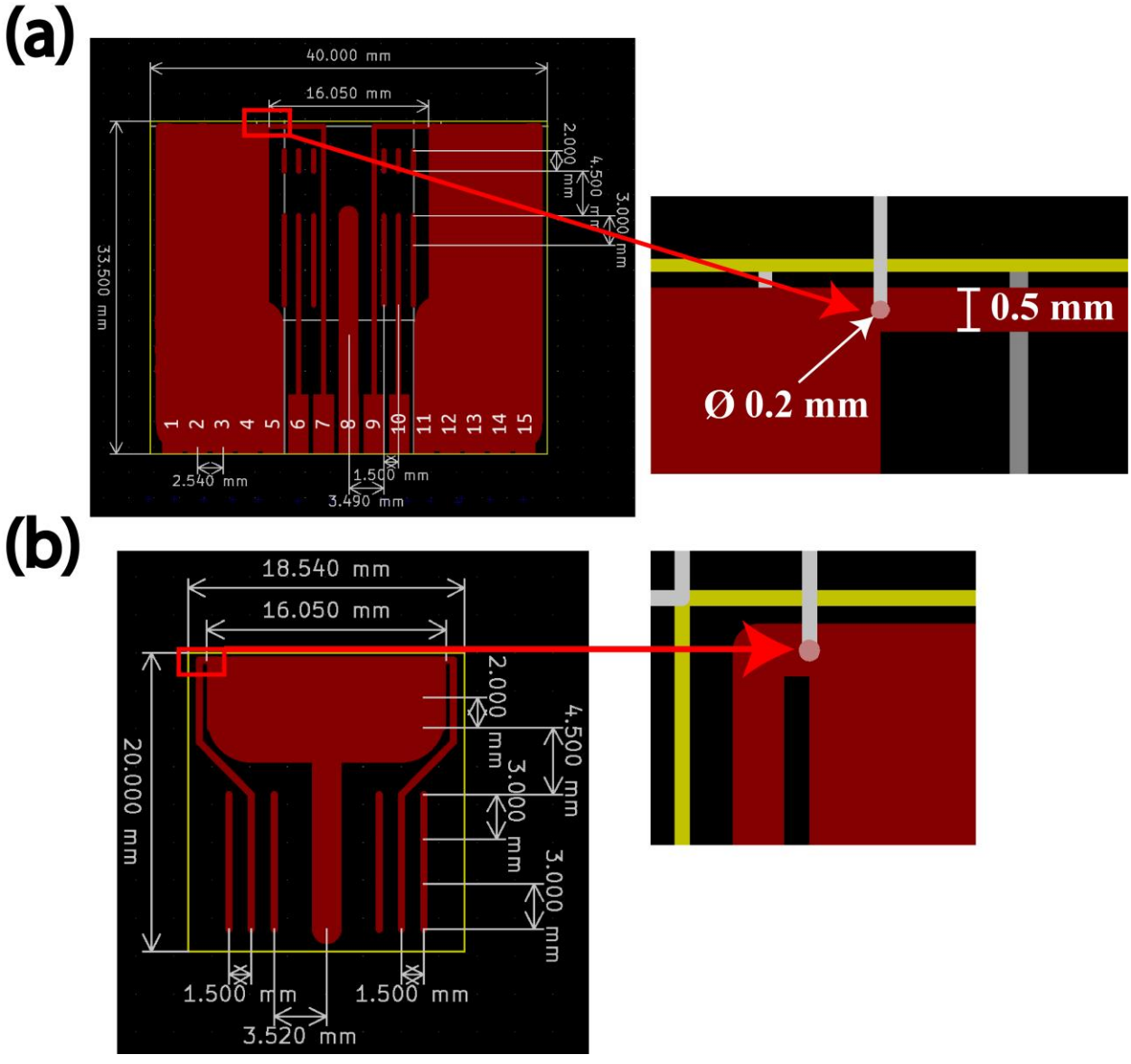

Figure 2.19: (a) Schematic of motherboard, with dimensions, showing one of current-stressed solder joints inside red rectangle (b) schematic of daughterboard and corresponding solder joint.

Chapter 3. Equipment used in EM test

The equipment used in the electromigration test is discussed in this chapter. Equipment specifications are provided, followed by the characterization of the equipment. Additional equipment and processes, which were developed to optimize the test setup, are also shown.

3.1 List of equipment and specifications

This section deals with the specifications for the equipment used for the electromigration test. The equipment consists of 7 main components: power supply, oven, high temperature cables, high temperature connectors, multiplexer, and voltmeter. Additionally, some other accessories were used such as d-sub connectors, regular ribbon cables, resistance temperature detector (RTD) sensors, a computer with python (Spyder) installed as well as a mechanical support system, as shown in Figure 3.1. These components are explained in details in Appendices A and B.

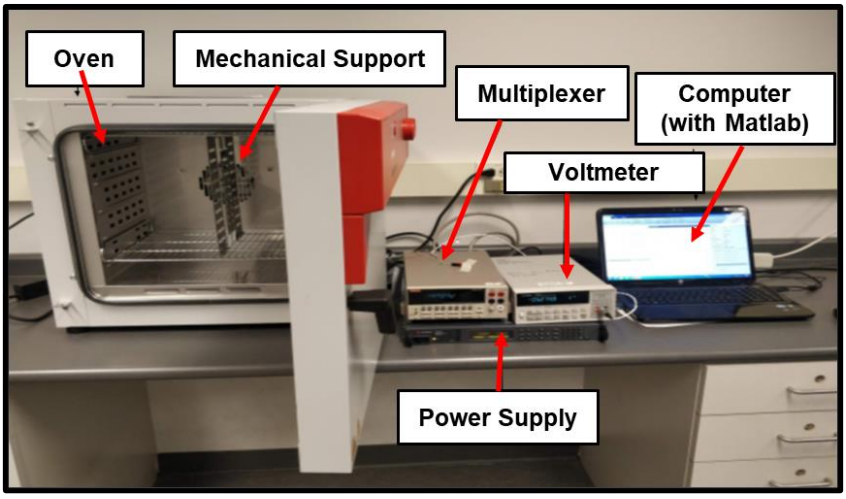

Figure 3.1: Overview of equipment for the electromigration test showing the main components: oven, mechanical support, multiplexer, voltmeter, power supply and a computer.

3.1.1 Commercial oven

To verify the accuracy of the equipment, the equipment was calibrated and characterized. The oven used for the EM experiment should maintain a constant temperature (with very little fluctuation) and allow for various temperature transitions - “Ramp” and “Step”. Additionally, the temperature deviation in the oven’s workspace must be low since the tested samples might be positioned at different locations inside the oven, and a uniform temperature distribution is vital to allow for a controlled experiment.

Due to these requirements, the FP053UL-120V Binder Oven was chosen for this application. This oven provides a large temperature range (5 to 300 °C) and a small temperature uniformity (2 K at 150 °C). The multiplexer module used for this experiment was the Keithley 7708 model, which allows for up to 40 channels to be used. In the case of this experiment, eight Pt1000 temperature sensors were used to measure the temperature distribution inside the oven at each corner, as shown in Figure 3.2.

The oven temperature variation agrees with the ±2 °C specified in the specifications sheet, as shown in Figure 3.3. However, it was determined that a 2 °C temperature change is a considerable amount since the test would be run for up to 1000 h, and a small temperature difference between samples would be amplified due to the time at which the samples are tested. Thus, a temperature sensor is needed for each PCB sample being tested.

Additionally, it was determined that placing the samples near the walls of the oven interior led to larger temperature fluctuations. This was later confirmed from the oven’s user manual.

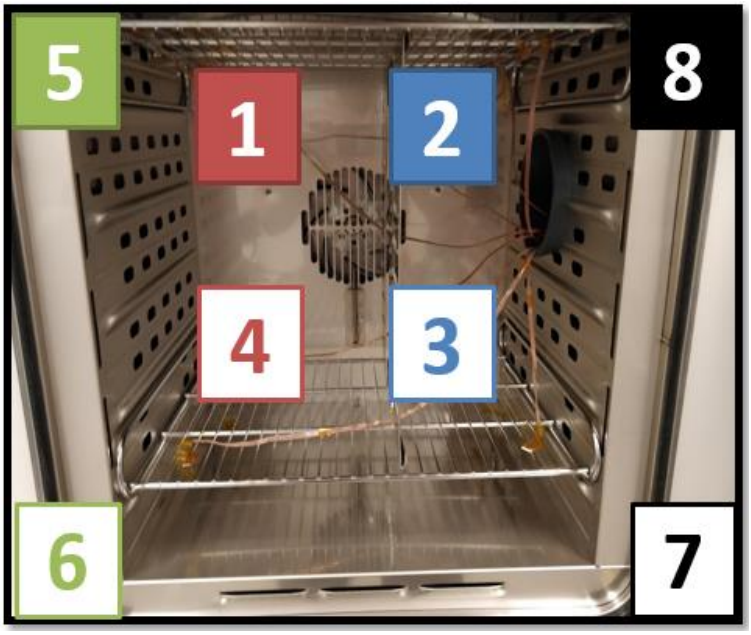

Figure 3.2: Location of 8 temperature sensors and their respective color-coding shown in Figure 3.3. The graphs on top are shown as solid lines, whereas the ones on bottom are shown as dotted lines with same color corresponding to their top counterpart.

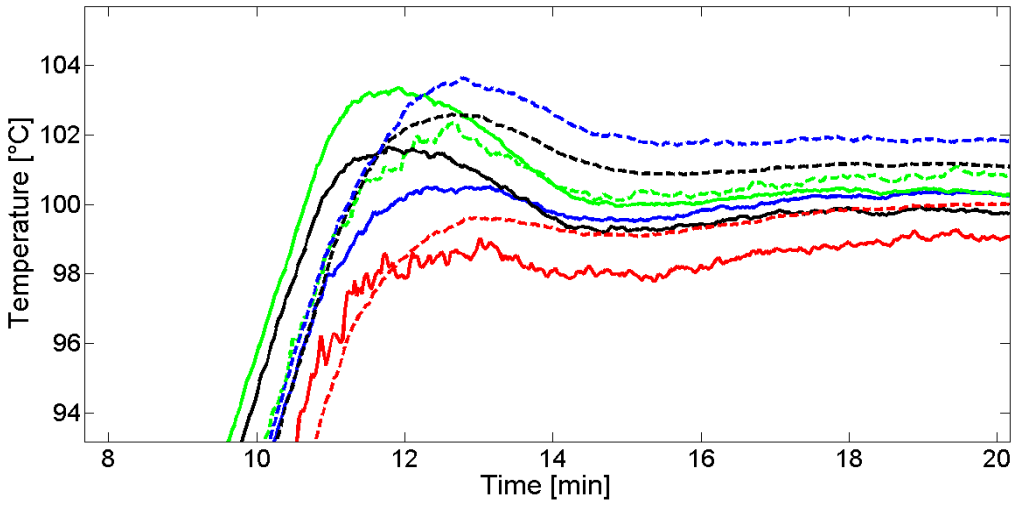

Figure 3.3: Temperature distribution curves inside the Binder Oven at 100 °C measured by eight sensors placed as indicated in Figure 3.2. The temperature range is approximately 2 °C at 100 °C, once the temperature stabilizes. Note: Accuracy of Pt1000: ± (0.15+0.002∗T)

3.1.2 Custom-made oven and PID controller

During certain applications, such as EM under a microscope, an oven cannot be used. Thus, a custom-made heating oven has to be created to increase the temperature of the test vehicle.

Two variations of the experimental setup are shown in Figures 3.4 (a) and (b). Both methods incorporate a power supply and a multiplexer, serving to measure the resistance values of the different channels. Both the temperature and power characterization experiments were performed in a single test to accelerate the thermal resistance measurement, with the purpose of characterizing the effect of Joule heating on EM.

The experimental setup for the accelerated pre-characterization testing utilizes the same equipment as that of the current stressing test, providing a robust system that allows for rapid testing and flexibility. A data acquisition system using the PyVISA Python package was developed for recording and saving the data as available in Appendix C. Additionally, the test vehicle was positioned under a microscope, with images being taken at a specific time-interval. The main difference between the two variations of the setup is the use of an upright microscope in the main method, as shown in Figure 3.4 (a), whereas an inverted microscope was used in Figure 3.4 (b). Additionally, two heating variations were provided, with the main setup using a hot plate and the alternative setup using a heating wire with an enclosure. The use of a heating wire allows for easier control of the temperature. The power delivered to the heating wire can be changed using a programmable power supply, allowing for automation during the pre-characterization tests. Figures 3.5 (a) and (b) show the physical experimental setup with its two variations.

The test vehicle was positioned under a distance of 2.27 cm from the 20 x microscope objective lens. The interval rate was set using the “IS Capture for MA Series Camera” software to capture images at 1-h intervals, with a resolution of 2592 x 1944 pixels. In hindsight, 1-h intervals were deemed too long as the final failure cannot be resolved. For example, increasing the interval rate to 1 image every 1 min, assuming each image is 200 kB and the failure time is 300 h, would require 6 GB of storage and allow capturing additional microstructural changes which could be beneficial for understanding the failure mechanism. Image processing, using GIMP software, was performed to measure the length of cracks and the area of the voids.

A test vehicle with a daisy chain configuration poses a challenge in identifying the solder joint that is most susceptible to failure. To counteract this problem, one of the solder joints was ground more than the other solder joints to ensure a smaller cross-sectional area and consequently, a larger current density to accelerate EM in that specific joint.

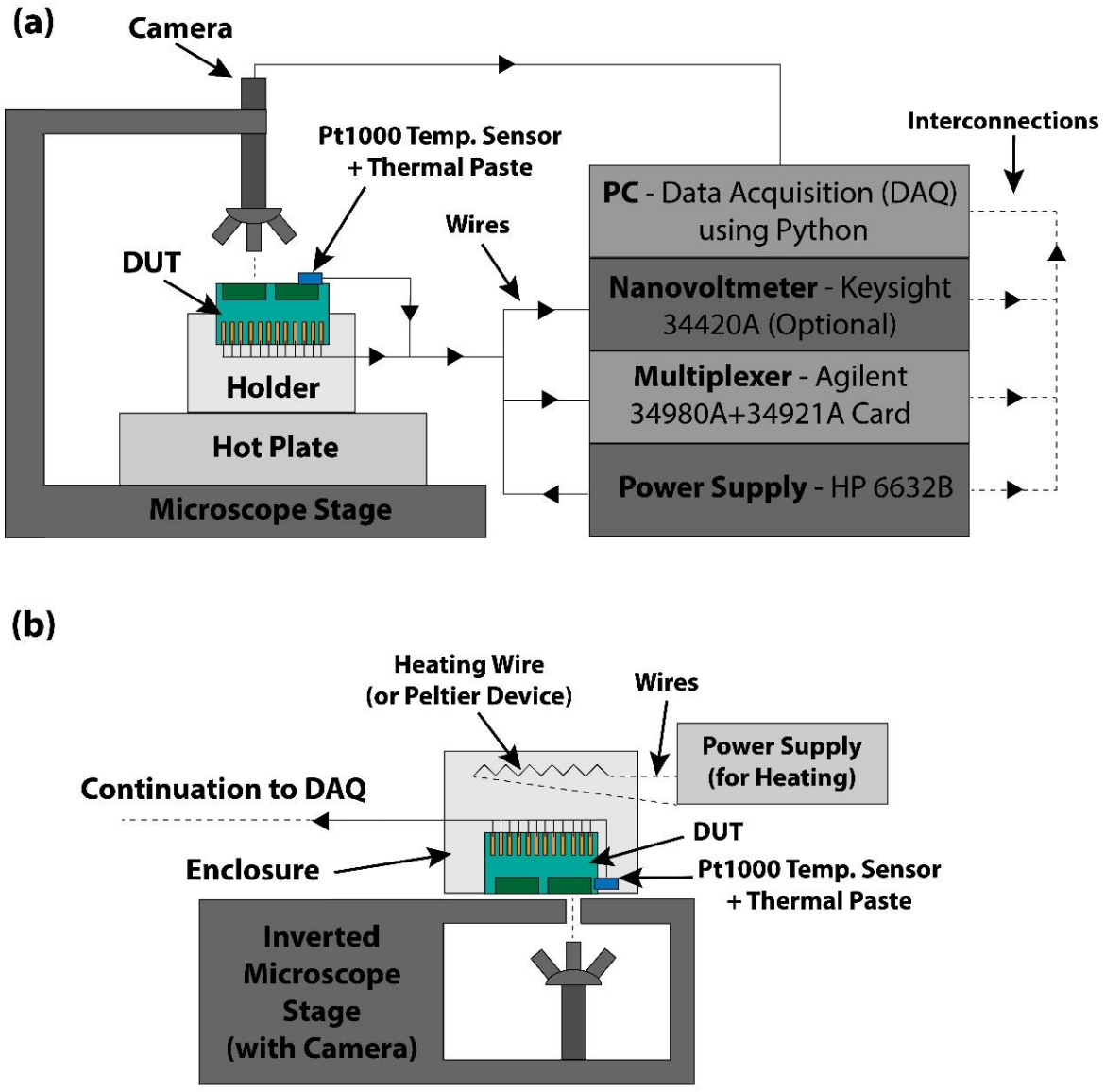

Figure 3.4: Schematic of experimental setup used in characterization and current stressing tests, showing (a) main method, and (b) alternative method using inverted microscope that allows for automated temperature control.

Alternatively, as performed in another example experiment, the microscope was modified by attaching a stepper motor to one of the microscope's X-Y translational control knobs. The stepper motor was controlled using an Arduino to automate the movement of the microscope stage to alternate between the solder joints in the daisy chain. This method allows for statistical evaluation when testing multiple samples simultaneously. Additional details of this setup and the proportional–integral–derivative (PID) controller are shown in Appendix C.

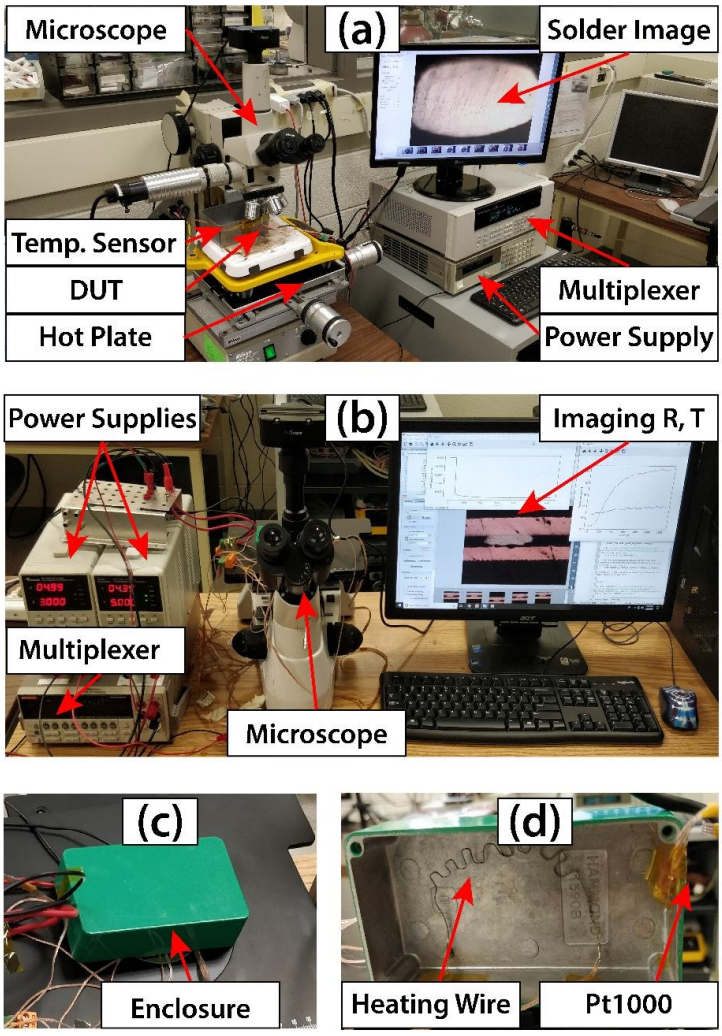

Figure 3.5: Physical experimental setup, showing (a) main method, (b) alternative method, (c) enclosure used for alternative method, and (d) heating method and temperature sensor used for alternative method.

Chapter 4. Electromigration test results

Sample-to-sample variations of the geometry and resistance at room temperature, both within the same test vehicle as well as between different test vehicles, were observed. To account for these variations, temperature and power pre-characterization tests were performed for each sample. Test vehicle 1 was used to obtain the real-time visuals in example 2, whereas test vehicle 2 was used to obtain the visuals in example 1. The pre-characterization tests were performed on both test vehicles, but only the results of test vehicle 2 are shown for simplicity.

4.1 Pre-characterization tests

The pre-characterization tests were split into the temperature and power tests, which were then combined to obtain the thermal resistance of the solder joints.

4.1.1 Temperature characterization

The temperature characterization involves the measurement of the temperature coefficient of resistance (TCR). The nominal temperature levels used were 50 °C, 100 °C and 140 °C. The resistance values of the DUTs were measured at each temperature value to obtain resistance versus temperature (R-T) graphs, enabling the calculation of the TCR. Examples of a temperature profile and corresponding resistance profile are shown in Figures 4.1 (a) and (b), respectively.

The average temperature characterization (R-T) of two solder joints is shown in Figure 4.2. A line of best fit was drawn for the R-T graph.

$$R = mT + b \tag{2}$$

where m is the slope and b is the y-intercept. The TCR at 0 °C values were calculated dividing the slope by the y-intercept, $TCR_0 = m/b$. Before cross-sectioning, the average slope of the SAC305 solder joints was $m = 1.67\times10^{-6}$ Ω/°C, and the average TCR_0 value was $TCR_0 = 4.84 \times 10^{-3}$ K^{-1}. At 20 °C, this calculates to $TCR_{20} = 1/(20+1/TCR_0) = 4.41\times10^{-3}$ K^{-1}, which is ≈10% larger than that reported in [54].

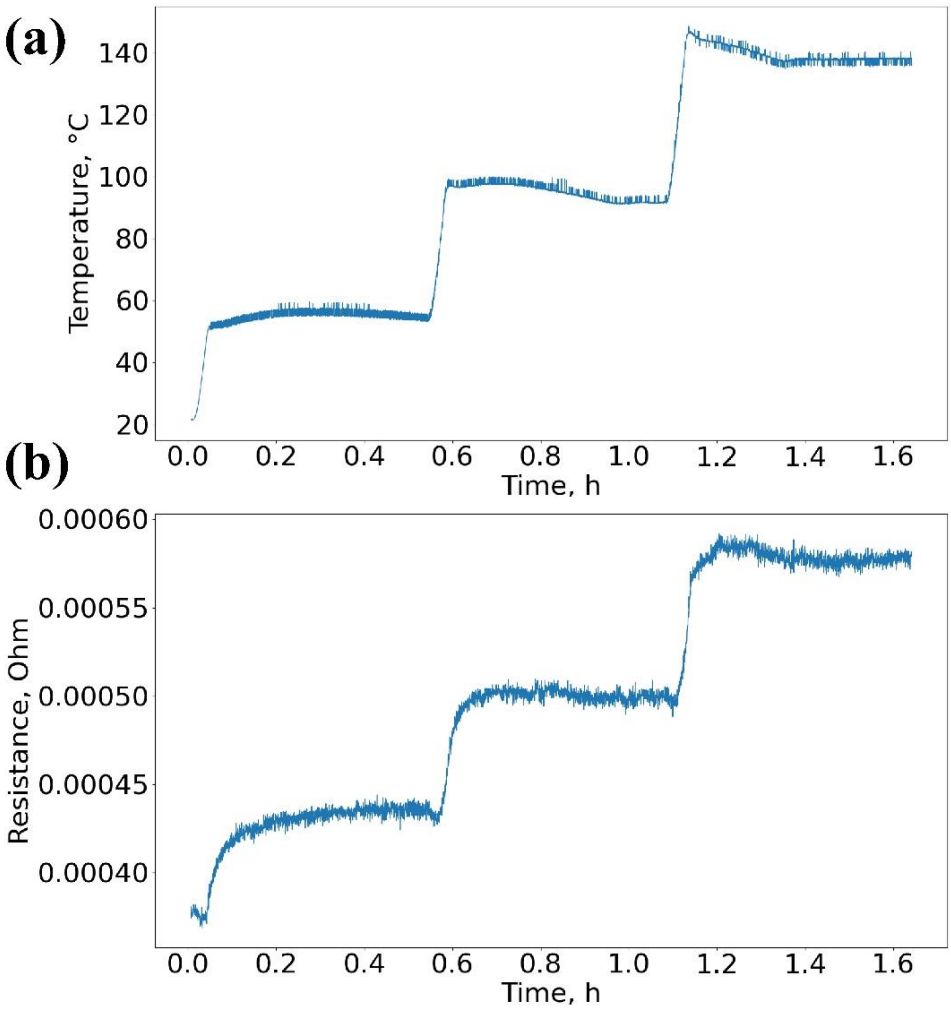

Figure 4.1: Temperature characterization test (a) heating curve of test. Three heating stages were utilized at three temperatures: 50, 100 and 140 °C. Sufficient time was elapsed between heating stages to ensure temperature stabilization of oven and ensure sample and temperature sensor reach same temperature.

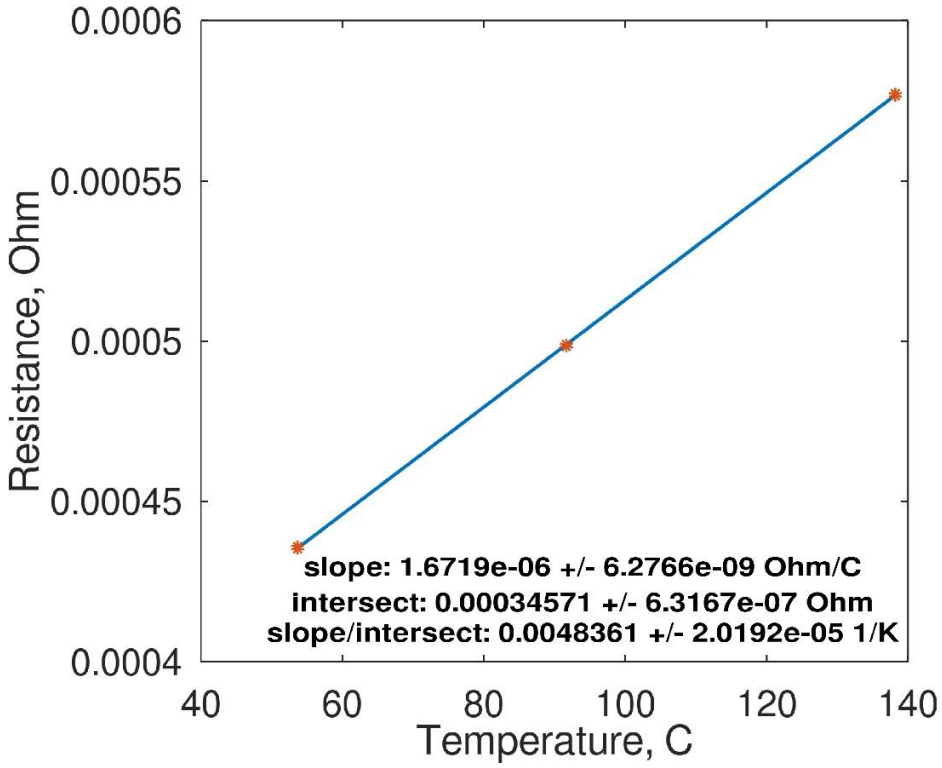

Figure 4.2: Results of temperature characterization test. Line of best fit is drawn to obtain TCR value and error estimate.

4.1.2 Power characterization

Following the temperature characterization, a power characterization test was performed. To obtain the resistance versus power (R-P) graphs, nine current levels were used. The current values started at 0.5 A until 5 A, with 0.5 A steps. Each step was held for approximately 15 s, followed by 5 s wherein current was set at 0 A to allow for the sample to cool down. The entire test data plot and the zoomed-in portion when the current was switched on is shown in Figures 4.3 (a) and (b), respectively.

To ensure that the flip configuration sample was not significantly affected by electromigration during the characterization phase, a limit equal to 50% of the EM current was set. The power and resistance values at each current level were averaged to obtain a point on the R-P graph. This procedure was repeated for all current levels. The line of best fit

$$R = rP + s \tag{3}$$

was determined using nine data points interpolated between the measured R-P data, at approximately equal power intervals, as shown in in Figure 4.4. The equidistant interpolation was done to achieve approximately equal fitting-weight for lower and higher power data. The slope was found to be r = 0.00123 Ω/W.

The results from the power characterization and the temperature characterization were combined by way of equating the right sides of equations 2 and 3,

$$T = \frac{r}{m}P + \frac{(s-b)}{m} \tag{4}$$

Thus, the thermal resistance of the SAC305 solder joint $R_{th} = r/m$ was found to be R_{th} = 736 ± 28 K/W.

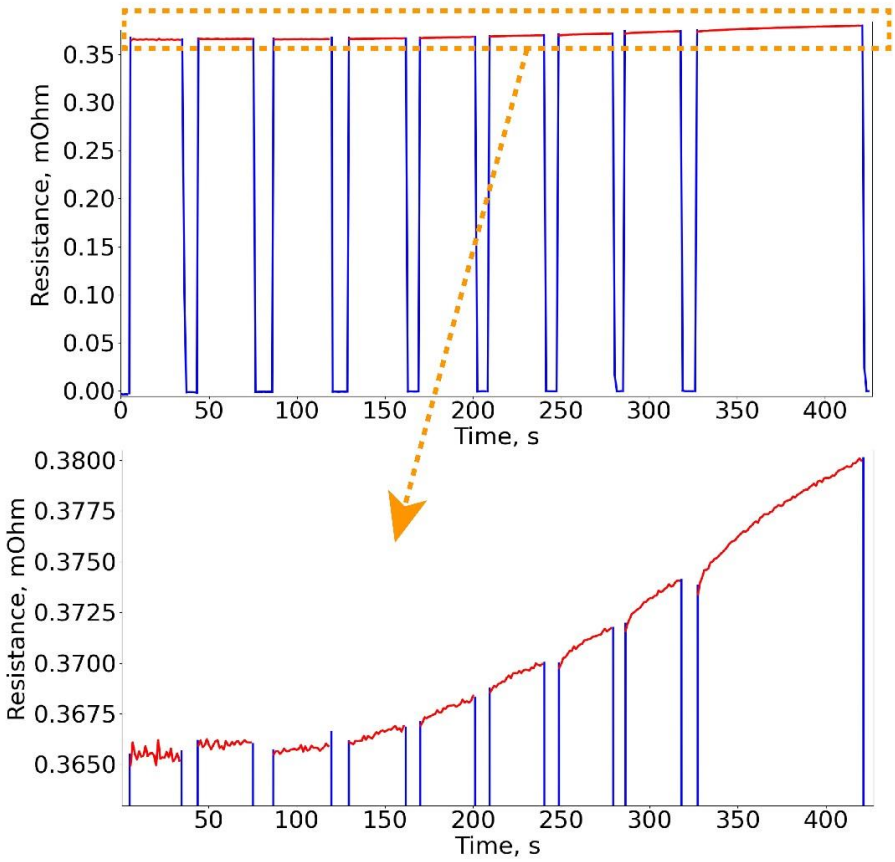

Figure 4.3: Power characterization test. Red part of curve shows when resistance measurements are recorded, and blue part shows portion when current is switched on and off. Figure shows, (a) entire test starting at 0.5 A until 5 A, with 0.5 A intervals (b) zoom in on the portion at which current was switched on. The resistance increased with higher current as a result of Joule heating.

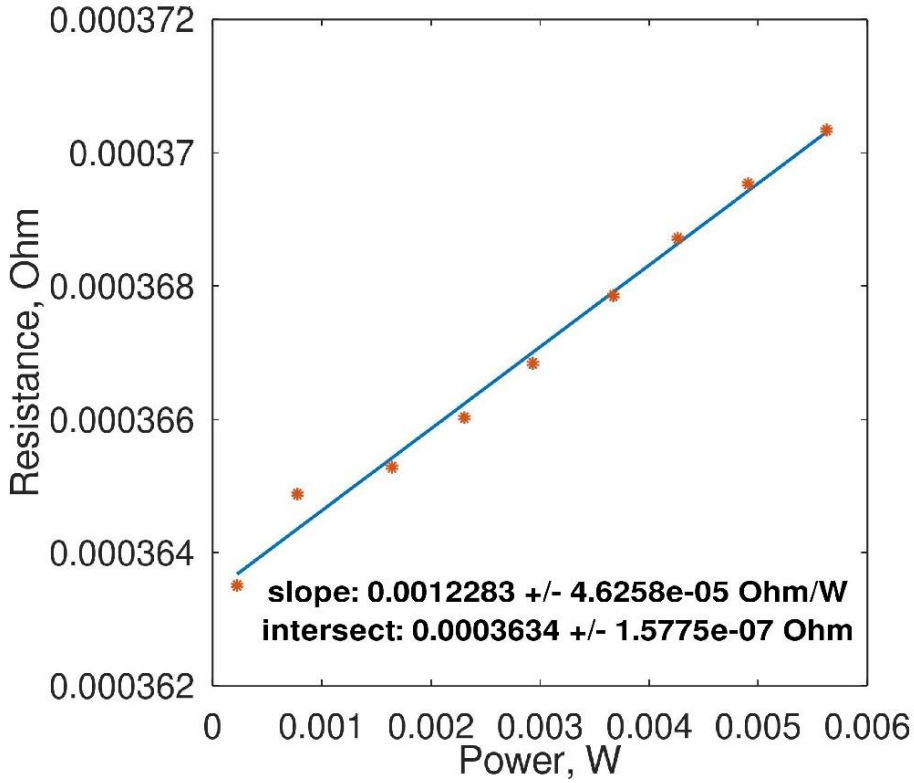

Figure 4.4: Results of power characterization test. Line of best fit is drawn for solder joint.

4.2 EM test at room temperature

An EM test was performed on test vehicle 1 using 5 A of current. However, the test was performed at room temperature without external heating to limit contribution from thermomigration and purely obtain failure from electromigration. The thermal resistance values for all the solder joints are shown in Figure 4.6, which were calculated using the pre-characterization tests shown in Section 4.1. With a nominal solder joint diameter of 250 μm, the theoretical current density was calculated to be 1.02×10^4 A/cm^2. Figure 4.5 (a) shows the resistance increase during the test, accompanied by the corresponding estimated temperature and temperature sensor readings, shown in Figures 4.5 (b) and (c).

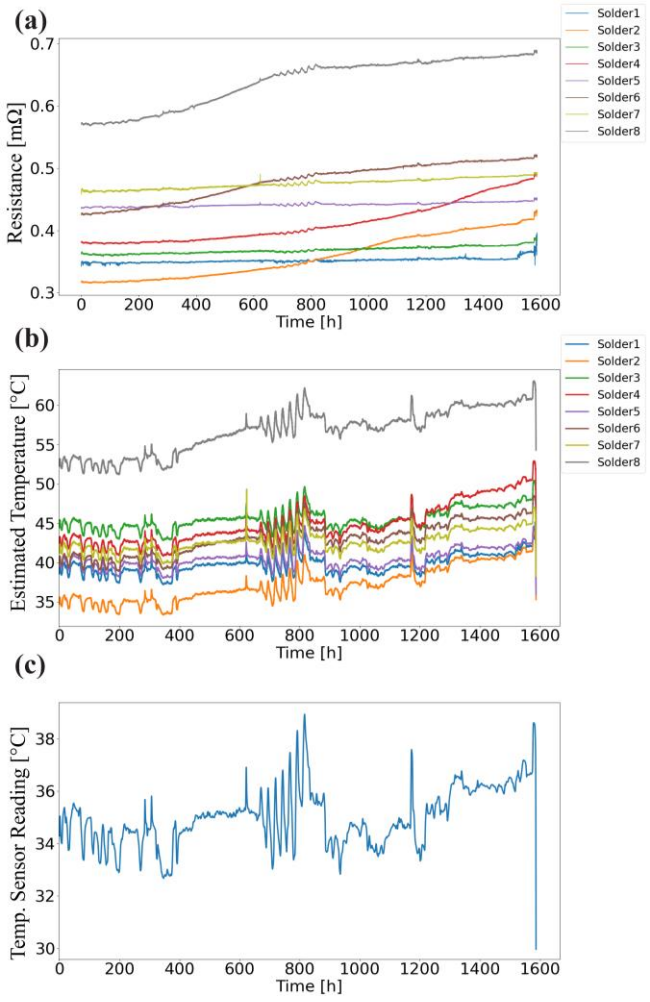

Figure 4.5: (a) Resistance of solder joints during room temperature current stressing test (b) temperature of individual solder joints calculated using thermal resistance (c) test vehicle temperature measured by Pt1000 temperature sensor.

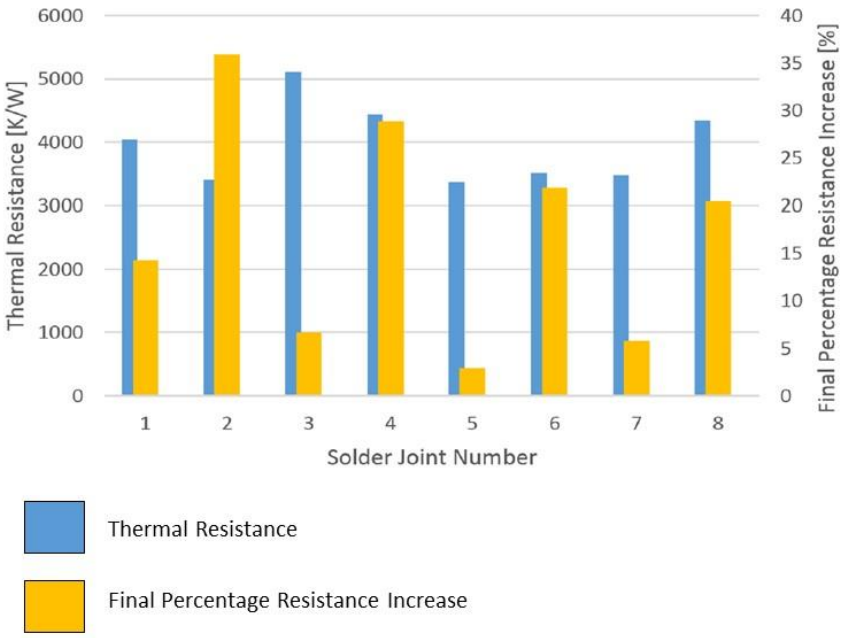

Figure 4.6: Thermal resistance values are shown on left in blue and final resistance increase at end of test is shown on right in yellow.

Some noise was present during the test due to room temperature fluctuations. To reduce the noise, a constant temperature chamber would be recommended. The test vehicle failed after 1600 h of current stressing. A significant amount of Joule heating was recorded by the temperature sensor near the test vehicle. The recorded temperature was approximately 35 °C, compared to the room temperature of 22 °C. The estimated temperature using the thermal resistance method demonstrated a significant temperature difference between the solder joints, the largest being 20 °C, between solder joints 2 and 8. This demonstrates that each solder joint produced a different amount of Joule heating, supporting the significance of this method to estimate the heating from each joint separately.

4.3 Real-time visuals (RTV)

The results from the room temperature experiment lasted approximately 96 days. In order to accelerate the test, cross-sectioning was performed which was also used to obtain real-time visuals.

4.3.1 RTV example 1: textbook scenario

This section was taken, with minor modifications, from [55]. An example of a cross-sectioned solder joint between mother and daughter boards is shown in Figure 4.7 (a). Prior to EM testing, the R-T and R-P tests were repeated to obtain a thermal resistance of 559.1 K/W. The testing conditions are shown in Table 4.1. The error of R_{th} for the cross-sectioned sample was assumed equal to that obtained from the more numerous unharmed solder joints (i.e. before cross-sectioning), err(*Rth*)= 28 K/W.

The smallest diameter was along the middle of the joint, having a value of 333.4 μm, giving a theoretical current density of 2.29×10^4 A/cm^2, assuming that the solder joint was cut exactly in the middle.

The EM test was starting by applying I = 10 A and heating the solder joint inside the enclosure to $T_{\text{ambient}} \approx 60$ °C as measured by a temperature sensor which was read out during the EM tests. The thermal resistance was used to estimate the temperature of the solder joint, T_S, during current stressing, using

$$T_s = T_{ambient} + P \cdot R_{th} \tag{5}$$

where $P = R \cdot I^2$ is the electrical power delivered to the solder joint. It is assumed that energy from this is completely transformed into thermal energy (Joule heat). For this we assume the energy consumed by electromigration and thermomigration is negligible compared to the Joule heat.

Results obtained during the EM test for the solder joint resistance R and extrapolated temperature T_s are shown in Figure 4.8. We expect eq. (5) to hold in first approximation even if the solder joint forms voids and cracks during electromigration, increasing its resistance permanently. This is supported by the facts that (a) the P in eq. (4) consumes the electrical power

delivered to the joint accounting for the rise in R, and (b) R_{th} does not depend much at all on the joint resistance but mainly on the thermal paths leading away from the joint. These paths are unaffected by voids or cracks growing in the solder joint itself.

Having discussed the practicality of deriving T_S using eq. (5), it remains to estimate the error of T_S which depends on the R_{th} error:

$$err(T_s) = P \cdot err(R_{th}) \tag{6}$$

This error is indicated by the dashed datalines in Figure 4.8 and ranges from 1.6 K (start of EM) to 2.3 K (end of EM).

Table 4.1: Real-time viewing test factors and responses (RT=Room Temperature)

$R_{initial}$ at RT (mΩ)	$R_{initial}$ cross-section at RT (mΩ)	R at start of EM test (mΩ)	Time until 20% R increase (h)	I (A)	R_{th} (K/W)
0.314	0.399	0.56	66	10	559.1

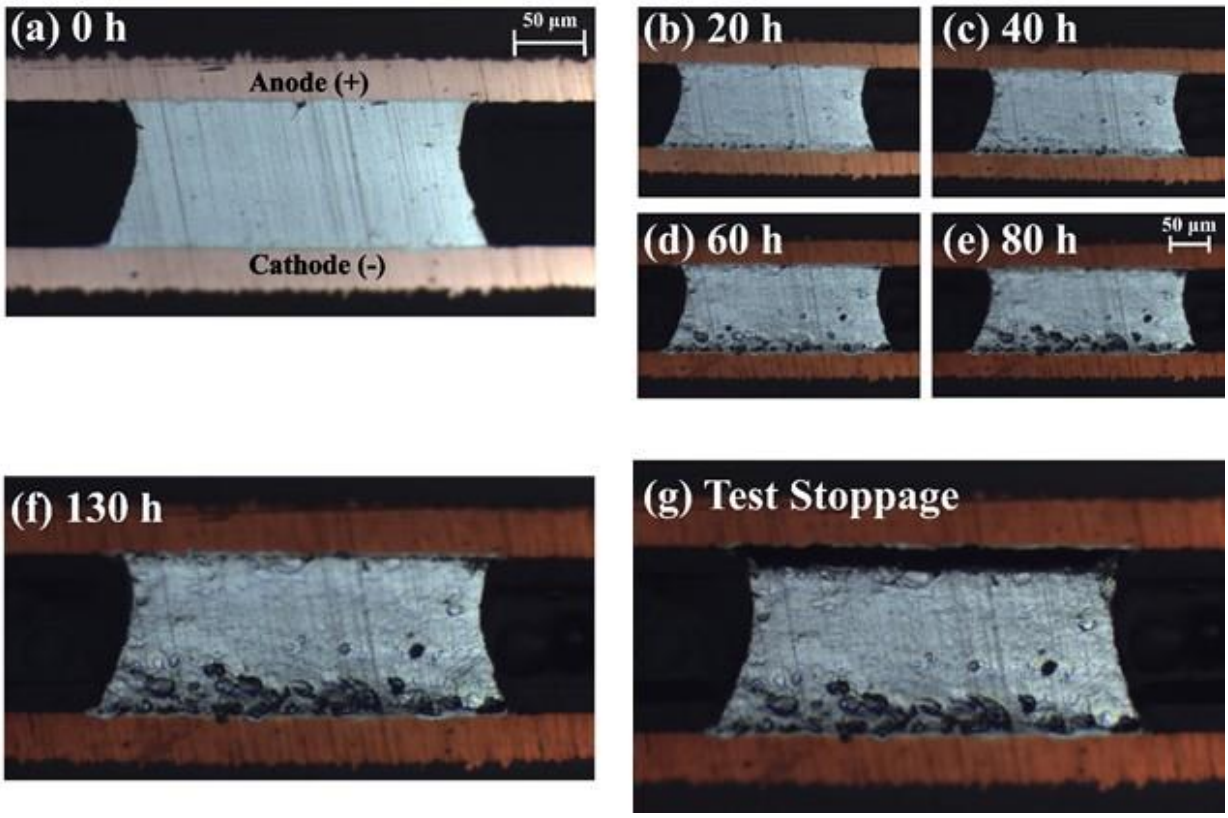

Figure 4.7: Evolution of electromigration failure in a single solder joint under I = 10 A and $T_{ambient} \approx 60$ °C, showing void nucleation at cathode and nucleation of smaller voids on anode. Current direction was from top metallization line (anode) to bottom (cathode). The current was switched off in (g) and the temperature was back at room temperature, down from a peak temperature of 107 °C, resulting in a complete separation crack along the anode interface.

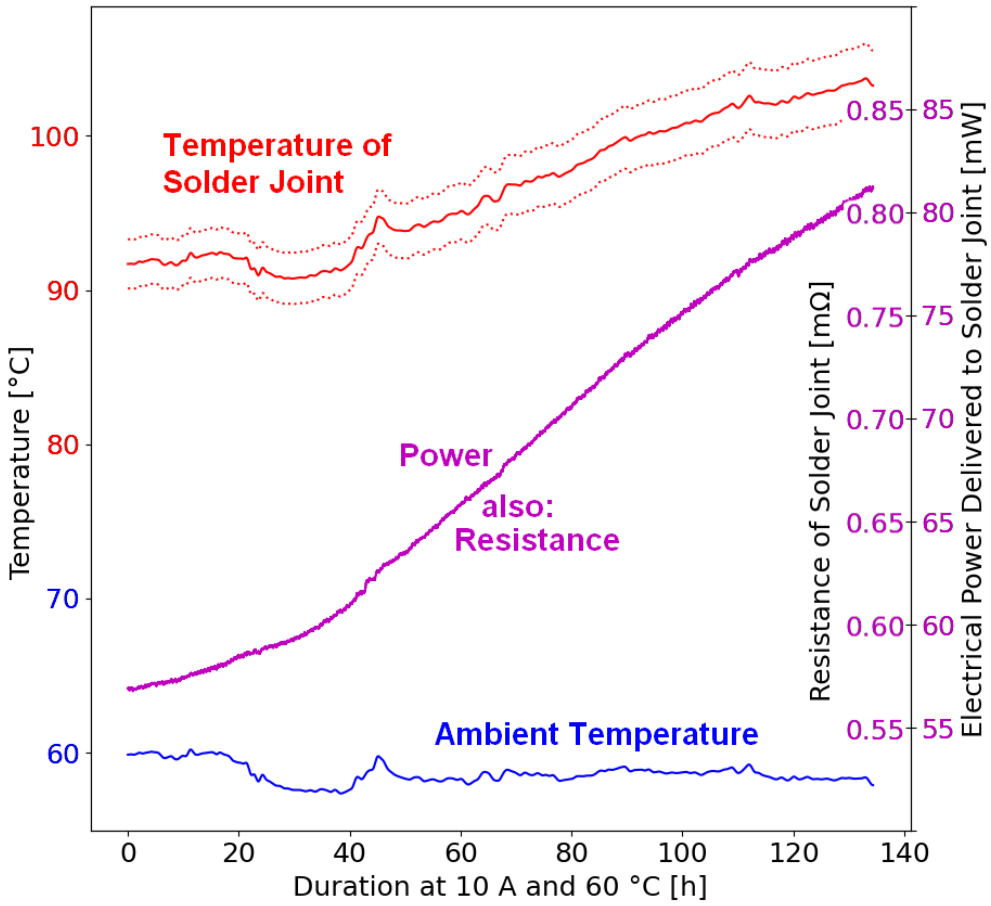

Figure 4.8: Results from electromigration test with stressing current I = 10 A and nominal ambient temperature $T_{ambient}$ = 60 °C up to 40 % resistance increase. Variations are due to room temperature variations. $R = V/I$ and $P = V \cdot I$, where V is voltage evolution measured across solder joint.

Figures 4.7 (a) – (f) show the microstructural changes occurring from EM, with corresponding times. Significant void growth occurred at the cathode, verifying failure due to EM. Furthermore, cracks propagated along the anode interface between the metallization line and solder joint. The test was stopped prior to an open circuit, since our arbitrary 40% resistance increase criterion was met. Immediately after current stressing and external heating were stopped, the crack at the anode grew along the solder-metallization line interface, causing a complete loss of connection, as shown in Figure 4.7 (d). The thermal shock from the material cooldown resulted in fracture of the already weak solder joint, ultimately causing the crack propagation and solder joint separation.

The cracking overserved during cooling after EM raises the question of the real point of complete failure for the DUT under current stressing. Conventional EM testing may always go beyond the point in time when the DUT stops being able to survive a cool-down to room temperature. The opportunity exists to develop more advanced EM testing methodologies as well as more reliable definitions and experimental data for time-to-failure.

The results highlight the impact of Joule heating on the increase of solder joint temperature and the importance of ambient temperature selection, adding to Joule heating, to accelerate electromigration experiments.

Furthermore, if R_{th} is determined for each individual solder joint, the sample-to-sample variations could be reduced by selecting appropriate ambient temperatures to achieve the same overall solder temperature. Thus, the differences in thermal resistance could be balanced out by the ambient temperature selection. This would help to control the temperature variable more precisely for each sample, resulting in more precise EM test results.

The current crowding location in this example agreed with the location observed in the literature in which the voids nucleated at the cathode interface between the metallization line and solder joint [52]. This failure mechanism was referred to as “discrete void growth and coalescence” in [24] in which smaller voids grew separately that later coalesced to form larger voids that negatively impacted the electrical resistance and mechanical integrity of the joint. Furthermore, the failure occuring due to the temperature cooldown at the end of the test is supported by [56], in which the authors observed that temperature fluctuations due to Joule heating and environmental conditions introduced fatigue in the solder joints, ultimately causing failure.

4.3.2 RTV example 2: current redistribution

This section was taken, with minor modifications, from [49]. For this test, a sample from test vehicle 1 was used. The experimental setup is shown in Figure 3.4 (a). A data acquisition system using the PyVISA Python package was developed for recording and saving the data as available in Appendix C.

The temperature was set at 50 °C using a custom-made oven shown in Figure 3.4 (b). The power supply was set to deliver a constant value of 5 A. A multiplexer was used to measure the resistance of the samples as well as that of the Pt1000 sensor, which were later converted to their corresponding temperature values using the formula

$$R_T = R_0(1 + A \cdot T + B \cdot T^2) \tag{7}$$

which was re-arranged to solve for the temperature

$$T = \frac{-R_0 \cdot A + \sqrt{R_0^2 \cdot A^2 - 4 \cdot R_0 \cdot B \cdot (R_0 - R_T)}}{2 \cdot R_0 \cdot B} \tag{8}$$

where *A*, *B* and R_0 are constants, with values of 3.9083×10^{-3}, -5.775×10^{-7} and 1000, respectively. R_T is the resistance at the temperature *T*.

The 4-wire method was employed to allow for the detection of small resistance changes. The solder sample was cut in half during the grinding process, giving a theoretical current density of

$$J = \frac{I}{A} = \frac{5\ \text{A}}{0.5\ \pi r^2} = 1.37 \times 10^4\ \text{A/cm}^2 \tag{9}$$

where *J* is the current density, *I* is the current, *A* is the cross-sectional area and *r* is radius of the cross-sectioned solder joint. In our case, the values for the variables *I* and *r* were 5 A and 152.4 µm, respectively. This current density was determined by using the method outlined in standard JEP154 [11]. The test was run for 330 h to when an open circuit occurred.

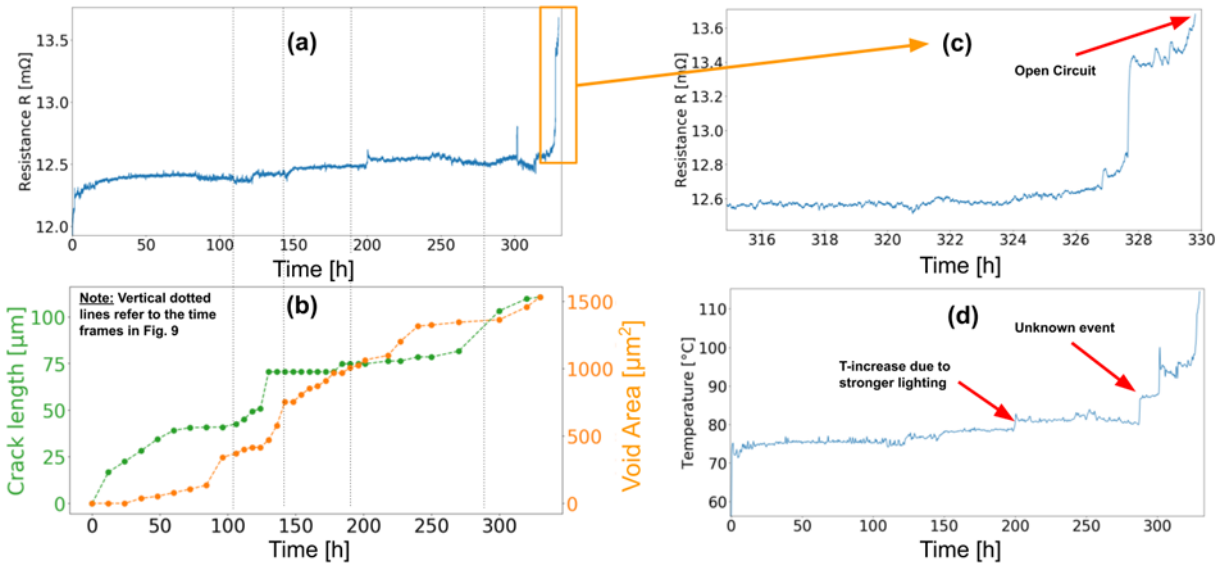

Figure 4.9: (a) Resistance measurements showing resistance changes during test. Micrographs are shown in Figure 4.10 at the times indicated by dashed lines. (b) Growth of cracks & voids (c) Resistance measurements at the end of test immediately prior to failure. (d) Temperature fluctuations during test.

An example of the microstructural evolution of the solder joint is presented, demonstrating the capability of the proposed method for enhanced electromigration monitoring.

Figures 4.9 (a) and (c) show the entire data and zoomed-in data of the experimental solder resistance data. The temperature of the hot plate was assumed to be constant at 50 °C, which was different from that of the measured temperature due to Joule heating, as shown in Figure 4.9 (d). The test was interrupted around the 200-h mark to modify the microscope light source, explaining the increase in temperature.

As shown in Figure 4.9 (a), the values of the resistance were relatively flat. A more detailed analysis shows the resistance increased approximately 0.5% in the first three days and then decreased with a more or less constant rate by approximately 2% in the following 9 days. However, towards the end of the test, there was a sharp peak occurring in the last hour of the test, wherein the resistance value increased to 13.63 mΩ. The resistance increase was attributed to defects introduced by electromigration. This claim is supported in the next section by a close examination of the microstructural changes which agree with the electromigration failures in the literature.

Figure 4.9 (b) shows measurements of the crack and void growth during the test. Both the crack and the void followed a similar pattern, with significant (sometimes abrupt) length and area increases, respectively, at certain time-intervals. Thus, the growth rate was non-linear, peaking at different times. One of the growth phases coincided for the crack and the void between the 130-h mark and the 150-h mark. Interestingly, no strong change was observed for the resistance signal during this phase. The strong growth in this phase was followed by relatively slow growth for 100 h, with stronger growth again during the last 50 h of the test.

Figures 4.10 (a) – (e) show micrographs chosen from five selected times during the evolution of the solder sample under current stressing for 330 h. Some scratches were present after the sample preparation procedure which were present prior to starting the test. A few notable observations during the test were recognized:

1) Void formation at the top of the solder joint, with the fastest growth rate around the 150 h, indicated by the steepest slope in Figure 4.9 (b).
2) Crack propagation, with the most prominent around the top void, growing to a length of 100 μm towards the end of the test.
3) Void formation at the bottom surface of the solder joint. The voids started growing at the bottom-left interface and propagated horizontally to the right.

A few voids were present prior to current stressing, which were possibly due to the outgassing flux that got trapped in the solder during reflow, similar to what was reported in [57,58]. As a crack propagates due to electromigration, it can be expected that the current crowding location shifts from the solder joint corner to the region next to crack edges. Electrons are forced to flow around the crack, leaving the edges of the cracks with a larger current density, creating a new current crowding location. Such a location is expected to have caused void nucleation, which ultimately resulted in the void growing to the cross-sectional surface. A decrease in joint strength as a result of crack formation has been reported in the literature [59].

The relationship between voids and cracks has been reported in the literature. Wang et al. presented a theory about cracks forming at void sides [60]. Liang et al. stated the “current redistribution is the main reason accounting for void formation and propagation” [61]. Synkiewicz et. al. presented a similar theory, stating that void formation can lead to deformations in a solder joint structure which can alter current flow and temperature distribution [62].

Our observations align with the previously presented theories. Examining the sequence of events occurring inside the solder matrix, crack formation and growth preceded void formation. Thus, the pre-existing internal stresses in the solder matrix, combined with the momentum transfer of the moving electrons to the metal ions inside the solder matrix, were likely to have prompted the void formation. Therefore, it is possible the crack was the probable influence of void formation that ultimately led to failure.

In addition to the particular location of void formation, which did not occur at the corners, the void formed on the anode side. The electrons moved from the cathode (bottom) to the anode (top). Conventionally, void formation is observed on the cathode end [31]. However, in previous publications, voids have been observed also at the anode end. Liu et al. observed a void in the anode end of a Cu/Sn/Cu flip-chip joint which the authors attributed to vacancy backflow due to the backstress on the anode Cu trace lines [63]. Stahlmecke et. al. observed void formation at the anode end of silver nanowires. The cause remained unclear, but the authors theorized contamination could have played a role [64]. Yu et al. studied the location of void nucleation [65]. The authors categorized the void location and size based on four types, one of which, albeit an anomaly, occurred at the anode, similar to our results. Synkiewicz et al. supported this claim, concluding that there was a tendency for voids to form in different arrangements and locations [62].”

Due to the cross-sectioning induced shape modification and increased current density of the solder joint, higher failure rates are expected as a result of current crowding, Joule heating, and heat flux concentration (thermomigration) effects. The exact influence of these factors on the cross-sectioned failure rates remains unclear; however, it is unlikely that Joule heating alone could have impacted the results, as thermal aging in a control experiment did not result in failures, even when considering the rise in local temperature of the solder joint due to Joule heating. However, it is likely that Joule heating, combined with current crowding, resulted in an uneven temperature distribution inside the solder joint giving rise to something like a hot region or a hot spot. Assuming the existence of a hot spot, the heat would travel away from the hot spot in all directions. Any thermomigration-type diffusion would be in these same directions.

One probable explanation for the void formation at the anode side, that was previously mentioned, was the shift in current crowding location due to crack formation. The appearance of

the void immediately followed that of the crack. Both phenomena also occurred at the exact same location, which supports the probable connection between the two. Another probable explanation is the existence of a strong thermal gradient effect, typical of thermomigration, which forced atoms to travel from the anode to the cathode, opposing electromigration. When thermomigration forces are present due to large thermal gradients, it is shown that crack and void formation is accelerated [19]. Additionally, in many cases involving solder joints, EM is complemented with thermomigration, although the exact contribution of each migration phenomenon is unknown [2]. A combination of both theories is thus the most probable explanation for the appearance of the void at the anode, away from the solder joint corner.

The results from this section can be set as the upper limit for failure criteria in our test vehicles. Additionally, under these accelerated conditions, the study of various variables on MTTF can still be performed as a means of comparing the effect of these variables on the MTTF, if the diffusion mechanism is assumed the same. At temperature values below the solder melting point, surface and grain diffusion are the predominant diffusion processes. The diffusion processes depend on the activation energy which is influenced by the solder material [10,12]. As the temperature increases and approaches the melting point, the predominant diffusion mechanism becomes the lattice diffusion [10].

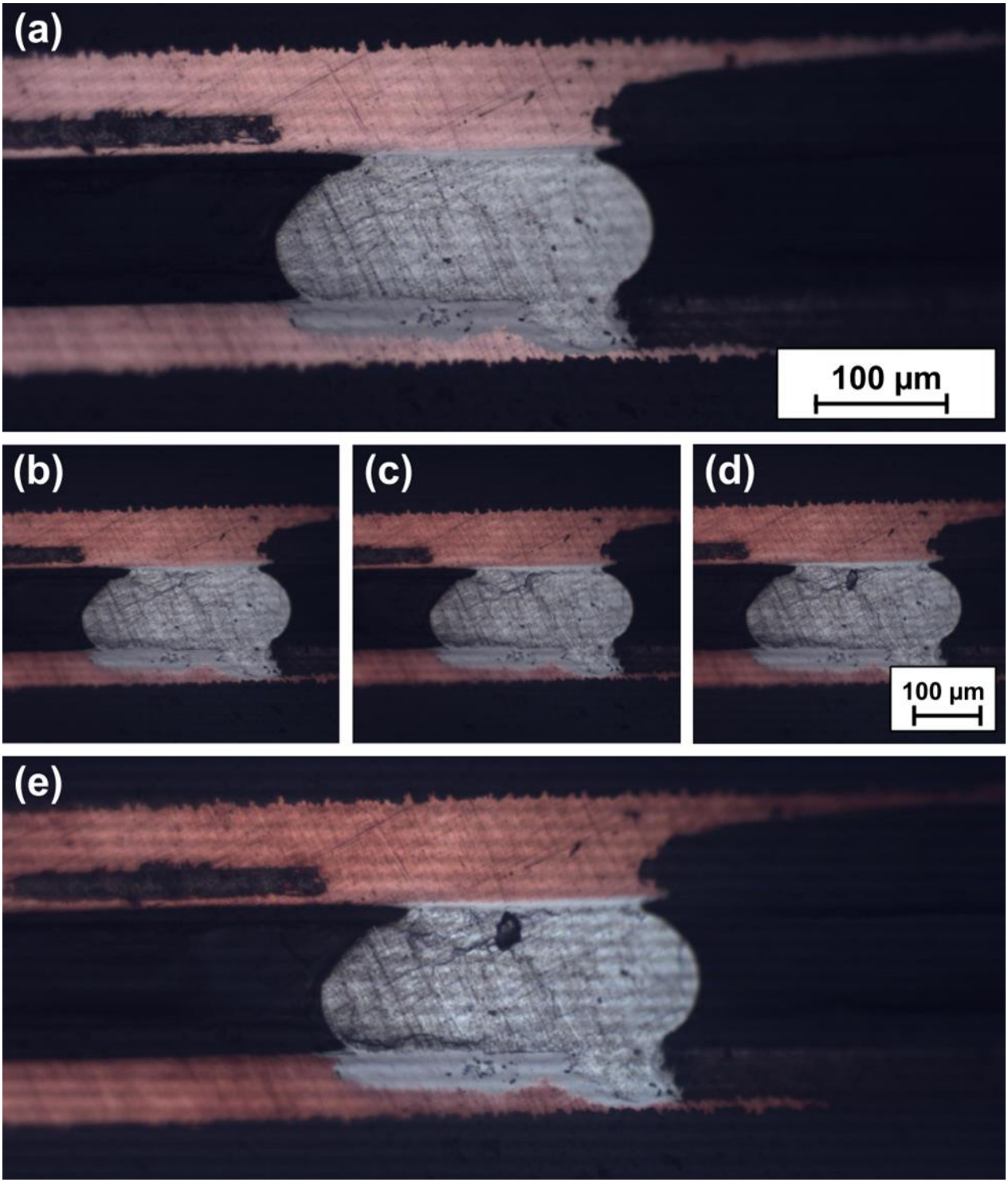

Figure 4.10: Screenshots of real-time video at (a) 0 h, (b) 102 h, (c) 139 h, (d) 171 h and (e) 276 h, respectively. Images were taken every hour. The electrons flowed from bottom-left to top-right corner.

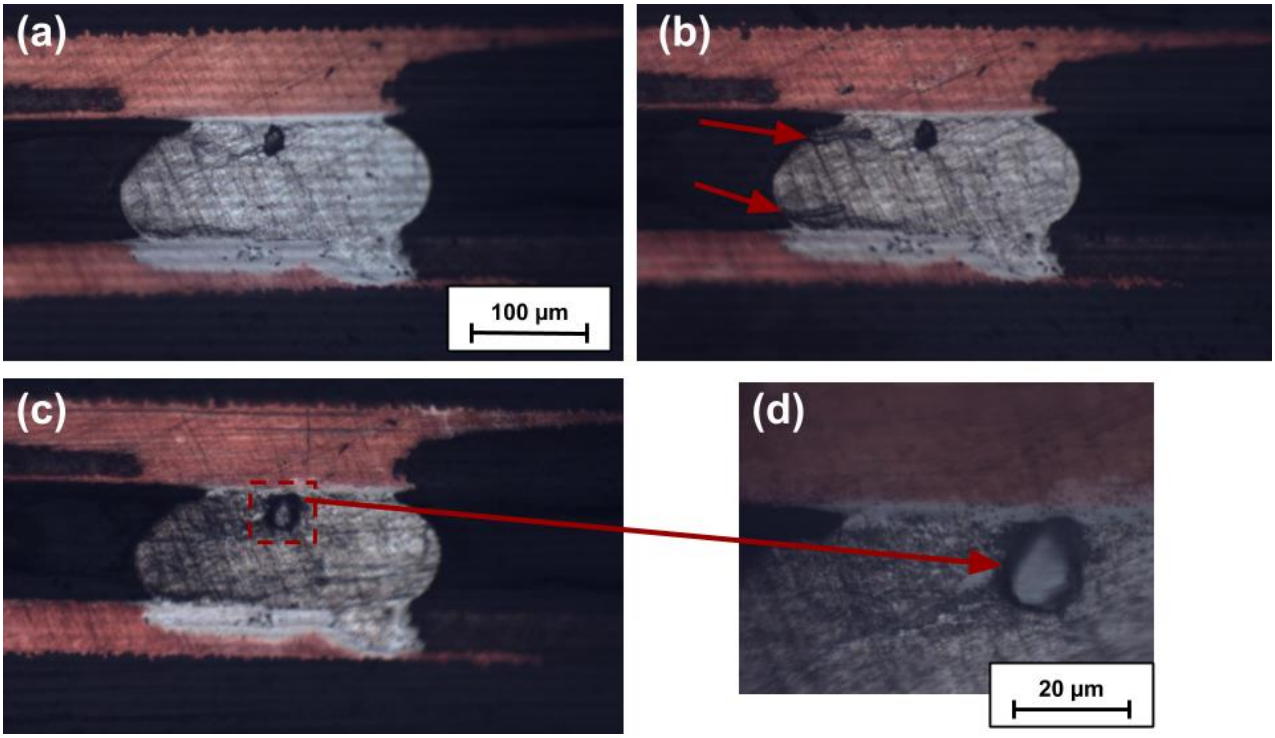

Figure 4.11: Microstructural changes after the test was stopped. (a) Image taken prior to test stoppage. (b) Image after 30 min of switching off power supply and hot plate, showing formation of two cracks. (c) Image after a few hours of test stoppage. The location of void formation was covered by a hillock. (d) Close-up image of hillock formation.

More observations were noted once the test was stopped. Crack formation, as shown in Figure 4.11, occurred in the test vehicle after 30 min of switching off the test setup. Since both the power supply and the hot plate were switched off, it was induced that these cracks were therefore a result of cooling. A hillock formed in place of the top void. Chemical diffusion, due to the difference in concentration gradients, could have played a role in the formation of this hillock. The atoms were able to rearrange based on the concentration gradients once the current and temperature gradients were eliminated.

Figure 4.12 shows further examples of changes occurring due to current stressing in solder joints, demonstrating this method in capturing those changes. If solder joints are cross-sectioned after EM testing, damage to the solder joints due to grinding and polishing is more likely to occur since current stressing results in weaker solder joints. Additionally, epoxy is more likely to infiltrate through the cracks.

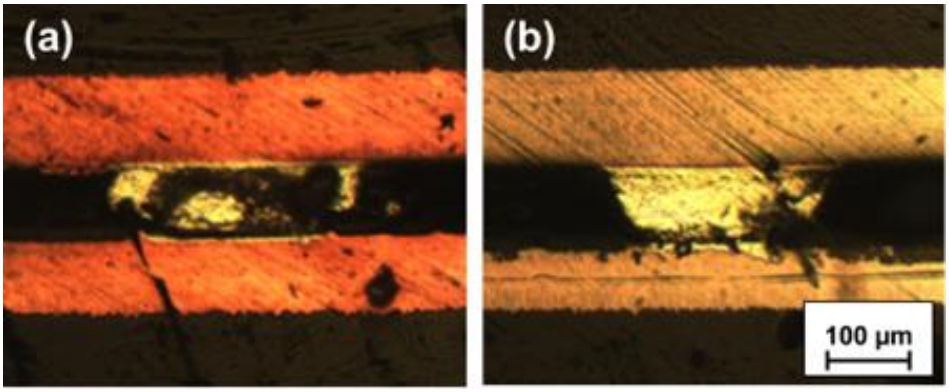

Figure 4.12: Another example of a current stressing test showing void and crack formation in two separate solder joints.

In order to verify that any changes were solely a result of EM, a control experiment without current stressing from a power supply was constructed. The experiment was performed for 300 h over a hot plate at a temperature of 80 °C, which was chosen to match the actual EM test temperature considering Joule heating. No changes were observed in the sample, as shown in Figure 4.13. Thus, this control experiment supports that temperature alone could not have resulted in the void formation shown in Figure 4.11, and EM played a significant role. Furthermore, resistance measurements did not show any permanent resistance increase, confirming that current stressing was the direct cause of the void.

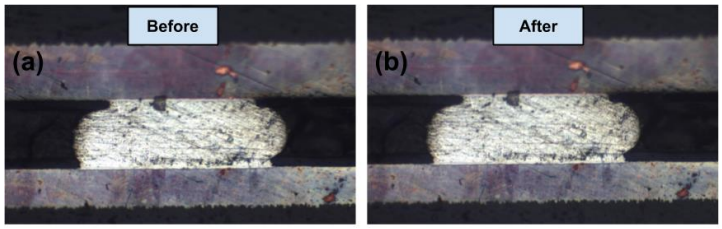

Figure 4.13: Control setup of solder joint under 80°C and no current stressing. Figure shows test vehicle (a) before test start and (b) after test stoppage. No visible change was observed.

4.4 Comparison of test vehicles

Both test vehicles were successful in observing EM failure in solder joints. Test vehicle 1 had 8 solder joints, enabling more data set collection of EM failure tests, as opposed to test vehicle 2 which only had 2 solder joints. However, the design came at the expense of Joule heating, in which the solder joints of test vehicle 1 had a more prominent effect on each other, in terms of heat generation. This finding demonstrated the importance of isolating the solder joints, by increasing the distance between them, to avoid the impact of external factors on the results of EM tests.

Additionally, it was more challenging to predict the location of failure in test vehicle 1, so the resistance of all 8 solder joints had to be measured in real-time. Similarly, it was more challenging to reflow and cross-section test vehicle 1, since any problems in a single solder joint would render the entire test vehicle obsolete as a result of the daisy chain configuration. The increased width of the current lines in test vehicle 2 allowed for higher current densities, which accelerated failure. Nevertheless, the shape and initial resistance of the solder joints in test vehicle 1 were more repeatable than those of test vehicle 2. These problems were attributed to the PCB fabrication and assembly processes, rather than the design.

In the future, it is recommended that fewer joints are used, similar to test vehicle 2, to separate the effects of Joule heating and to ease the assembly process. Smaller solder joints, as small as 50 μm, are presently available in the market[4], which can be used to further accelerate EM studies. Additionally, wider current lines are also preferred to increase the maximum allowable current flowing in the test vehicle. However, the assembly process of test vehicle 1 is recommended for future designs. Manual solder ball bumping and automated assembly using a Tresky die bonder yielded reliable and repeatable results.

[4] https://www.easyspheres.com/sn96-5ag3-0cu0-5/

Chapter 5. Conclusions

The real-time viewing methodology was successful in allowing for simultaneous imaging and resistance measurements of the studied solder joints, revealing multiple failure types stemming from EM, such as void nucleation and growth, crack propagation, and brittle fracture due to IMC formation. Instead of performing acceleration through high temperature testing, these tests were truly accelerated through cross-sectioning, achieving complete failure and repeatable results in roughly 300 h at temperatures below 100 °C. These tests have the potential to provide better failure time estimation than high temperature testing, while still providing the necessary acceleration.

Furthermore, real-time viewing of solder joints was successful in tracing the changes due to current stressing. This is important for identifying details about the location of failure mechanisms, including void formation, shifting location of current crowding caused by internal stresses and cracks, interconnection of different failure mechanisms, and changes in the solder joint microstructure after current stressing. Thus, capturing images at different time frames is important to pinpoint the cause of these changes in contrast to taking images only after failure. Real-time viewing can provide improved understanding in the study of electromigration in solder joints. Factors such as IMC and hillock formation as well as grain rotation could be better understood through in-situ imaging. Ultimately, the exact onset of void formation in this paper was only observed due to the in-situ behavior of the test setup, highlighting this method's significance. Furthermore, real-time viewing helps identify failure-prone locations in a solder joint and accelerate EM failure. Most importantly, real-time viewing allows for comparing samples under the same accelerated conditions to obtain optimized parameters that minimize reliability concerns.

In addition to the real-time viewing capability, the temperature estimation of a solder joint under current stressing resulted in a low estimation error and is a more accurate temperature estimation of individual solder joints compared to the use of a conventional temperature sensor. Joule heating cannot be ignored in typical EM testing as due to its substantial magnitude and change. The fraction of electrical energy consumed by electromigration remains to be studied.

In constant current EM tests, Joule heating is not constant but is mainly increasing, leading to an ever-accelerating joint stressing. More accelerated and more advanced EM testing methodologies with better control on specimen temperature during the test are conceivable as well as more reliable definitions and experimental data for time-to-failure.

The microstructural evolution of a cross-sectioned solder joint coupled with in-situ resistance and temperature measurements helped identify another shortcoming of typical EM testing when the sample broke upon cool-down. This demonstrated the resistance of a mortally damaged DUT can appear healthy, remaining below the failure limit during current stressing for too long, while at the same time it cannot survive the thermal stress of the test end.

With the accurate determination of the in-situ temperature of the solder joint during EM testing, design verification of test vehicles could be performed aiming at separating the effects of thermomigration from those of EM. This would be achieved by increasing current density and decreasing the thermal resistance of solder joints. Such effect separation is believed helpful for any further deepening of the understanding of EM in electronics packaging.

References

[1] B. Willis, Reflow Soldering Processes and Troubleshooting SMT, BGA, CSP and Flip Chip Technologies, Solder. Surf. Mt. Technol. (2003). https://doi.org/10.1108/ssmt.2003.21915aae.003.

[2] C. Chen, H.M. Tong, K.N. Tu, Electromigration and thermomigration in Pb-free flip-chip solder joints, Annu. Rev. Mater. Res. (2010). https://doi.org/10.1146/annurev.matsci.38.060407.130253.

[3] K.-N. Tu, Solder Joint Technology- Materials, Properties, and Reliability, Reactions. 117 (2007) 373. https://doi.org/10.1007/978-0-387-38892-2.

[4] K. Tu, Solder Joint Technology- Materials, Properties, and Reliability, Reactions. (2007).

[5] M. Date, T. Shoji, M. Fujiyoshi, K. Sato, K.N. Tu, Ductile-to-brittle transition in Sn-Zn solder joints measured by impact test, Scr. Mater. (2004). https://doi.org/10.1016/j.scriptamat.2004.06.027.

[6] J. en Luan, T.Y. Tee, E. Pek, C.T. Lim, Z. Zhong, Dynamic responses and solder joint reliability under board level drop test, Microelectron. Reliab. (2007). https://doi.org/10.1016/j.microrel.2006.05.012.

[7] S.F. Wong, P. Malatkar, C. Rick, V. Kulkami, I. Chin, Vibration testing and analysis of ball grid array package solder joints, in: Proc. - Electron. Components Technol. Conf., 2007. https://doi.org/10.1109/ECTC.2007.373825.

[8] F.X. Che, J.H.L. Pang, Vibration reliability test and finite element analysis for flip chip solder joints, Microelectron. Reliab. (2009). https://doi.org/10.1016/j.microrel.2009.03.022.

[9] L. Xu, J.H.L. Pang, F. Che, Impact of thermal cycling on Sn-Ag-Cu solder joints and board-level drop reliability, J. Electron. Mater. (2008). https://doi.org/10.1007/s11664-008-0400-0.

[10] J. Lienig, M. Thiele, Fundamentals of electromigration-aware integrated circuit design, 2018. https://doi.org/10.1007/978-3-319-73558-0.

[11] JEDEC, Guideline for characterizing solder bump electromigration under constant current and temperature stress, n.d. https://www.jedec.org/standards-documents/docs/jep-154.

[12] J.R. Black, Electromigration—A Brief Survey and Some Recent Results, IEEE Trans. Electron Devices. 16 (1969) 338–347. https://doi.org/10.1109/T-ED.1969.16754.

[13] H. Gan, W.J. Choi, G. Xu, K.N. Tu, Electromigration in solder joints and solder lines, Jom. 54 (2002) 34–37. https://doi.org/10.1007/BF02701847.

[14] I.A. Blech, Electromigration in thin aluminum films on titanium nitride, J. Appl. Phys. (1976). https://doi.org/10.1063/1.322842.

[15] H.U. Schreiber, B. Grabe, Electromigration measuring techniques for grain boundary

diffusion activation energy in aluminum, Solid State Electron. (1981). https://doi.org/10.1016/0038-1101(81)90182-9.

[16] M. Shatzkes, J.R. Lloyd, A model for conductor failure considering diffusion concurrently with electromigration resulting in a current exponent of 2, J. Appl. Phys. 59 (1986) 3890–3893. https://doi.org/10.1063/1.336731.

[17] R. Spolenak, O. Kraft, E. Arzt, Effects of alloying elements on electromigration, Microelectron. Reliab. (1998). https://doi.org/10.1016/S0026-2714(98)00110-3.

[18] S. Beyne, O.V. Pedreira, H. Oprins, I. De Wolf, Z. Tokei, K. Croes, Electromigration Activation Energies in Alternative Metal Interconnects, IEEE Trans. Electron Devices. (2019). https://doi.org/10.1109/TED.2019.2949196.

[19] M.F. Abdulhamid, C. Basaran, Y.S. Lai, Thermomigration versus electromigration in microelectronics solder joints, IEEE Trans. Adv. Packag. (2009). https://doi.org/10.1109/TADVP.2009.2018293.

[20] H. Ye, C. Basaran, D. Hopkins, Thermomigration in Pb-Sn solder joints under joule heating during electric current stressing, Appl. Phys. Lett. (2003). https://doi.org/10.1063/1.1554775.

[21] F.Y. Ouyang, C.L. Kao, In situ observation of thermomigration of Sn atoms to the hot end of 96.5Sn-3Ag-0.5Cu flip chip solder joints, J. Appl. Phys. (2011). https://doi.org/10.1063/1.3671404.

[22] T.Y. Lee, K.N. Tu, S.M. Kuo, D.R. Frear, Electromigration of eutectic SnPb solder interconnects for flip chip technology, J. Appl. Phys. 89 (2001) 3189–3194. https://doi.org/10.1063/1.1342023.

[23] J.W. Nah, J.O. Suh, K.N. Tu, S.W. Yoon, V.S. Rao, V. Kripesh, F. Hua, Electromigration in flip chip solder joints having a thick Cu column bump and a shallow solder interconnect, J. Appl. Phys. 100 (2006). https://doi.org/10.1063/1.2402475.

[24] Y.W. Chang, Y. Cheng, L. Helfen, F. Xu, T. Tian, M. Scheel, M. Di Michiel, C. Chen, K.N. Tu, T. Baumbach, Electromigration Mechanism of Failure in Flip-Chip Solder Joints Based on Discrete Void Formation, Sci. Rep. 7 (2017) 1–16. https://doi.org/10.1038/s41598-017-06250-8.

[25] J.R. Black, Electromigration Failure Modes in Aluminum Metallization for Semiconductor Devices, Proc. IEEE. 57 (1969) 1587–1594. https://doi.org/10.1109/PROC.1969.7340.

[26] M.A. Korhonen, P. Borgesen, K.N. Tu, C.Y. Li, Stress evolution due to electromigration in confined metal lines, J. Appl. Phys. 73 (1993) 3790–3799. https://doi.org/10.1063/1.354073.

[27] G. Scotti, Electromigration in Solder Interconnects, 2008. https://www.researchgate.net/publication/235994499_Electromigration_in_Solder_Interconnects.

[28] A. Geczy, D. Straubinger, A. Kovacs, O. Krammer, P. Mach, G. Harsányi, Effects of high current density on lead-free solder joints of chip-size passive SMD components, Solder.

Surf. Mt. Technol. (2018). https://doi.org/10.1108/SSMT-10-2017-0032.

[29] D. Straubinger, A. Géczy, A. Sipos, A. Kiss, D. Gyarmati, O. Krammer, D. Rigler, D. Bušek, G. Harsányi, Advances on high current load effects on lead-free solder joints of SMD chip-size components and BGAs, Circuit World. (2019). https://doi.org/10.1108/CW-11-2018-0088.

[30] R. Rosenberg, D.C. Edelstein, C.K. Hu, K.P. Rodbell, Copper metallization for high performance silicon technology, Annu. Rev. Mater. Sci. 30 (2000) 229–262. https://doi.org/10.1146/annurev.matsci.30.1.229.

[31] E.C.C. Yeh, W.J. Choi, K.N. Tu, P. Elenius, H. Balkan, Current-crowding-induced electromigration failure in flip chip solder joints, Appl. Phys. Lett. 80 (2002) 580–582. https://doi.org/10.1063/1.1432443.

[32] L. Meinshausen, H. Frémont, K. Weide-Zaage, Migration induced IMC formation in SAC305 solder joints on Cu, NiAu and NiP metal layers, Microelectron. Reliab. 52 (2012) 1827–1832. https://doi.org/10.1016/j.microrel.2012.06.127.

[33] M.F. Abdulhamid, C. Basaran, Y.S. Lai, Thermomigration versus electromigration in microelectronics solder joints, IEEE Trans. Adv. Packag. 32 (2009) 627–635. https://doi.org/10.1109/TADVP.2009.2018293.

[34] Y.W. Chang, C.C. Hu, H.Y. Peng, Y.C. Liang, C. Chen, T.C. Chang, C.J. Zhan, J.Y. Juang, A new failure mechanism of electromigration by surface diffusion of Sn on Ni and Cu metallization in microbumps, Sci. Rep. 8 (2018) 1–10. https://doi.org/10.1038/s41598-018-23809-1.

[35] L.D. Chen, M.L. Huang, S.M. Zhou, Effect of electromigration on intermetallic compound formation in line-type Cu/Sn/Cu interconnect, J. Alloys Compd. 504 (2010) 535–541. https://doi.org/10.1016/j.jallcom.2010.05.158.

[36] A. Sharma, D.E. Xu, J. Chow, M. Mayer, H.R. Sohn, J.P. Jung, Electromigration of composite Sn-Ag-Cu solder bumps, Electron. Mater. Lett. 11 (2015) 1072–1077. https://doi.org/10.1007/s13391-015-4454-x.

[37] D.E. Xu, J. Chow, M. Mayer, J.P. Jung, J.H. Yoon, Sn-Ag-Cu to Cu joint current aging test and evolution of resistance and microstructure, Electron. Mater. Lett. 11 (2015) 1078–1084. https://doi.org/10.1007/s13391-015-5201-z.

[38] Y.C. Chan, D. Yang, Failure mechanisms of solder interconnects under current stressing in advanced electronic packages, Prog. Mater. Sci. 55 (2010) 428–475. https://doi.org/10.1016/j.pmatsci.2010.01.001.

[39] I.J. Ringler, J.R. Lloyd, Stress relaxation in pulsed DC electromigration measurements, AIP Adv. 6 (2016). https://doi.org/10.1063/1.4963669.

[40] Y. Dan, Study on Reliability of Flip Chip Solder Interconnects for High Current Density Packaging, City University of Hong Kong, 2009. https://scholars.cityu.edu.hk/en/theses/theses(fbba05d6-d612-4ae7-8bfb-b15a5746763d).html.

[41] A.T. Huang, A.M. Gusak, K.N. Tu, Y.S. Lai, Thermomigration in SnPb composite flip chip solder joints, Appl. Phys. Lett. 88 (2006). https://doi.org/10.1063/1.2192694.

[42] Y.H. Lin, Y.C. Hu, C.M. Tsai, C.R. Kao, K.N. Tu, In situ observation of the void formation-and-propagation mechanism in solder joints under current-stressing, Acta Mater. (2005). https://doi.org/10.1016/j.actamat.2005.01.014.

[43] S. Chatterjee, V. Sukharev, F.N. Najm, Power Grid Electromigration Checking Using Physics-Based Models, IEEE Trans. Comput. Des. Integr. Circuits Syst. (2018). https://doi.org/10.1109/TCAD.2017.2666723.

[44] M.L. Huang, J.M. Kuang, H.Y. Sun, Electromigration-induced β-Sn grain rotation in lead-free flip chip solder bumps, in: Proc. - Electron. Components Technol. Conf., 2019. https://doi.org/10.1109/ECTC.2019.00312.

[45] C. Basaran, S. Li, D.C. Hopkins, D. Veychard, Electromigration time to failure of SnAgCuNi solder joints, J. Appl. Phys. (2009). https://doi.org/10.1063/1.3159012.

[46] D.G. Pierce, P.G. Brusius, Electromigration: A review, Microelectron. Reliab. (1997). https://doi.org/10.1016/s0026-2714(96)00268-5.

[47] H.U. Schreiber, Activation energies for the different electromigration mechanisms in aluminum, Solid State Electron. (1981). https://doi.org/10.1016/0038-1101(81)90080-0.

[48] M. Technology, BGA Manufacturer's User Guide for Micron BGA Parts, 2020.

[49] M. Abdelaziz, D. Erick, G. Wang, M. Mayer, Microelectronics Reliability Electromigration in solder joints : A cross-sectioned model system for real-time observation, Microelectron. Reliab. 119 (2021) 114068. https://doi.org/10.1016/j.microrel.2021.114068.

[50] MG Chemicals, Lead Free Solder Sn96 (SAC305) 4900 Technical Data Sheet, 2016. https://www.techsil.co.uk/media/pdf/TDS/MGEN00015-tds.pdf.

[51] alpha A. SOLUTIONS, ALPHA Vaculoy SAC300,305,350,400,405, 2017.

[52] J.W. Nah, J.O. Suh, K.N. Tu, Effect of current crowding and Joule heating on electromigration-induced failure in flip chip composite solder joints tested at room temperature, J. Appl. Phys. (2005). https://doi.org/10.1063/1.1949719.

[53] S. Karajgikar, V. Nagaraj, D. Agonafer, S. Pekin, Flip chip back end design parameters to reduce bump electromigration, in: Proc. - Electron. Components Technol. Conf., 2008. https://doi.org/10.1109/ECTC.2008.4549994.

[54] J. Feng, D.E. Xu, Y. Tian, M. Mayer, SAC305 Solder Reflow: Identification of Melting and Solidification Using In-Process Resistance Monitoring, IEEE Trans. Components, Packag. Manuf. Technol. (2019). https://doi.org/10.1109/tcpmt.2019.2901651.

[55] M. AbdelAziz, M. Mayer, In-situ Determination of Specimen Temperature during Electromigration Testing of Solder Joint, in: IEEE 71st Electron. Components Technol. Conf., 2021. Manuscript submitted for publication.

[56] J.H. Lau, P.A. Engel, Solder Joint Reliability—Theory and Applications, J. Electron.

Packag. (1992). https://doi.org/10.1115/1.2905434.

[57] M.A. Previti, M. Holtzer, T. Hunsinger, Four ways to reduce voids in BGA/CSP package to substrate connections, Surf. Mt. Light Emit. Diodes Conf. (2011).

[58] T.D. Ewald, N. Holle, K.J. Wolter, Void formation during reflow soldering, in: Proc. - Electron. Components Technol. Conf., 2012. https://doi.org/10.1109/ECTC.2012.6249064.

[59] L. Zhang, Z.G. Wang, J.K. Shang, Current-induced weakening of Sn3.5Ag0.7Cu Pb-free solder joints, Scr. Mater. (2007). https://doi.org/10.1016/j.scriptamat.2006.10.043.

[60] Q. Wang, Q. Liu, Z. Zhang, M. Miao, Y. Su, F. Su, An observation and explanation of interior cracking at the interface of solder by electromigration, Microelectron. Reliab. (2019). https://doi.org/10.1016/j.microrel.2019.04.013.

[61] S.W. Liang, Y.W. Chang, T.L. Shao, C. Chen, K.N. Tu, Effect of three-dimensional current and temperature distributions on void formation and propagation in flip-chip solder joints during electromigration, Appl. Phys. Lett. (2006). https://doi.org/10.1063/1.2220550.

[62] B.K. Synkiewicz, A. Skwarek, K. Witek, Voids investigation in solder joints performed with vapour phase soldering (VPS), Solder. Surf. Mt. Technol. (2014). https://doi.org/10.1108/SSMT-10-2013-0028.

[63] C.Y. Liu, J.T. Chen, Y.C. Chuang, L. Ke, S.J. Wang, Electromigration-induced Kirkendall voids at the Cu/Cu3Sn interface in flip-chip Cu/Sn/Cu joints, Appl. Phys. Lett. (2007). https://doi.org/10.1063/1.2714100.

[64] B. Stahlmecke, F.J. Meyer Zu Heringdorf, L.I. Chelaru, M. Horn-Von Hoegen, G. Dumpich, K.R. Roos, Electromigration in self-organized single-crystalline silver nanowires, Appl. Phys. Lett. (2006). https://doi.org/10.1063/1.2172012.

[65] Q. Yu, T. Shibutani, D.S. Kim, Y. Kobayashi, J. Yang, M. Shiratori, Effect of process-induced voids on isothermal fatigue resistance of CSP lead-free solder joints, Microelectron. Reliab. (2008). https://doi.org/10.1016/j.microrel.2007.08.008.

Appendix A: List of components

Table A-1: Complete list of components used for EM test

Equipment	**Model Number**
Power Supply	Keysight 1xN6700C+4xN6751A
Oven	FP053UL-120V (with 100mm access port with silicon plug on right)
High Temperature Cables	20 ft. Daburn 2609/50
High Temperature Connectors	5xSullins WMC18DRYI
Multiplexer	Keithley 2x7708+1x2700
Voltmeter	Keysight 1x34220A
Custom PCB Carrier	Flip chip configuration solder PCB
D-sub Connectors (5A current rating, 5 pairs, 36 position or higher)	(5xL17DCFRA37S) + (5xL17DCFRA37P)
Ribbon Cables (5A current rating, >32 wire ribbon cables, >40 ft, easily ripped) - matching with D-sub connectors	310J101-50
High Temperature Insulation-Displacement Connector (IDC) (36 contacts, 0.1 in pitch, >200°C)	5xMAS-CON IDC
GPIB	(1xGPIB-USB Adapter) + (2xGPIB Connectors)
RTD Sensors	PT1000
PC	With Python (Spyder)[5]
Software	Testing Matlab Codes
Mechanical Support System	Custom-made (see Appendix) Off-the-shelf components per Hanger-Spring Design: 6 x Extension Springs: 1.75” length 20 x Screws: 4-40 thread size, ½” long 20 x Nuts: 4-40 thread size Same components are required for the Hanger-Hook Design with the exception of springs (no springs required)

[5] https://www.spyder-ide.org/

Appendix B: Custom-made components

In addition to the off-the-shelf components, some equipment was manufactured to accommodate the custom-made PCBs. The components for the mechanical support system are shown in Table A-1.

1) Mechanical support for card edge connectors

In order to test multiple testing boards simultaneously, a mechanical support is needed to hold multiple card edge connectors inside the oven, which are used to connect the PCB to the multiplexer. A mechanical support is thus required to ensure an adequate number of connectors can fit securely inside the oven. The availability of the racks inside the oven was seen as an advantage since a mechanical support which incorporated the racks can be used, as opposed to building a new mechanical support which has to be stable on its own when held vertically. Utilizing the racks, a hanger-spring design was generated, in which a pair of springs would be attached to the design, and each of those springs would be attached to the top and bottom racks. This design would minimize any rotations which could occur due to the air convection which is generated by the fan inside the oven. Another design that incorporates the racks was also generated. Instead of using springs, a hook-like mechanism was used which allows for attaching the component directly onto the racks. Both designs are shown in Figure B-1.

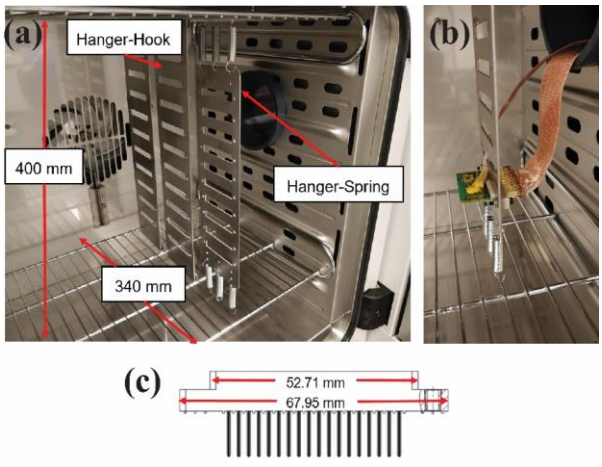

Figure B-1: Mechanical design showing (a) both hanger concepts, (b) card edge connector attached to hanger, and (c) dimensions of card edge connector

2) Epoxy 3D-printed mold

During the preparation of the test vehicle for microscopy, the test vehicle has to be cured in epoxy to provide support to the solder joints during the shear cutting and grinding processes. No off-the-shelf components were available in the market that would be a perfect fit for the PCB and reduce the amount of epoxy wasted.

A 3D-printed mold was designed and printed using PLA to allow for an optimized curing process, as shown in Figure B-2.

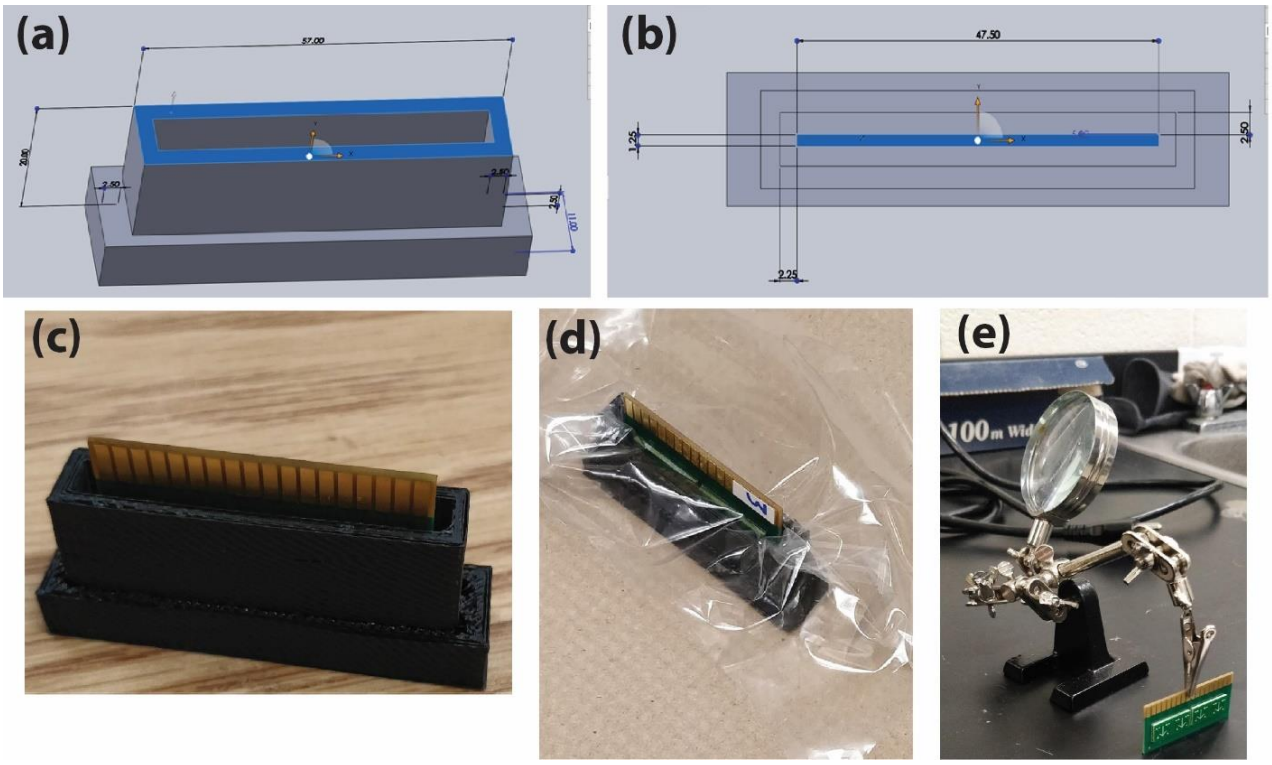

Figure B-2: Epoxy mold, showing (a) CAD model in Solidworks. Dimensions in mm (b) top view of component, (c) component after 3D printing and PCB inversion, (d) plastic wrap usage to allow for reusable mold and (e) use of soldering helping hand to hold PCB in place during curing.

Appendix C: Setup automation

1) In-situ resistance measurement code

Filename: In-situ resistance measurements from Keithley 2700 MUX.py

```
"""
@author: Mostafa AbdelAziz
Resistance measurements of 2 PCBs connected to Keithley 2700 MUX using 2 card
edge connectors
"""
from IPython import get_ipython;
get_ipython().magic('reset -sf')

from itertools import chain
import pyvisa as visa
import time
import matplotlib.pyplot as plt
import scipy.io
from math import sqrt

def roots(a,b,c):
    disc = b**2 - 4*a*c
    if disc >= 0:
        if ((-b + sqrt(disc))/(2*a))<300 and ((-b + sqrt(disc))/(2*a))>0:
            return (-b + sqrt(disc))/(2*a)
        elif ((-b - sqrt(disc))/(2*a))<300 and ((-b - sqrt(disc))/(2*a))>0:
            return (-b - sqrt(disc))/(2*a)
    else:
        return -10000000

plt.close('all')

RealTimeReadings = 1;
sampleName = 'Resistance Measurements of SAC305 flip
chip_started_Nov25_samples A7 and A8_preconditioning_150°C';
SetCurrent = 5;
failureflag = 0;

A = 3.9083e-3;
B = -5.775e-7;
RTD0 = 1000;

t = []
T1 = []
T2 = []
T3 = []
T4 = []
R = [[] for z in range(16)]
Vpcb1 = [[] for z in range(16)]
Vpcb2 = [[] for z in range(16)]
Tread1 = []
Tread2 = []
Tread3 = []
```

```
Tread4 = []

fname=time.strftime("%y%m%d%H%M%S",time.localtime()) + sampleName #filename
#GPIB INITIALIZATION WITH PYVISA
rm = visa.ResourceManager()
rm.list_resources()
multiplexer = rm.open_resource('USB0::0x0957::0x0507::MY45000023::0::INSTR')

channel1=['@2001','@2002','@2003','@2004','@2005','@2006','@2007','@2008','@2
009','@2010','@2011','@2012','@2013','@2014','@2015','@2016']
channel2=['@2021','@2022','@2023','@2024','@2025','@2026','@2027','@2028','@2
029','@2030','@2031','@2032','@2033','@2034','@2035','@2036']
color=['b','b--','g','g--','r','r--','c','c--','m','m--','y','y--','k','k--
','b-.','b:']

tic = time.perf_counter()

while failureflag == 0:
        toc=time.perf_counter()
        t.append(toc-tic)
#         try:
        for j in range (16):
            dc1 = multiplexer.query(':MEASure:SCALar:VOLTage:DC? (%s)' %
(channel1[j]))
            cur = float(5)
            #The MUX saves the data with VDC and other characters after the
number. The following obtains the numbers only:
            sep = 'VDC'
            rest = dc1.split(sep, 1)[0]
            #If there is an OC, MUX records +9.9E37,... This next part
removes parts after ","
            sep1 = ','
            rest1 = rest.split(sep1, 1)[0]
            rest2 = float(rest1)
            Vpcb1[j].append(rest2)

            dc2 = multiplexer.query(':MEASure:SCALar:VOLTage:DC? (%s)' %
(channel2[j]))
            rest3 = dc2.split(sep, 1)[0]
            rest4 = rest3.split(sep1, 1)[0]
            rest5 = float(rest4)
            Vpcb2[j].append(rest5)

            temp_values1 =
multiplexer.query_ascii_values(':MEASure:SCALar:FRESistance? (%s)'
%('@4001'))
            opc1 = int(temp_values1[0])
            RR1 = roots(B*RTD0, A*RTD0, RTD0-float(opc1));

            # temp_values2 =
multiplexer.query_ascii_values(':MEASure:SCALar:FRESistance? (%s)'
%('@4002'))
            # opc2 = int(temp_values2[0])
            # RR2 = roots(B*RTD0, A*RTD0, RTD0-float(opc2));
```

```
            # temp_values3 =
multiplexer.query_ascii_values(':MEASure:SCALar:FRESistance? (%s)'
%('@4003'))
            # opc3 = int(temp_values3[0])
            # RR3 = roots(B*RTD0, A*RTD0, RTD0-float(opc3));

            # temp_values4 =
multiplexer.query_ascii_values(':MEASure:SCALar:FRESistance? (%s)'
%('@4004'))
            # opc4 = int(temp_values4[0])
            # RR4 = roots(B*RTD0, A*RTD0, RTD0-float(opc4));

        Tread1.append(RR1)
        # Tread2.append(RR2)
        # Tread3.append(RR3)
        # Tread4.append(RR4)


        ff = plt.figure(1)
        plt.cla()
        #list1= chain(range(1,5), range(7,8), range(14,16))
        list1= chain(range(1,13), range(14,16))
        for w in list1:
            plt.plot(t,Vpcb1[w], '%s' %color[w])
        plt.xlabel('Time [s]')
        plt.ylabel('Voltage [mV]')
        plt.ion()
        plt.show()
        ff.canvas.draw()
        ff.canvas.flush_events()

        ff = plt.figure(2)
        plt.cla()
        #list2= chain(range(1,5), range(7,8), range(14,16))
        list2= chain(range(1,16))
        for w in list2:
            plt.plot(t,Vpcb2[w], '%s' %color[w])
        plt.xlabel('Time [s]')
        plt.ylabel('Voltage [mV]')
        plt.ion()
        plt.show()
        ff.canvas.draw()
        ff.canvas.flush_events()

        plt.ion()
        gg = plt.figure(3)
        plt.cla()
        plt.plot(t[max(0, len(t)-300):],Tread1[max(0, len(t)-300):])
        # plt.plot(t[max(0, len(t)-300):],Tread2[max(0, len(t)-300):])
        # plt.plot(t[max(0, len(t)-300):],Tread3[max(0, len(t)-300):])
        # plt.plot(t[max(0, len(t)-300):],Tread4[max(0, len(t)-300):])
        plt.xlabel('Time [s]')
        plt.ylabel('Temperature [℃]')
        plt.show()
        gg.canvas.draw()
        gg.canvas.flush_events()
```

```
        data = {}
        data['t'] = t
        data['R'] = R
        data['T1'] = T1
        # data['T2'] = T2
        # data['T3'] = T3
        # data['T4'] = T4
        data['Tread1'] = Tread1
        # data['Tread2'] = Tread2
        # data['Tread3'] = Tread3
        # data['Tread4'] = Tread4
        data['Vpcb1'] = Vpcb1
        data['Vpcb2'] = Vpcb2
        saved = 0
        while saved == 0:
            try:
                scipy.io.savemat('%s.mat' % fname, data)
                saved = 1
            except:
                saved = 0
        #time.sleep(5)
        maxlength2save = 10000000
        if len(t) > maxlength2save:
            fname=time.strftime("%y%m%d%H%M%S",time.localtime()) + sampleName
#filename
            t = []
            T1 = []
            # T2 = []
            # T3 = []
            # T4 = []
            R = [[] for z in range(16)]
            V = [[] for z in range(16)]
            Vpcb1 = [[] for z in range(16)]
            Vpcb2 = [[] for z in range(16)]

multiplexer.close()
rm.close()
```

2) Resistance measurement post-processing plotting code

Filename: Plotting resistance measurements from Keithley 2700 MUX.py

```
#@author: m8abdela, MIJO34
from itertools import chain
import scipy.io
import matplotlib.pyplot as plt
import numpy as np
import matplotlib.patches as mpatches

test1 = scipy.io.loadmat('201002170354Resistance Measurements of SAC305 flip
chip_startedOct2,5PM,SolderJoint.mat')
print(type(test1))


channel1=['@101','@102','@103','@104','@105','@106','@107','@108','@109','@11
0','@111','@112','@113','@114','@115','@116']
channel2=['@201','@202','@203','@204','@205','@206','@207','@208','@209','@21
0','@211','@212','@213','@214','@215','@216']
color=['b','b--','g','g--','r','r--','c','c--','m','m--','y','y--','k','k--
','b-.','b:']

#Test 1
R1=test1['R']
t1=test1['t']
T1=test1['T1']
T2=test1['T2']
T3=test1['T3']
Vpcb1=test1['Vpcb1']
Vpcb2=test1['Vpcb2']
Tread1=test1['Tread1']
Tread2=test1['Tread2']
#
##Plotting
## Resistance Vs. Time
#ax=plt.figure()
##list1= chain(range(1,5), range(7,10), range(15,16))
##for w in list1:
##for w in [x for x in range(16) if x != 9]:
#plt.plot(t1[0]/3600,Vpcb1[15], '%s' %color[0])
##plt.plot((ttotal[0]/3600),(Vpcb1_total[0]), linewidth=2.0)
#ax.legend(fontsize=24)
#plt.xlabel('Time [hrs]', fontsize=34)
#plt.rcParams['xtick.labelsize']=34
#plt.rcParams['ytick.labelsize']=34
#plt.ylabel('Resistance [mΩ]',fontsize=34)
#plt.show()

# Temperature Vs. Time
ax=plt.figure()
plt.plot((t1[0]/3600),(Tread1[0]), linewidth=2.0)
plt.plot((t1[0]/3600),(Tread2[0]), linewidth=2.0)
ax.legend(fontsize=24)
plt.xlabel('Time [hrs]', fontsize=34)
plt.rcParams['xtick.labelsize']=34
```

```
plt.rcParams['ytick.labelsize']=34
plt.ylabel('Temperature [°C]',fontsize=34)
plt.show()


#Plotting
# Resistance Vs. Time
ax=plt.figure()
plt.plot(t1[0]/3600,Vpcb1[0], '%s' %color[0])
ax.legend(fontsize=24)
plt.xlabel('Time [hrs]', fontsize=34)
plt.rcParams['xtick.labelsize']=34
plt.rcParams['ytick.labelsize']=34
plt.ylabel('Voltage [mV]',fontsize=34)
plt.show()

#Plotting
# Resistance Vs. Time
ax=plt.figure()
plt.plot(t1[0]/3600,Vpcb1[1], '%s' %color[0])
ax.legend(fontsize=24)
plt.xlabel('Time [hrs]', fontsize=34)
plt.rcParams['xtick.labelsize']=34
plt.rcParams['ytick.labelsize']=34
plt.ylabel('Voltage [mV]',fontsize=34)
plt.show()

#Plotting
# Resistance Vs. Time
ax=plt.figure()
plt.plot(t1[0]/3600,Vpcb1[2], '%s' %color[0])
ax.legend(fontsize=24)
plt.xlabel('Time [hrs]', fontsize=34)
plt.rcParams['xtick.labelsize']=34
plt.rcParams['ytick.labelsize']=34
plt.ylabel('Voltage [mV]',fontsize=34)
plt.show()

#Plotting
# Resistance Vs. Time
ax=plt.figure()
plt.plot(t1[0]/3600,Vpcb1[3], '%s' %color[0])
ax.legend(fontsize=24)
plt.xlabel('Time [hrs]', fontsize=34)
plt.rcParams['xtick.labelsize']=34
plt.rcParams['ytick.labelsize']=34
plt.ylabel('Voltage [mV]',fontsize=34)
plt.show()

#Plotting
# Resistance Vs. Time
ax=plt.figure()
plt.plot(t1[0]/3600,Vpcb1[4], '%s' %color[0])
ax.legend(fontsize=24)
plt.xlabel('Time [hrs]', fontsize=34)
plt.rcParams['xtick.labelsize']=34
```

```
plt.rcParams['ytick.labelsize']=34
plt.ylabel('Voltage [mV]',fontsize=34)
plt.show()

#Plotting
# Resistance Vs. Time
ax=plt.figure()
plt.plot(t1[0]/3600,Vpcb1[5], '%s' %color[0])
ax.legend(fontsize=24)
plt.xlabel('Time [hrs]', fontsize=34)
plt.rcParams['xtick.labelsize']=34
plt.rcParams['ytick.labelsize']=34
plt.ylabel('Voltage [mV]',fontsize=34)
plt.show()

#Plotting
# Resistance Vs. Time
ax=plt.figure()
plt.plot(t1[0]/3600,Vpcb1[6], '%s' %color[0])
ax.legend(fontsize=24)
plt.xlabel('Time [hrs]', fontsize=34)
plt.rcParams['xtick.labelsize']=34
plt.rcParams['ytick.labelsize']=34
plt.ylabel('Voltage [mV]',fontsize=34)
plt.show()

#Plotting
# Resistance Vs. Time
ax=plt.figure()
plt.plot(t1[0]/3600,Vpcb1[7], '%s' %color[0])
ax.legend(fontsize=24)
plt.xlabel('Time [hrs]', fontsize=34)
plt.rcParams['xtick.labelsize']=34
plt.rcParams['ytick.labelsize']=34
plt.ylabel('Voltage [mV]',fontsize=34)
plt.show()

#Plotting
# Resistance Vs. Time
ax=plt.figure()
plt.plot(t1[0]/3600,Vpcb1[8], '%s' %color[0])
ax.legend(fontsize=24)
plt.xlabel('Time [hrs]', fontsize=34)
plt.rcParams['xtick.labelsize']=34
plt.rcParams['ytick.labelsize']=34
plt.ylabel('Voltage [mV]',fontsize=34)
plt.show()
```

3) Current stressing code

Filename: Hanmatek DC Power Supply Current Stressing.py
Used to obtain data shown in Figure 4.3.

```
# import TestModbusScript
Credits go to sperim, who created the original code, found on sourceforge:
https://sourceforge.net/projects/dc-power-supply-software/

from itertools import chain
import visa
import scipy.io
import numpy as np
from tkinter import *
import tkinter.ttk as ttk
from tkinter import messagebox
from pymodbus.client.sync import ModbusSerialClient
import time
from time import sleep

"""Window Definition"""

device = []
connection = False


class MyWindow(Frame):
    unit_id = 1
    method = "rtu"
    baudrate = 9600
    bytesize = 8
    parity = "N"
    stopbits = 1
    timeout = 0.25

    def __init__(self, parent):
        self.parent = parent
        Frame.__init__(self, parent)
        """definitions"""

        self.connectedText = StringVar()
        self.connectedText.set("Not Connected")
#         self.tkValueVoltageRead = StringVar()
#         self.tkValueVoltageRead.set("0.0")
#         self.tkValueCurrentRead = StringVar()
#         self.tkValueCurrentRead.set("0.0")
#         self.tkValuePowerRead = StringVar()
#         self.tkValuePowerRead.set("0.0")
        self.tkValueVoltageWrite = StringVar()
        self.tkValueVoltageWrite.set("32.0")
        self.tkValueCurrentWrite = StringVar()
        self.tkValueCurrentWrite.set("0.1")
        self.tkValuePowerWrite = StringVar()
        self.tkValuePowerWrite.set("0.0")
```

```
        """COM Port Fields"""
        comport_label = Label(self, bd=5, width=40, text="COM Port")
        self.tkCOMPort = StringVar(self)
        self.tkCOMPort.set("COM11")
        comport_entry = OptionMenu(self, self.tkCOMPort, "COM1", "COM2",
"COM3", "COM4", "COM5", "COM6", "COM7", "COM8",
                                   "COM8",
                                   "COM9", "COM10", "COM11", "COM12",
"COM13", "COM14", "COM15", "COM16")
        connect_button = Button(self, bd=5, text="Connect",
command=self.connect_device)
        disconnect_button = Button(self, bd=5, text="Disconnect",
command=self.disconnect_device)
        self.connectedText.set("Disconnected")
        self.connected_label = Label(self, bd=5, width=40, bg="red",
textvariable=self.connectedText)

        """Controller"""
        controlledValues_label = Label(self, bd=5, width=40,
text="Controllable Values")
        controlledVoltage_label = Label(self, bd=5, width=20, text="Voltage")
        self.voltage_value_write = Entry(self,
textvariable=self.tkValueVoltageWrite)
        voltage_submit = Button(self, bd=5, text="Submit",
command=self.submit_voltage)
        controlledCurrent_label = Label(self, bd=5, width=20, text="Current")
        self.current_value_write = Entry(self,
textvariable=self.tkValueCurrentWrite)
        current_submit = Button(self, bd=5, text="Submit",
command=self.submit_current)
        """Output Control"""
        self.output_label = Label(self, bd=5, width=20, bg="red",
text="Output")
        output_button_on = Button(self, bd=5, text="On",
command=self.output_on)
        output_button_off = Button(self, bd=5, text="Off",
command=self.output_off)
        exit_button = Button(self, bd=5, text="Exit",
command=self.quit_program)
#         """Reader"""
#         self.readValues_label = Label(self, bd=5, width=40, text="Read
Values")
#         readVoltage_label = Label(self, bd=5, width=20, text="Voltage")
#         self.voltage_value_read = Entry(self, state="readonly",
textvariable=self.tkValueVoltageRead)
#         readCurrent_label = Label(self, bd=5, width=20, text="Current")
#         self.current_value_read = Entry(self, state="readonly",
textvariable=self.tkValueCurrentRead)
#         power_label = Label(self, bd=5, width=20, text="Power")
#         self.power_value_read = Entry(self, state="readonly",
textvariable=self.tkValuePowerRead)

        """Windows Format"""
        """COM Port"""
        comport_label.grid(row=0, column=0, columnspan=3, sticky="WE")
        comport_entry.grid(row=1, column=0, sticky="WE")
```

```
        connect_button.grid(row=1, column=1, sticky="WE")
        disconnect_button.grid(row=1, column=2, sticky="WE")
        ttk.Separator(self, orient=HORIZONTAL).grid(row=2, column=0,
columnspan=3, sticky="WE")
        self.connected_label.grid(row=3, column=0, columnspan=3, sticky="WE")
        ttk.Separator(self, orient=HORIZONTAL).grid(row=4, column=0,
columnspan=3, sticky="WE")
        """Controller"""
        controlledValues_label.grid(row=5, column=0, columnspan=3,
sticky="WE")
        controlledVoltage_label.grid(row=6, column=0, sticky="WE")
        self.voltage_value_write.grid(row=6, column=1, sticky="WE")
        voltage_submit.grid(row=6, column=2, sticky="WE")
        controlledCurrent_label.grid(row=7, column=0, sticky="WE")
        self.current_value_write.grid(row=7, column=1, sticky="WE")
        current_submit.grid(row=7, column=2, sticky="WE")
        self.output_label.grid(row=8, column=0, sticky="WE")
        output_button_on.grid(row=8, column=1, sticky="WE")
        output_button_off.grid(row=8, column=2, sticky="WE")
        ttk.Separator(self, orient=HORIZONTAL).grid(row=9, column=0,
columnspan=3, sticky="WE")
#         """Reader"""
#         self.readValues_label.grid(row=10, column=0, columnspan=3,
sticky="WE")
#         readVoltage_label.grid(row=11, column=0, sticky="WE")
#         self.voltage_value_read.grid(row=11, column=1, sticky="WE")
#         readCurrent_label.grid(row=12, column=0, sticky="WE")
#         self.current_value_read.grid(row=12, column=1, sticky="WE")
#         power_label.grid(row=13, column=0, sticky="WE")
#         self.power_value_read.grid(row=13, column=1, sticky="WE")
#         ttk.Separator(self, orient=HORIZONTAL).grid(row=14, column=0,
columnspan=3, sticky="WE")
#         exit_button.grid(row=15, column=0, columnspan=3, sticky="WE")

#     def shortIO(self):
#         device.write_register(address=int('1', 16), count=1, value=1,
unit=1)
#         time.sleep(0.25)
#         device.write_register(address=int('1', 16), count=1, value=0,
unit=1)

    def connect_device(self):
        global device
        global connection
        device = ModbusSerialClient(method=self.method,
port=self.tkCOMPort.get(),
                                    stopbits=self.stopbits,
bytesize=self.bytesize,
                                    parity=self.parity,
baudrate=self.baudrate,
                                    timeout=self.timeout)
        connection = device.connect()

        if not connection:
            messagebox.showerror("Error", "Problems connecting to COM port.
\n"
```

```
                                            "Please check the port.")
        else:
            self.connectedText.set("Connected")
            self.connected_label.config(bg="green")
            device.write_register(address=int('1', 16), count=1, value=1,
unit=1)

    def disconnect_device(self):
        global device
        global connection
        try:
            self.output_off()
            device.close()
            device = []
            connection = False
            self.connectedText.set("Disconnected")
            self.connected_label.config(bg="red")
        except AttributeError:
            messagebox.showerror("Error", "COM Port is disconnected!!!")

    def submit_voltage(self):
        try:
            voltageString4 = 3200
            transferString = int(voltageString4)
            device.write_register(address=int('30', 16), count=1,
value=transferString, unit=1)
        except AttributeError:
            messagebox.showerror("Error", "COM Port is disconnected!!!")

    def submit_current(self):
        try:
            Ilevels=[]
            I=[]
            Ilevelsetup = np.arange(0,10300,200)
            for objects in range(len(Ilevelsetup)):
                Ilevels.append((Ilevelsetup[objects]))
            n = 1
            ele = float(0)
            list(chain(*[Ilevels[i:i+n] + [ele] if len(Ilevels[i:i+n]) == n
else Ilevels[i:i+n] for i in range(0, len(Ilevels), n)]))
            for x in range(51):
                    device.write_register(address=int('31', 16), count=1,
value=Ilevels[x], unit=1)
                    time.sleep(10)
                    #chnage to 5
                    device.write_register(address=int('31', 16), count=1,
value=int(0), unit=1)
                    time.sleep(10)
        except AttributeError:
            messagebox.showerror("Error", "COM Port is disconnected!!!")

    def output_on(self):
        try:
            device.write_register(address=int('1', 16), count=1, value=1,
unit=1)
            self.output_label.config(bg="green")
```

```
            except AttributeError:
                messagebox.showerror("Error", "COM Port is disconnected!!!")

        def output_off(self):
            try:
                device.write_register(address=int('1', 16), count=1, value=0,
unit=1)
                self.output_label.config(bg="red")
            except AttributeError:
                messagebox.showerror("Error", "COM Port is disconnected!!!")

        def quit_program(self):
            if connection:
                self.disconnect_device()
            self.quit()

        def updateVoltage(self, voltage):
            self.tkValueVoltageRead.set(voltage)

        def updateCurrent(self, current):
            self.tkValueCurrentRead.set(current)

        def updatePower(self, power):
            self.tkValuePowerRead.set(power)

    def read_data(my_label):
        global device
        resultU = []
        resultI = []
        resultP = []
        if hasattr(device, "read_holding_registers"):
            result = device.read_holding_registers(address=16, count=4, unit=1)
            if hasattr(result, "unit_id"):
                voltageString1 = float(result.registers[0])
                voltageString2 = voltageString1 / 100.0
                transferString = str(voltageString2)
                my_label.updateVoltage(transferString)
                currentString1 = float(result.registers[1])
                currentString2 = currentString1 / 1000.0
                transferString = str(currentString2)
                my_label.updateCurrent(transferString)
                powerString1 = float(result.registers[2] + result.registers[3])
                powerString2 = powerString1 / 1000.0
                transferString = str(powerString2)
                my_label.updatePower(transferString)
        my_label.after(500, read_data, my_label)

    def main():
        window = Tk()
        my_label = MyWindow(window)
        window.title("Power Supply Controller")
        read_data(my_label)
        my_label.pack(side=TOP)
        window.mainloop()
    if __name__ == '__main__':
        main()
```

4) Microscope position control using stepper motors

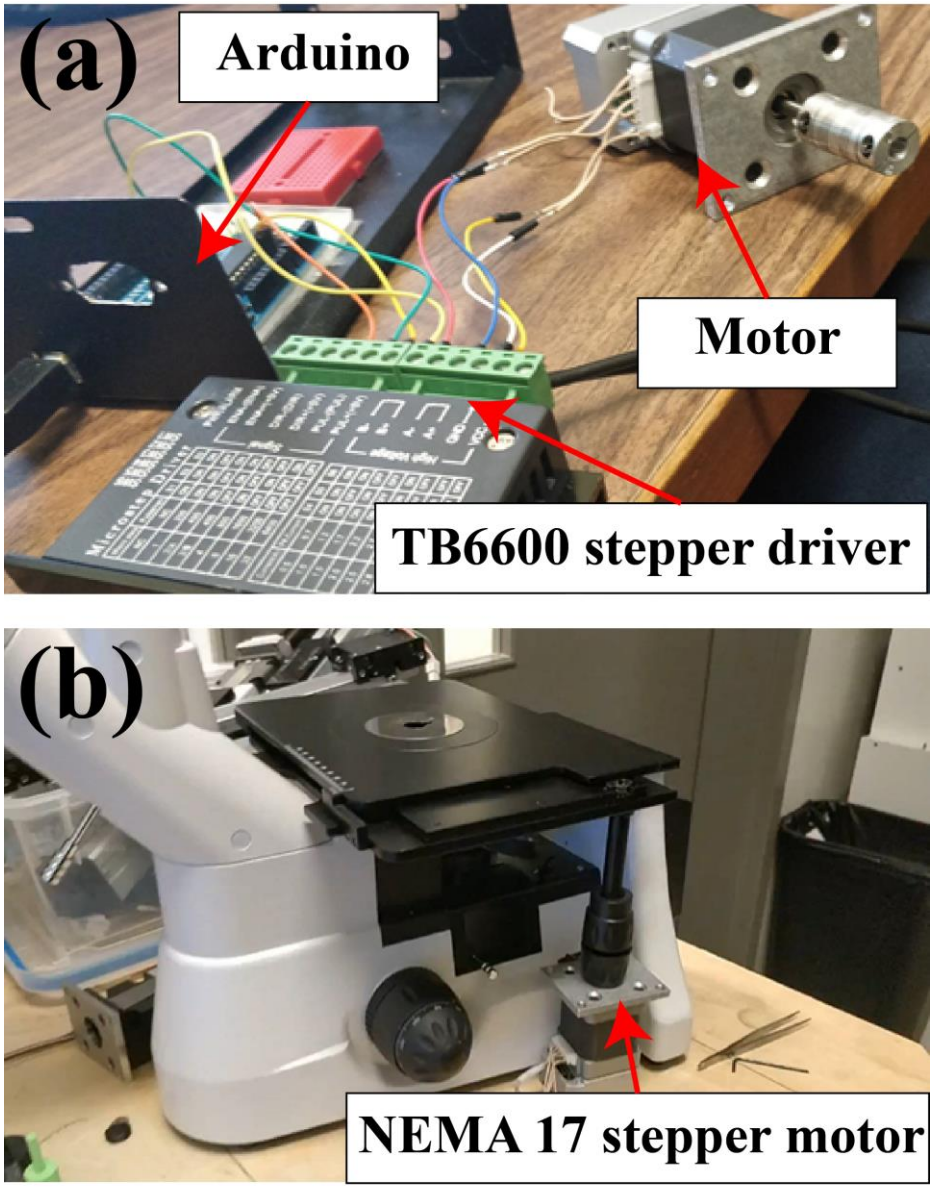

Figure C-1: Microscope automation, showing (a) components used to develop system including microcontroller (Arduino), motor and stepper driver (b) NEMA 17 stepper motor connected to microscope mechanical stage

Table C-1: Bill of materials for microscope position control system

Item	Cost (CAD)
Elegoo UNO R3 Board ATmega328P ATMEGA16U2 (Arduino)[6]	14.95
Usongshine 4 Lead Nema 17 Stepper Motor Nema 17 Motor (17HS4401S)[7]	15.49
TB6600 4A 9-42V Stepper Motor Driver[8]	19.99
Jumper wires[9]	10.99
Belker 12W Adjustable Voltage Universal AC/DC Adapter Power Supply[10]	18.9

Arduino software was used to control the system [11]:

```
#define dirPin 2
#define stepPin 3
void setup()
{
pinMode(stepPin, OUTPUT);
pinMode(dirPin, OUTPUT);
digitalWrite(dirPin, HIGH);}
void loop() {
digitalWrite(stepPin, HIGH);
delayMicroseconds(500);
digitalWrite(stepPin, LOW);
delayMicroseconds(500);
}
```

[6] https://www.amazon.ca/Elegoo-Board-ATmega328P-ATMEGA16U2-Arduino/dp/B01EWOE0UU/ref=sr_1_8?dchild=1&keywords=arduino+uno&qid=1616074780&sr=8-8

[7] https://www.amazon.ca/Nema17-Stepper-42BYGH-17HS4401S-Printer/dp/B0787BQ4WH/ref=sr_1_1?dchild=1&keywords=nema+17+stepper+motor&qid=1616075501&sr=8-1

[8] https://www.amazon.ca/TB6600-Stepper-Driver-Controller-tb6600/dp/B07B9ZQF5D/ref=sr_1_9?dchild=1&keywords=TB6600+stepper+driver&qid=1616075582&sr=8-9

[9] https://www.amazon.ca/120pcs-Multicolored-Breadboard-Arduino-raspberry/dp/B01LZF1ZSZ/ref=sr_1_8?dchild=1&keywords=jumper+wires&qid=1616075626&sr=8-8

[10] https://www.amazon.ca/Belker-Adjustable-Universal-Household-Electronics/dp/B07NKZCWT1/ref=sr_1_6?dchild=1&keywords=adapter&qid=1616075723&sr=8-6

[11] https://www.makerguides.com/tb6600-stepper-motor-driver-arduino-tutorial/

5) PID Temperature controller

```
"""
Created on Tue Jul 28 13:29:14 2020
@author: m8abdela
Temperature Controller using 34411A Multimeter (for temp. sensor), 2200-26-5
Keithley Power Supply for
Icstation 12V 12W Flexible Polyimide Heater Plate Adhesive PI Heating Film
10mmx93mm (Pack of 4)
Use "U3606 Multimeter DC Power Supply" manual from "Keysight Command Expert"
to control the power supply/obtain commands
"""
from IPython import get_ipython;
get_ipython().magic('reset -sf')

import visa
import time
import matplotlib.pyplot as plt
import scipy.io
from math import sqrt
from simple_pid import PID

#Convert Pt1000 Resistance value to a temperature reading
def roots(a,b,c):
    disc = b**2 - 4*a*c
    if disc >= 0:
        if ((-b + sqrt(disc))/(2*a))<300 and ((-b + sqrt(disc))/(2*a))>0:
            return (-b + sqrt(disc))/(2*a)
        elif ((-b - sqrt(disc))/(2*a))<300 and ((-b - sqrt(disc))/(2*a))>0:
            return (-b - sqrt(disc))/(2*a)
    else:
        return -10000000

plt.close('all')
sampleName = 'Temperature Controller';
failureflag = 0;
A = 3.9083e-3;
B = -5.775e-7;
RTD0 = 1000;

t = []
T1 = []
Tread1 = []
V1 = []

fname=time.strftime("%y%m%d%H%M%S",time.localtime()) + sampleName #filename
#GPIB INITIALIZATION WITH PYVISA
rm = visa.ResourceManager()
rm.list_resources()
multimeter = rm.open_resource('USB0::0x0957::0x0A07::MY48005925::0::INSTR')
DCsource = rm.open_resource('USB0::0x05E6::0x2200::9050135::0::INSTR')

tic = time.perf_counter()
DCsource.write('*RST')
DCsource.write('*CLS')
```

```
DCsource.write('OUTPUT ON')
DCsource.write('CURR 1')
DCsource.write('VOLT 1')
#DCsource.write('OUTPUT OFF')

class FilmHeater:
    def __init__(self):
        self.film_temp = 40
    def update(self, powersupply_voltage):
        voltage_reading = DCsource.query_ascii_values('MEASure:VOLTage:DC?')
        powersupply_voltage = voltage_reading
        if powersupply_voltage > 0:
            temp_values1 =
multimeter.query_ascii_values(':MEASure:SCALar:FRESistance?')
            opc1 = int(temp_values1[0])
            RR1 = roots(B*RTD0, A*RTD0, RTD0-float(opc1));
            Tread1.append(RR1)
            self.film_temp = RR1
            return self.film_temp

while failureflag == 0:
    vol = -10000;
    cur = -10000;
    while vol == -10000 or cur == -10000:
        toc=time.perf_counter()
        t.append(toc-tic)
        try:
            try:
                temp_values1 =
multimeter.query_ascii_values(':MEASure:SCALar:FRESistance?')
                opc1 = int(temp_values1[0])
                RR1 = roots(B*RTD0, A*RTD0, RTD0-float(opc1));
                Tread1.append(RR1)
                if (RR1) > 40: #50C=1194.00ohm, 60C=1232.40ohm,
70C=1270.80ohm
                    DCsource.write('VOLT 1.5')
                elif (RR1) < 40:
                    DCsource.write('VOLT 4')
#                    DCsource.write('VOLT %s' % (voltage))
                voltage_readings =
DCsource.query_ascii_values('MEASure:VOLTage:DC?')
                voltage_V = voltage_readings[0]

                boiler = FilmHeater()
                film_temp = boiler.film_temp
                pid = PID(100, 10, 5, setpoint=film_temp)
                pid.output_limits = (0, 100)
                power = pid(film_temp)
                film_temp = boiler.update(power)
                #The problem is that I want my setpoint to be 40C, not to
control the voltage, how do I make it clear that PID should act on voltage
based on temperature
#                v = FilmHeater.update(0)
#                while True:
#                    temp_values1 =
multimeter.query_ascii_values(':MEASure:SCALar:FRESistance?')
```

```
#                     opc1 = int(temp_values1[0])
#                     RR1 = roots(B*RTD0, A*RTD0, RTD0-float(opc1));
#                     Tread1.append(RR1)
#                     temperature = RR1
#                     # compute new ouput from the PID according to the
systems current value
#                     control = pid(temperature)
#                     # feed the PID output to the system and get its current
value
#                     v = FilmHeater.update(control)
##                      voltage_reading =
DCsource.write('MEASure:CURRent[:DC]?')
##                      voltage = voltage_reading
##                      # compute new ouput from the PID according to the
systems current value
##                      control = pid(voltage)
##                      # feed the PID output to the system and get its current
value
##                      v = FilmHeater.update(control)
            except:
                Tread = [];
                #print("error")
            T1.append(RR1)
            V1.append(voltage_V)
            data = {}
            data['t'] = t
            data['T1'] = T1
            data['power'] = power
            data['V1']= V1
            saved = 0

            while saved == 0:
                try:
                    scipy.io.savemat('%s.mat' % fname, data)
                    saved = 1
                except:
                    saved = 0
            time.sleep(5)
            maxlength2save = 10000
            if len(t) > maxlength2save:
                fname=time.strftime("%y%m%d%H%M%S",time.localtime()) +
sampleName #filename
                t = []
                T1 = []
                V1 = []
        except:
            vol = -10000;
            cur = -10000;
        plt.ion()
        gg = plt.figure(1)
        plt.cla()
        plt.plot(t[max(0, len(t)-300):],T1[max(0, len(t)-300):])
        plt.xlabel('Time [s]')
        plt.ylabel('Temperature [℃]')
        plt.show()
        gg.canvas.draw()
```

```
        gg.canvas.flush_events()

        plt.ion()
        gg = plt.figure(2)
        plt.cla()
        plt.plot(t[max(0, len(t)-300):],V1[max(0, len(t)-300):])
        plt.xlabel('Time [s]')
        plt.ylabel('Voltage [V]')
        plt.show()
        gg.canvas.draw()
        gg.canvas.flush_events()
multimeter.close()
DCsource.close()
rm.close()
```

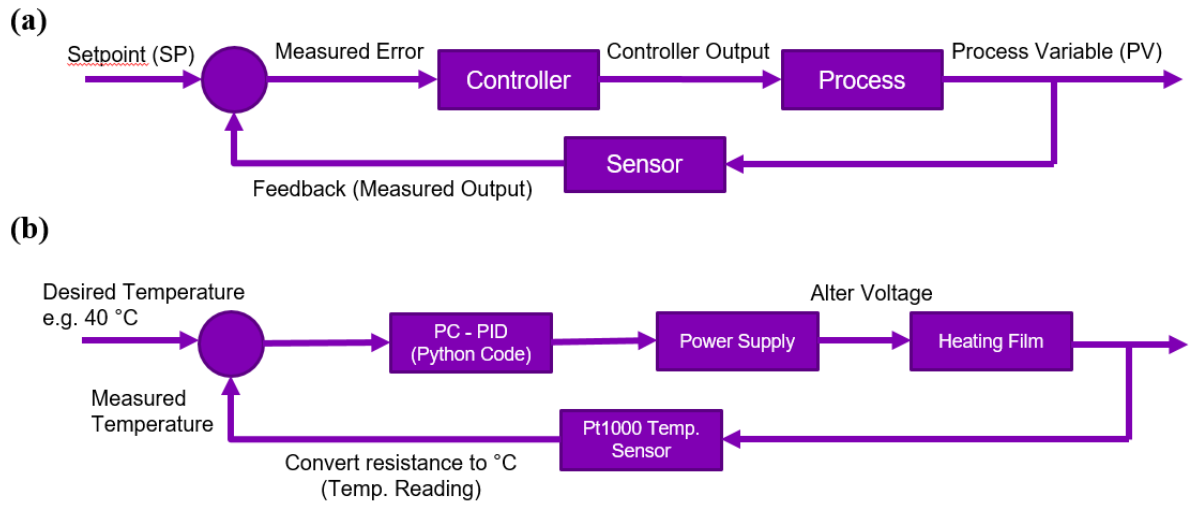

Figure C-2: PID temperature controller block diagram, showing (a) typical diagram (b) diagram for EM testing including all equipment used

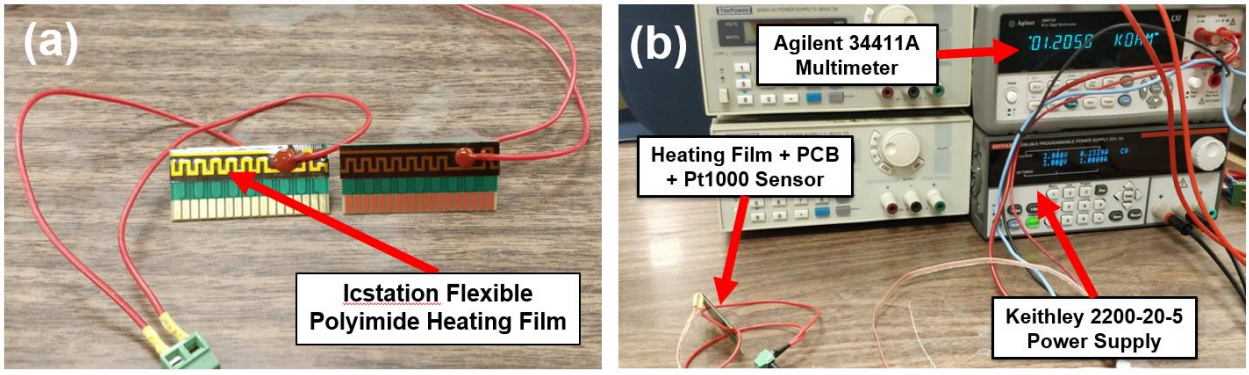

Figure C-3: (a) Heating film used for PID controller (b) Power supply, multimeter and temperature sensor connections to the heating film

Table C-2: PID temperature controller results, showing examples from four tests aimed at stabilizing chamber at 40 °C

Test #	Min Voltage (V)	Max Voltage (V)	Time to reach SP (s)	Temp. Range (°C)	Std Dev (°C)	Av. Temp. (°C)
1	0	7	-	38.6 – 49.8	3.64	44.01
2	1.5	4	31.4	38.6 – 43.3	1.0	40.35
3	2.5	4	47.1	39.7 – 42.2	0.73	40.84
4	2.5	3.5	62.6	39.7 – 41.5	0.46	40.45